Phase Change of Molten-Salt Flows in Energy Systems

Niccolò Le Brun

A dissertation submitted in partial fulfilment of the requirements for the degree of Doctor of Philosophy in Chemical Engineering of the University of London and the Diploma of Imperial College

University of London
Imperial College of Science, technology and Medicine
Department of Chemical Engineering
February 17, 2017

Statement of Originality

I hereby certify that, to my best knowledge, the content of this thesis is original and the results of my own work; all the assistance I received and the sources I used have been properly acknowledged.

Niccolò Le Brun
07 December 2016

Copyright Declaration

Journal Publications

1. N. Le Brun, C.N. Markides. *The Thermal Conductivity of Alkali Halides, including FLINAK: Re-evaluation of Previous Steady State Measurements.* Under preparation.

2. N. Le Brun, A. Charogiannis, L. Christopher, C.N. Markides. *Particle Image Velocimetry Measurements of Transient Water Solidification in a Channel Flow.* Under preparation.

3. N. Le Brun, G.F. Hewitt, C.N. Markides. *Transient Freezing in Direct Reactor Auxiliary Cooling System (DRACS).* Applied Energy, 2017, 186 (1): 56-67.

4. N. Le Brun, C.N. Markides. *A Galinstan-Filled Capillary Probe for Thermal Conductivity Measurements and its Application to Molten Eutectic KNO_3-$NaNO_3$-$NaNO_2$ (HTS) up to 700 K.* International Journal of Thermophysics, 2015, 36 (10-11): 3222-3238.

Conferences

1. ICONE 2017. N. Le Brun, A. Charogiannis, G.F. Hewitt, C.N. Markides. *Tackling Coolant Freezing in Generation-IV Molten Salt Reactors.* In: International Conference on Nuclear Engineering, May 2017, Shanghai, China.

2. UKES 2016. N. Le Brun, C.N. Markides. *Thermohydraulic Characterisation of Molten Salt as PCMs for Thermal Energy Storage.* In: U.K. Energy Storage Conference, December 2016, Birmingham, U.K.

3. ICACER 2016. N. Le Brun, C.N. Markides. *A Transient Model for Simulating the Freezing Process of Molten-salt Coolants.* In: International Conference in Advanced in Clean Energy, April 2016, Bangkok, Thailand.

4. UKHTC 2015. N. Le Brun, C.N. Markides. *Feasibility Analysis of Molten-Salt Direct Reactor Auxiliary Cooling System.* In: UK Heat Transfer Conference 2015, September 2015, Edinburgh, U.K.

Abstract

The possibility of molten salt freezing in pipe flow systems is a key concern for the solar-energy industry and a safety issue in the Generation-IV molten-salt reactors, worthy of careful consideration. The overriding aim of this thesis is to address this issue by providing an approach to quantify the solidification of molten salts in piping systems (in terms of mass build-up, effect on the flow and heat transfer, etc.). In light of this aim, several aspects needed to be investigated which affect how molten salt solidification can be predicted. Specifically, the work described in this thesis is hereby described: 1) An experimental method was developed to measure the thermal conductivity of molten salts, whose uncertainties significantly affect further modelling efforts. The method can be applied to measure the thermal conductivity of molten salts up to temperatures around 760 K, with an overall error better than 4%. 2) The thermal conductivities of $NaNO_3-NaNO_2-KNO_3$ eutectic (HTS) and $LiCl-KCl$ eutectic were measured up to temperatures of 700 K and 760 K respectively. In addition, data in the literature were re-evaluated by taking into account the thermal losses present in a particular experimental apparatus; the revised results were found to be in good agreement with other studies. These re-evaluated data and the measurements conducted in the present study were used to critically review and suggest the values of the thermal conductivities of common salts, including FLiNaK. 3) A 1-dimensional thermo-hydraulic model was developed under the steady state assumption and validated to predict transient freezing in internal pipe flows. The model can be incorporated in standard thermo-hydraulic codes and can be used to predict the solidification process in complex piping system where CFD is computationally expensive. 4) An experimental apparatus equipped with laser-based diagnostic measurement techniques was built to measure the growing thickness of an ice layer in contact with a cold surface and liquid water flow. The developed freezing model was validated against these experimental data and the discrepancies were considered. 5) The freezing model was then applied to study the behaviour of the Direct Reactor Auxiliary Cooling System (DRACS) under Loss of Forced Circulation (LOFC) with blackout. DRACS was found to be prone to failure due to freezing in the molten salt/air heat exchanger; its transient response was characterised and discussed.

iv

Acknowledgements

I would like to express my sincere gratitude to my supervisor Dr. Markides for the continuous support, patience, motivation, and inspiration; what he did in all these years means a lot to me. I would also like to acknowledge colleagues and academics for their insightful comments and encouragement, particularly Prof. Hewitt.

My deepest thanks also go to my friends with whom I shared everything throughout these four years. In particular, I wish to mention my "colleagues" Ajay, Aly, Arash, Cristoph, Emanuele G., Giuseppe, James, Ivan, Paul; and my old friends: Alessio, Anton, Emanuele N., Giulia, John, Ivano, Lorenzo F., Lorenzo L., Tommaso, Zanobi. Their friendship and support helped me overcome any difficulties and made my PhD experience always enjoyable. A special thank goes to my girlfriend Claudia whose presence made the time in London when this Thesis was written one of the happiest of my life.

Lastly I want to express my most sincere gratitude to my family and, in particular, to Giulietta Barbieri, Pio Sgarbi, Lucia Sona, Rodolfo Le Brun and Elena Barbieri, whose love and encouragement I always carry with me.

Above all, my parents Alessandra Sgarbi and Marco Le Brun deserve the deepest thanks; without their support this work would not have been possible. This thesis is dedicated to them.

'If we knew what we were doing, it would not be called research, would it?'

Albert Einstein

Contents

x

List of Tables

List of Figures

Chapter 1

Introduction

1.1 Background and Motivation

Energy systems make use of process fluids as heat and mass transfer vehicles. Since the beginning of the industrial revolution water has always been the most utilised process fluid due to its availability, low cost and ease of application. With the development of new technologies, other fluids, such as glycerine, ammonia, or toluene, have increasingly being considered as alternatives to water for their superior properties in their own specific application. Among these new categories of fluids, much interest have recently being given to molten salts, and ionic liquids in general [1]. Molten salts have indeed the potential to replace water in many applications, especially in the power industry. The main advantages of using molten salts over conventional fluids reside in their high boiling point (>1600 °C), good thermal and chemical stability, good solvent properties, ease of manufacturing and low cost (1$/kg) [2]. The solar energy industry was probably the pioneer in taking full advantage of the peculiar characteristics of molten salts. Molten eutectics of Nitrates and Chlorides salts have been indeed used for years in solar power plants as both heat transfer fluids and phase change materials (PCMs), for thermal energy storage [3].

1

There are however disadvantages associated with the use of molten salt technology which hamper its widespread implementation. One significant disadvantage is the relatively high melting point of the salts when compared to standard process fluids: the lowest melting point, exhibited by molten Nitrates, is around 150 °C, but the melting point can be as high as 1000 °C for molten Fluorides. The high melting point makes these salts impossible to be utilised without preheating, and thus significantly complicates the start-up phase of any process. Furthermore, all salts, except the ones used as PCMs, require to be maintained in the molten state during most of their operational life. The eventuality of a solidification of the salt in the piping system is a detrimental occurrence: the solidified mass of salt can clog the pipe or cause structural stresses in the pipe due to the change in volume during the melting/solidification process. To avoid this occurrence, in the solar industry auxiliary electric heaters have been installed which automatically switch on during a possible solidification of the liquid salt. These solutions are usually very expensive and represent an important entry in the overall cost balance [4, 5]. It could be argued that the problem of solidification also hampers the implementation of more efficient, high melting temperature melts, for which the cost related with freezing-prevention technologies would be excessive.

Solar energy is not the only sector interested in using molten salts as process fluids. In the last decade a renewed interest in safe nuclear energy promoted the need for Generation-IV nuclear power plants. Among the proposed designs of the reactor, molten salt reactors (MSRs), which utilise molten salts as coolant, have been indicated as a valuable choice from several countries, including USA and China [6]. China, in particular, is actively pursuing this technology by building a test reactor which should be completed in 2017 [7]. The idea to use molten salts as coolant for a nuclear reactor is however not new and it was first proposed during the 1960s with two projects: the Aircraft Reactor Experiment (ARE) and the Molten Salt Reactor Experiment (MSRE). Despite the promising results shown by these first prototypes, molten salt technology was progressively abandoned in

favour of Fast Neutron Reactors. Only recently, molten salts, and in particular Fluoride mixtures, have been re-evaluated as primary coolants [8]. The renewed interest in utilising molten salts as coolants is mainly due to their useful thermo-hydraulics and chemical properties [9]. A high boiling point allows the reactor to work efficiently at atmospheric pressure, reducing the risk of leakage and increasing the overall safety. The large difference between the melting and freezing point also allows for high energy output per thermodynamic cycle. A high heat capacity, on the other hand, increases the energy density and allows the piping volume to be reduced, decreasing the plant capital cost. Finally, the fuel can be directly dissolved in the salt which opens the possibility for safer reactor designs where the coolant itself is always in contact with the fuel, essentially eliminating Loss of Coolant Accidents (LOCAs) [10].

Despite the advantages, MSRs, similarly to solar power plants, are exposed to the problem of accidental coolant solidification. In MSRs, freezing of the coolant can take place in colder areas of the reactor distant from the core, such as inside secondary heat exchangers. Whereas in solar power plants molten salts accidental solidification represents an economical loss, in a nuclear power plant, where safety is paramount and the "trial and error" approach is not viable, it represents a much more serious scenario. In addition, the coolants envisaged for the Generation-IV MSRs have much higher melting points than the ones used in solar energy, and this further exacerbates the issue of accidental solidification. The overall picture is also complicated from the fact that solidification of molten salts in piping system is not well known and almost no studies can be found in the literature. The lack of knowledge in the field adds a further limitation because there are no methods available to predict if and how the solidification process will occur. The current approach followed to prevent freezing simply involves designing the system components so that the bulk temperature of the salt will remain above its melting temperature (see, for example, [11]). Such approach can be over-conservative in many cases, excluding designs or the use of melts which would otherwise be

beneficial; conversely, as it will be demonstrated in the last Chapter of this thesis, it can lead to consider designs, which are indeed unsafe, to be acceptable.

Given the problematic nature of solidification and the lack of appropriate predictive tools, the overriding aim of this thesis is to address the issue by providing an approach to quantify the molten salt solidification in piping systems (in terms of mass build-up, effect on the flow and heat transfer, etc.), to aid the development and implementation of molten salt systems in the nuclear sector and beyond.

1.2   Thesis Structure

More than one challenge has to be overcome to develop a reliable approach to simulate molten salt solidification in piping systems. Fig. 1.1 reports a diagram showing the various aspects (in green) involved in developing a predictive tool such as a code to simulate transient freezing in pipe flow. The main challenges which prevent the development of such predictive capability were found to be: 1) the very high uncertainties in the values of the thermal conductivity of molten salts; 2) the lack of a simplified model which could be incorporated in standard thermo-hydraulic codes; 3) the lack of experiments on transient freezing which could be used to validate the models. All these three difficulties have been tackled in the present thesis: Chapters 2 and 3 deal with 1), Chapter 4 with 2), and Chapter 5 with 3); Chapter 6 then concludes by describing a practical case of molten salt solidification in MSRs. Each of the contributions of the present work is represented by a red block in Fig. 1.1, which also indicates the relevant Chapter in which it is discussed. The detailed reasons for investigating all these topics are described in the following lines using Fig. 1.1 as a reference. The order in which the Chapters are introduced is logical (follows Fig. 1.1) and it is different from how the Chapters appear in the thesis.

Prior to the modelling of any process, its phenomenological characteristics need to
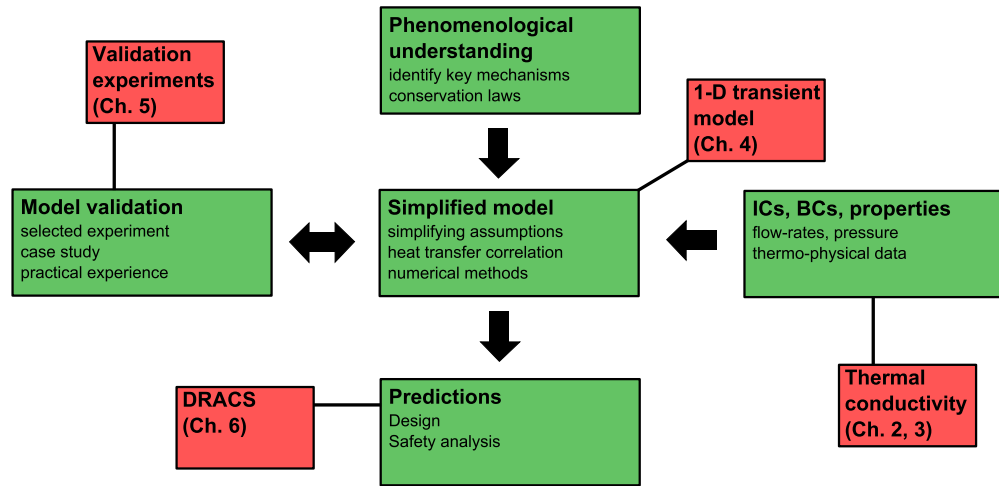
Figure 1.1: Diagram of the multiple aspects (green blocks) which need to be considered to develop a code to simulate transient freezing of molten salts in piping system. A layout of the research carried out in the present thesis is also shown by the red blocks.

be understood and qualitatively investigated (first green block at the top of Fig. 1.1). This fundamental research, which revolves around the phase change of molten salts, can be considered mature. Still some questions require a definite answer (for example regarding the fundamental structure of molten salts [12]), however the current level of knowledge is more than acceptable for any engineering application. The mathematical description of the freezing process is fully accepted: "Stefan-like", moving-interface problems that occur during solidification have been widely discussed [13, 14], while the theory behind mass and heat transfer in a Newtonian fluid is now in any thermo-hydraulic textbook.

The fundamental conservation laws describing the freezing process are usually too complex to be directly solved. Simplifying assumptions and suitable numerical methods are used to reduce the conservation laws to a simplified model (block at the centre of Fig. 1.1), which can be implemented in a numerical code to simulate complex transient problems in a reasonable time. Taking the nuclear industry as an example, most of the thermo-hydraulic behaviour of nuclear power plants is modelled under the 1-dimensional assumption, leaving the 3-dimensional, computational fluid dynamic (CFD) approach only to critical parts (e.g. the reactor core). With respect to transient freezing in internal flow, in the most

utilised commercial codes no simplified model exists which could be implemented to simulate with reasonable accuracy the transient behaviour of complex systems. For example, some of the most famous commercial thermo-hydraulic system codes TRACE, RELAP5, and GOTHIC do not have the capabilities to properly model transient freezing. GOTHIC, which is the most advanced model with respect to this aspect, treats the solidification process by stacking layers of solidified material (up to 3) one upon the other and by not considering any possible sub-cooling of the solidified layer [15]. This approach is computationally expensive and of dubious accuracy given the importance, in some systems, of the sensible heat in the solidified layer of fluid (see Chapter 5). TRACE and RELAP5, which have both been used to model MRSs, do not present an implementation for the solidification of molten salts and simply bound the temperature of the simulated fluid to its melting temperature [11, 16, 17]. This lack of predictive capability is not a surprise as solidification has rarely been an issue in the nuclear industry due to the low melting point of any liquid used (even molten metals). To properly simulate the freezing process, a simplified model was developed which could be also incorporated in standard thermo-hydraulic codes, such as the ones mentioned above. This model is explained in detail in Chapter 4.

Any model implemented to make predictions requires to be validated against experiments to check its accuracy and reliability, especially if the model is used for a safety analysis (left green block in Fig. 1.1). The model developed in Chapter 4 was therefore applied to simulate the results of previous experimental studies. The experimental conditions utilised in these studies, however, differ from the ones encountered in MSRs. Most of the previous experimental works consist of freezing a water flow in contact with a cold surface at temperatures which are 10-20 °C lower than the melting temperature of water. In a MSR the difference in temperature between the wall and the melting point of the fluid can be as high as 300 °C. Under such conditions, the thermal capacity of the wall and of the solidified layer close to the wall play a dominant role (as it will be shown in Chapter 5). In

order to better reproduce the conditions present in a MSR and further validate the model, we therefore designed and build an experimental apparatus. The details and the results of the experiments are explained in detail in Chapter 5.

To make reliable predictions any model needs to be provided with Boundary Conditions (BCs), Initial Conditions (ICs) and, most importantly, accurate values of the physical properties of the materials involved (right green block in Fig. 1.1). A critical problem with the development and use of these predictive codes which severely affects the results of the simulations concerns the lack of accurate data regarding the thermal conductivity of molten salts. Most of the current database about molten salts properties uses the results of dated works performed at Oak Ridge National Laboratories and, since then, has not been updated [18]. In particular, at present, the uncertainty regarding thermal conductivity data ranges between 20% and 60% for the most common types of salts [19]. The need for more accurate measurements has indeed been underlined by many authors (for example see references [20, 21]). The high degree of uncertainty on the thermal conductivity inevitably affects the validity of the basic thermo-hydraulics correlations and therefore affects the predictions of any thermo-hydraulic model. We therefore decided to review the thermal conductivity data found in the literature by conducting new measurements and re-evaluating previous data. This effort in retrieving reliable thermal conductivity values is described in Chapter 2 and 3 of this thesis. In particular, Chapter 2 explains the development of an experimental apparatus to measure the thermal conductivity of molten salts and Chapter 3 reviews their recommended values, based on the new values found in this work.

Finally, in Chapter 6, we apply the model developed to simulate the transient behaviour of the MSR during an accident scenario. In particular, we simulated the behaviour of the Direct Reactor Auxiliary Cooling System (DRACS), which is the passive safety system proposed for the new generation MSR. During accident, DRACS removes the decay heat from the reactor using a series of natural convection loops coupled with a molten salt/air heat exchanger. This heat exchanger is

one of the key part of DRACS which is especially sensitive to the freezing of the liquid salt. Solidification of the coolant can indeed clog the piping system compromising the heat removal capabilities. The results of the simulations on DRACS serve to show the possible solidification-related issues in MSRs and suggests how to avoid them. Chapter 7 closes this thesis by summarising the conclusions and recommending key aspects to be investigated in the future.

Chapter 2

Measurement of Thermal Conductivity: Experimental Method

In this Chapter the experimental method utilised to measure the thermal conductivity of molten salts is explained. Thermal conductivity is the capacity of a material to conduct heat via diffusion (as opposed to other forms of heat transfer such as advection and radiation). It is defined as the proportionality constant λ in the Fourier's equation:

$$q = \lambda \cdot \nabla T, \tag{2.1}$$

where q is the heat flux and T the temperature. Knowledge of thermal conductivity is often at the very basis of any energetic process characterisation. Indeed most energy technologies rely on working fluids, which along their cycle exchange heat through convection (diffusion and advection). For a thermal characterisation of the process, it is therefore of paramount importance the knowledge of how heat diffuses through the material: the thermal conductivity. It could be argued that the level of optimisation of an energetic process is closely related to the accuracy in the knowledge of its thermo-physical properties, with the thermal conductivity of water and steam now being known with less than 1% error [22].

Thermal conductivity data for high-temperature melts are often scarce or of poor quality, especially if related with the plethora of studies undertaken on low-boiling point liquids. The reason for this disproportion in the research interest can probably be ascribed to the fact that almost all the working fluids used in the past, for which accurate values of the transport properties are needed, were low-boiling point liquids; as such, the motivation to measure high temperature melts was low. New technologies, however, are increasingly moving towards the application of high temperature melts which still lack an accurate thermo-physical characterisation, especially with respect to thermal conductivity. The corresponding literature regarding the knowledge of the thermal conductivity of molten salts is even more limited. The reason for the lack of reliable data regarding molten salts is mainly the relative recent fortune of molten salt technology and, to a second extent, the many challenges encountered in the measurements themselves.

In the following Section we offer a review of the literature regarding thermal conductivity measurements with the overriding aim to demonstrate the need for accurate data and show the main challenges encountered by many authors in their experimental efforts. In Section 2.2 we summarised our failed experience in developing a method (pulsed-THWM) to measure the thermal conductivity. In Section 2.3 and2.4 the main method developed in this work is described in details.

2.1   Review of the Experimental Methods

The techniques utilised by the experimentalists to measure λ are several, each showing advantages and disadvantages. Going back to the mid 19th century, the first studies about the thermal conductivity measurement of molten salts used steady state methods, such as the Concentric Cylinder Method (CCM). A good review of these initial measurements can be found in [23].

Concentric Cylinder Method (CCM). The CCM, and its geometrical counterpart, the Parallel Plate Method (PPT), are based on the Fourier's equation (Eq. 2.1). In this technique, the material is placed between two concentric cylinders, which are externally surrounded by an insulating material. One cylinder is heated until the system reaches steady state and the power input is thereafter monitored. The thermal conductivity is found by measuring the temperature difference between the two cylinders via thermocouples and solving Eq. 2.1. The main advantage of this method lies in its simple structure, ease to build, and in the small number of parameters that need to be measured to work out the value of λ. However, according to the literature, there are two significant sources of error in using this apparatus that become large at high temperature. First, some of the power is inevitably dissipated through the insulation so the real heat flux is less than the one measured; second, the time required for reaching steady state is usually longer than the time required for natural convection to start, therefore a convective heat transfer process superimposes on the diffusive one. There are techniques which can be used to alleviate the magnitude of these two sources of error; power losses can be decreased by adding specially tailored guard heaters on the insulation to compensate for heat dissipation [24], while natural convection is diminished by making the gap between the two plates very small [25].

In these initial measurements conducted with steady-state methods, $NaNO_3$ and its mixtures were the most studied salts. In particular, several studies focused on $NaNO_3-NaNO_2-KNO_3$ because its low melting point (140 °C) facilitated sample handling and experimental safety measures. The preliminary data conducted by the first pioneers exhibited a significant scatter. It is here useful to briefly mention the experiment of White and Davis [26] who adopted the CCM with good repeatability and attributed the disagreement in the literature to the guard heaters used in CCM measurements by other authors. In their opinion, guard heaters are indeed difficult to calibrate, and a wrong calibration can lead to large error in the

measurements. They suggested to avoid guard heaters and, instead, to calculate the heat dissipated through the insulation. In Section 3.3 we will come back to the problem of thermal losses in the CCM, which, from the analysis conducted in the present work, appeared as the principal source of error in this steady-state method.

Later on, Turnbull significantly increased the repeatability of the measurements by implementing the Transient Hot Wire Method (THWM) on molten salts [27].

Transient Hot Wire Method (THWM). Among the non steady-state techniques, the most utilised one is by far the THWM. A historical review of this method can be found in [28]. As we chose to employ this technique in our own measurements, a more detailed explanation is required. This method consists of a thin metallic wire that acts both as a heater and as a thermometer. The wire is immersed in the liquid specimen and a direct current is used to heat the wire. The temperature of the wire, which is assumed uniform inside the wire, increases with time and its value is found by measuring the electrical resistance of the wire (that is a linear function of its temperature). The resistance of the wire is usually measured using a Wheatstone bridge. By knowing the rate at which the temperature increases it is possible to work out the thermal conductivity of the specimen; indeed liquids with a high thermal conductivity will remove more heat from the wire, on a time unit, than liquids with low thermal conductivity, and therefore the temperature increase will be slower.

The wire is modelled as an infinitesimal line heat source of zero heat capacity and infinite thermal conductivity. The corresponding equation describing the problem is:

$$\frac{1}{\alpha}\frac{\partial T}{\partial t} = \frac{1}{r}\frac{\partial}{\partial r}\left(r\frac{\partial T}{\partial r}\right);$$

(2.2)

here, α is the thermal diffusivity of the specimen, r the cylindrical coordinate

and t the time. This equation have to be solved with the boundary conditions:

$$r\left(\frac{\partial T}{\partial r}\right) = -\frac{\dot{q}}{2\pi\lambda} \qquad \text{for } t \geq 0 \text{ and } r \to 0 \qquad (2.3)$$

$$T(r,t) = T_0 \qquad \text{for } t = 0 \text{ and } \forall r \qquad (2.4)$$

where $\dot{q}$ is the heat generated by the wire per unit of time and per unit of length. The solution of Eq. 2.2 was derived by Carslaw and Jaegar [29] and applied by Healy et al. [30]:

$$T(r,t) - T_0 = \frac{\dot{q}}{4\pi\lambda}\left[\ln\left(\frac{4\alpha t}{r^2 e^\gamma}\right) + \left(\frac{r^2}{4\alpha t}\right) + ...\right], \qquad (2.5)$$

where γ is the Euler's constant of 0.5772. For a wire of radius a and for large values of $4\alpha t/r^2$, the temperature increase of the wire ΔT (assumed uniform) is:

$$\Delta T(t) = \frac{\dot{q}}{4\pi\lambda}\ln\left(\frac{4\alpha t}{a^2 e^\gamma}\right) + \mathcal{O}(a^2/\alpha t). \qquad (2.6)$$

Rearranging and taking the derivative with respect to $\ln(t)$ we find the approximate value of the thermal conductivity:

$$\lambda = \frac{\dot{q}}{(4\pi)}\frac{1}{\mathrm{d}(\Delta T)/\mathrm{d}(\ln(t))}. \qquad (2.7)$$

Eq. 2.7 is found to perform well during the experiments and to give accurate estimates of the thermal conductivity of liquids. The equation was however derived for an ideal wire and non-ideal effects add an error on the thermal conductivity estimations. These non ideal effects are related, for example, to the finite thermal capacity of the wire, the finite length of the wire, and the presence of an insulative coating. The errors caused by these non-ideal effects are usually less than 1% and they are taken into account by adding corrections

(δT_i) on the measured value of the temperature rise of the wire ΔT_{meas}:

$$\Delta T = \Delta T_{meas} + \delta T_1 + \delta T_2 + ... \qquad (2.8)$$

The expressions for the correction factors δT_i have been derived for many sources of error, see for example Ref. [30].

The biggest advantages of THWM are the simplicity and the accuracy of the apparatus. It suits particularly well to liquids because the experiments can be conducted in a very short time (from 0.1 to 6 s) preventing natural convection to start. This technique is, however, not directly transferable to molten salts in its standard implementation due to the finite electrical conductivity of the salt, which allows part of the current flowing through the wire to leak inside the liquid sample, thus distorting the signal and invalidating the standard analytical model. Specifically, the electrical power dissipated through the wire, and used as a direct indication of the heat transferred to the sample from the wire, becomes unknown.

In his work, Turnbull adopted a 50 μm platinum wire and each experiment lasted 1 min [27]. The author claimed that the current flowing in the electrically conducting liquid was minimal when compared with the one flowing in the wire; as such, he concluded that the experiment was not compromised by the high electrical conductivity of the salt. Other authors however experienced several problems when applying the THWM with electrically conductive fluids (see, for example, [31]). From our experience using bare wires we found that by-pass currents in the fluid compromise the experiments. In order to understand more in depth the consequences of a non-negligible electrical conductivity in the sample (indeed this is the very reason why THWM is so difficult to apply to molten salts), we ran a simulation using OpenFOAM, a computational fluid dynamics (CFD) package. Fig. 2.1 reports the simulated current densities (and patterns) in a 15 μm-TWHM wire immersed in an electrically conductive fluid such as a molten salts. Different
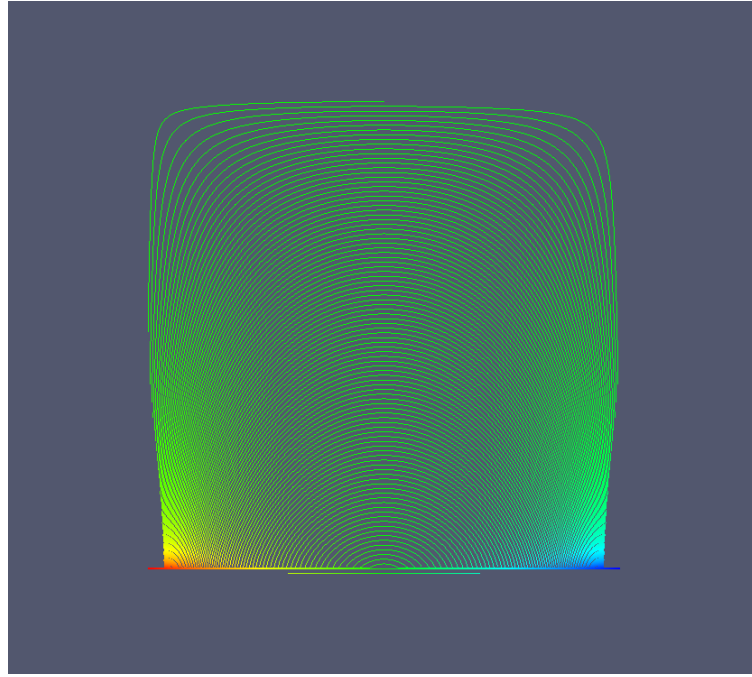
Figure 2.1: Current densities in a 15 μm wire surrounded by an electrically conductive fluid.

colours represent different current densities. From the simulations, the current flowing into the sample was approximately 35 % of the total current, therefore not negligible, in line with the opinion sustained by Nagasaka and Nagashima [32], in contrast with Turnbull [27].

In addition to the by-pass currents problem, the experiment of Turnbull was also probably affected by natural convection. Indeed, the experimental time of 1 minute, in our experience, seems too long to avoid natural convection. Even if Turnbull's results cannot be considered reliable for these reasons, his work is however a milestone towards the search for more appropriate methods and should be given his credit.

Successive studies showed that CCM was still the preferred technique among experimentalists in the area of molten salts. For high melting temperature salts, like Chlorides and Fluorides, most of the thermal conductivity measurements were conducted in Oak Ridge National Laboratories using steady-state methods as part of the Molten Salt Nuclear Reactor Project and these are well summarised in [33, 34].

Additional work was commenced 15-25 years later by Smirnov et al. [35] using the CCM and Cooke et al. using an updated version of the PPM [24]; their "variable gap method" is essentially a PPM in which the distance between the two plates is adjustable. By performing experiments with different distances it is possible to reduce the error due to natural convection. These successive studies which implemented PPM and CCM, however, did not improve the accuracy of the measurements which were still afflicted by a significant disagreement in the literature, as enlightened by [36]. Interesting is also the stepwise heating method developed by Kato et al. [37] which can be considered as a quasi steady-state method; the authors however did not pursue this method further.

Years later, a substantial improvement was achieved with the work of Nagasaka and Nagashima [32]. The authors implemented a modified version of THWM with the aim of solving the by-pass current problem by coating the wire with an electrically insulating coating. Their experimental prototype worked successfully at relatively low temperature. Unfortunately, the coated wire probes used in this approach had the disadvantage of being prone to cracks at high temperature due to the differential expansion between the (thin) ceramic insulating sheath and the internal heated wire, consequently losing their electrically insulating properties. As a result, the accuracy of the measurements at high temperature was compromised. Recent research have been conducted by Zhang and Fujii using a similar approach [38].

As an alternative to the ceramic-coated transient hot-wire probe, few years later, Hoshi et al. and Omotani et al. used a liquid-metal-filled capillary [39, 40]. The liquid metal can expand freely within the capillary, thus avoiding the aforementioned thermally-induced stresses. The authors measured successfully the thermal conductivity of some eutectic Nitrates up to 584 K. Subsequently, DiGuilio et al. [41] further explored the idea of Omotani and co-workers by using two Gallium-filled capillaries with a repeatability less than 1%. Nevertheless, the authors noticed that the technique stopped giving reliable results at around 600 K,

and ascribed this observation to the possible decrease in the electrically insulating properties of the quartz at high temperatures.

A completely different approach was investigate by Nagasaka et al. [42] using non-intrusive techniques (see also [43]). The aggressive nature of the salts and their high electrical conductivity challenged the application of standard methods. To avoid this problem Nagasaka et al. implemented a contact-less method which did not require the immersion of a probe in the salt: the Rayleigh Scattering Method (RSM).

Rayleigh Scattering Method (RSM). This method uses a laser to heat the molten salt at one point on its surface. This laser beam, of known frequency, is divided in two beams which cross the sample creating interference patterns and causing a sinusoidal temperature distribution in the sample. Another low-power probing laser is used to optically measure the phase grating of the temperature distribution. From the knowledge of how the phase of the temperature distribution changes with time it is possible to find the thermal conductivity of the material. The principal advantage of this method is that is contact-less, therefore it can be applied at very high temperature without the need to use suitable material to withstand the corrosive environment of the hot molten salts. However, the RSM is difficult to implement and the error related to the measurements is high. One of the main problem in utilising RSM with molten salts is that most of them are transparent or semi-transparent, therefore they require the addition of a dye to be able to absorb radiative energy efficiently. The use, however, of a dye changes the properties of the salt, decreasing the accuracy of the measurements [42]. Also, this method does not measure the thermal conductivity directly, but rather the thermal diffusivity. Calculating the thermal conductivity from the thermal diffusivity further increase the uncertainties in the measurements.

The experiment of Nagasaka et al. and by his collaborators provided invaluable data (most of the present database) and indeed a contact-less method seemed to

be able to overcome many of the drawbacks faced by previous methods. However, it seems difficult that they can achieve an accuracy better than 5% which is on the other hand typical for THWM.

Lastly, the experiments of Harada et al. [44] and Gustafsson [45] should be given credit, especially for the quality of experimental data. Harada et al., in particular, used the so-called Laser Flash Method (LFM) to successfully measure the thermal conductivity of some Alkali Halides. Similarly to the RSM this method appears more suitable than others for high temperature molten salts. It is however (again similarly to the RSM) of lower accuracy than the THWM.

> *Laser Flash Method(LFM)* In its standard form, LFM is based on placing the sample material within two metallic sheets and applying a laser pulse on one of them. The temperature on the other sheet is measured by means of an infrared camera and quickly decreases with time. From the knowledge of how the temperature of the plate drops it is possible to calculate the thermal diffusivity of the sample. The major problem with LFM resides in the low accuracy of the infrared camera which decreases the repeatability of the measurements.

For our choice of experimental system to measure the thermal conductivity we chose to start from the work of DiGuilio et al. Indeed, after several trials using a number of different techniques molten metal-filled capillaries seemed the most promising to achieve accurate measurements ($<3\%$). Specifically, the probe developed in this work and explained in the next Section, consisted of a flexible U-shaped quartz-capillary filled with the molten metal "Galinstan".

2.2 Pulsed-THWM: An Overview of the Challenges and Failures

Before introducing the measurement apparatus used in this study, we briefly comment, in this Section, on another solution which was tried at first, but found unsuitable. We believe that the underlying physical processes are interesting by themselves and are worth being exposed. However, the content of this Section is superfluous with respect to the overall discussion of this Chapter. This technique was developed to allow the THWM to be applied to electrically conducting fluids and it is based on polarising the wire with a current pulse; as such, we refer to it as the "pulsed-THWM". The rational behind this method is explained in the following text.

Current (charge) flow in molten salts is due to the movement of ions; their electrochemical behaviour resembles the behaviour of aqueous solutions. Therefore, in order to explain the concept of this method, we will refer to the behaviour of aqueous solution. When a significant difference of potential (voltage) is applied to two electrodes immersed in an electrolytic solution, charge is transferred across the electrolyte by the movement of ions. Charge is also transferred from the electrode to the solution because of the chemical reactions occurring on the surface of the electrode. If however, the voltage applied to the electrodes is less than the voltage required for chemical reactions to occur (we call this voltage the "decomposition voltage"), no transfer of charge between the electrode and the fluid is possible. Initially, upon the application of a voltage, current flows due to electrode polarisation, with cations concentrating close to the negative electrode and anions close to the positive one. After some time, however, a double layer is created at the electrodes that opposes the difference of potential externally imposed, zeroing the current. This was also the idea behind the apparatus developed by Perkins et al [46] which tried to polarize the THWM with respect to the cell. In other terms,
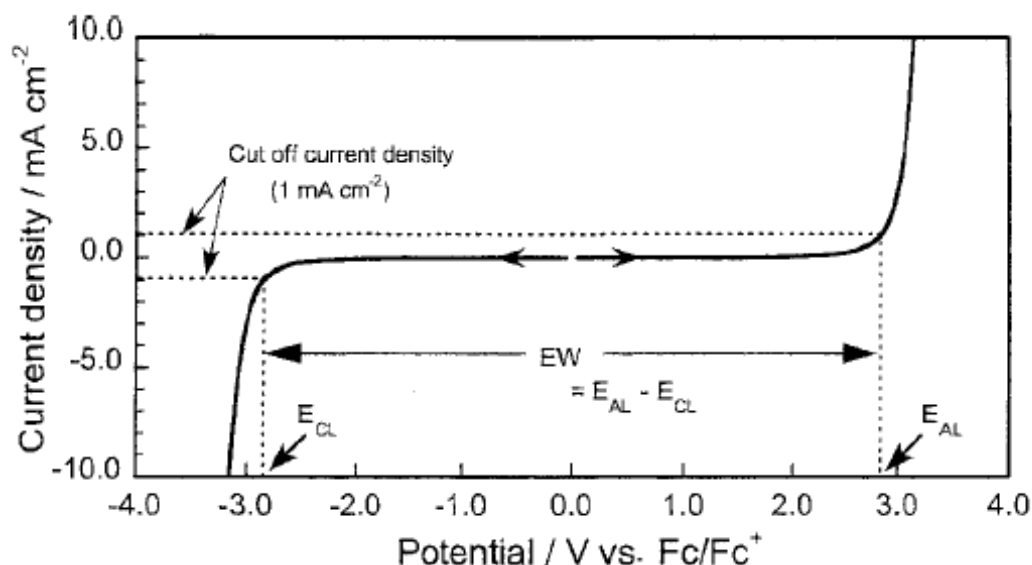
Figure 2.2: Linear sweep voltammogram of a ionic liquid. Image taken from Bard and Faulkner [47].

because the solution is conductive, the electrostatic (Gauss's law) impose that, if no charge is transferred at the interface between the electrodes and the solution the electric field inside the solution must be zero at the equilibrium. In Fig. 2.2 the linear sweep voltammogram of a molten ionic liquid is reported and this process of polarisation is clearly visible. As previously mentioned, if a difference of potential between E_{cl} and E_{al} is used, no current is flowing through the solution. In this case, the system can indeed be modelled as the circuit depicted in Fig. 2.3a. It is important to note that not all electrodes show this behaviour, but only those electrodes which are called "polarisable". Platinum electrodes in electrolytic solutions are usually highly polarisable.

Going back to the THWM, the case of a wire immersed in an electrolytic solution is not much different to two electrodes which are connected by a conductor. The electrical circuit of the cell system could indeed be modelled as shown in Fig. 2.3b. If we apply a voltage less than the decomposition voltage of our electrolytic solution, after some time the current should stop flowing inside the sample. The time taken time depends on the mobility of the ions in the sample. For water it has been measured to be in the order of seconds. In theory then, we could still
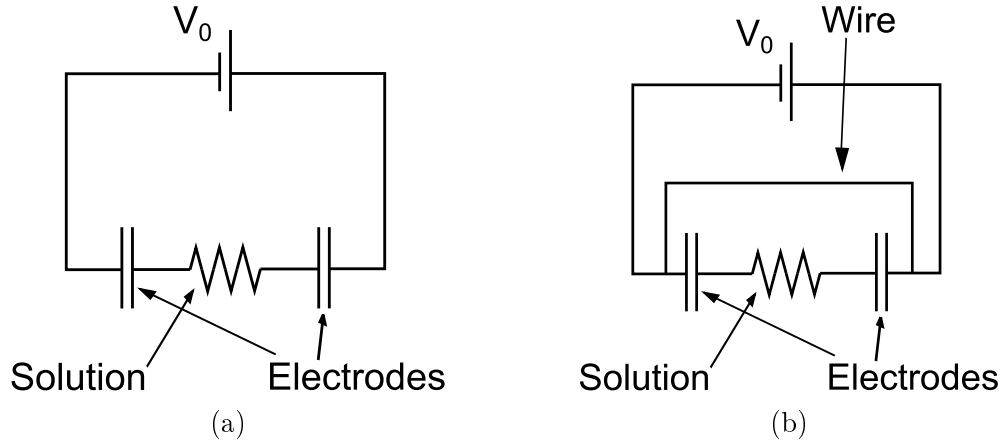
Figure 2.3: Electrical model of: a) two platinum electrodes in an electrolytic solution. b) a platinum wire in an electrolytic solution.

apply the THWM, only caring to discard the data measured before the platinum wire is fully polarised, when current is flowing in the sample. In literature we found that Baruel proposed a similar method to measure thermal conductivity of electrically conductive fluids [48]. The report of the author is however focused on the development of a theory for such method and unfortunately does not report practical considerations or results. One problem in this procedure is that the time needed for natural convection to start is as well of the order of seconds and, therefore, the time window needed to take accurate measurements (prior to the onset of natural convection) is too short. It was then decided to apply a very short pulse (of the order of few ms) to artificially polarize the wire and facilitate the process of creating a double layer. After the introduction of this pulse, the THWM is applicable in its standard design. We named this method the "pulsed-THWM".

A number of prototypes were built to test different solutions. The prototypes were produced in plastic (Fig. 2.4), as plastic can be immersed in low melting point, transparent fluids for optimal experiment diagnostic. The effect of an electrically conducting liquid on the measurement system was investigated by adding the salt NaCl ($\sim$3 M) to distilled water.

The results from the first runs of the pulsed-THWM, applied to measure the thermal conductivity of a solution of NaCl, conducted at temperatures up to 50 °C,
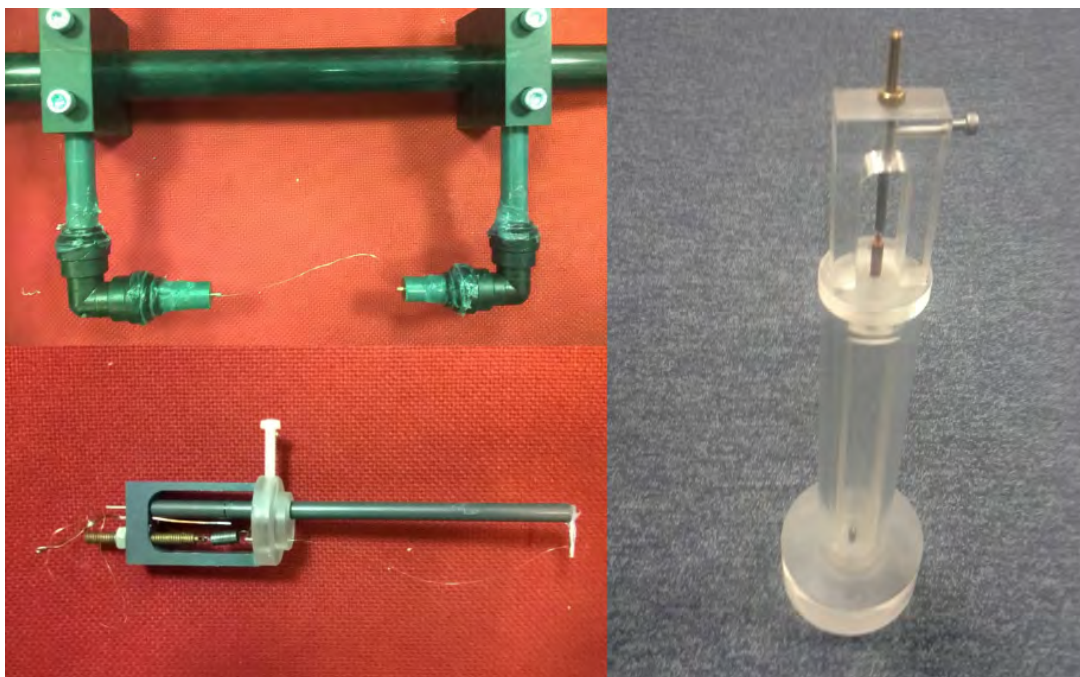
Figure 2.4: Probes for the pulsed-THWM

were very promising. If the standard THWM was applied, the signal was noisy (even if still easily detectable), but the linearity of the $\Delta T - \ln(t)$ plot was lost (see Section 2.1 for a description of the THWM), considerably decreasing the precision of the measurements. By using the pulsed-THWM instead, a smooth signal and a linear $\Delta T - \ln(t)$ profile were shown. The reduced data from the measurements were satisfactory and the probe measured effectively the thermal conductivity of both distilled and high-salinity water, according to the standard equations governing the THWM. After these first successes, different probes were built, and the error in the measurement decreased to less than 2% for temperatures below 50 °C, which is comparable with standard THWM. However, when testing the sensor at higher temperatures, such as 70 °C, the experimental error increased dramatically. At 80 °C, the signal coming from the probe was almost completely unusable. Successive experiments with pure platinum electrodes seemed to reveal that the main cause for this error were electrochemical reactions taking place on the wire due to the presence of small impurities either on the wire or in the salt. At high temperatures indeed, even small impurities can have a large contribution, due to the fast

kinetic of the electrochemical reaction, much lowering the decomposition voltage of the solution. Indeed bare platinum electrodes at high temperature ceased to behave as ideally polarisable, and current flow was detected upon the application of even small voltages ($<$1 V). Experiments were also conducted on molten Nitrates at 150 °C, but were found to be essentially impossible. Summarising the overall experience, the theoretical concept of this technique was validated and the main reason of its failure was found to be related to the challenges involved in keeping the materials composing the probe and the sample pure. Ideally, polarisable wire-probes made of high purity materials, would probably work on a sample of molten salt of high purity. After the initial trials, the method was not pursued further considering the large temperature gap which was needed to be overcome in order to measure the thermal conductivity of Chlorides melts which, in addition, are much more aggressive from an electrochemical point of view than water (smaller decomposition voltages, and thus more difficult measurements).

2.3   The U-Shaped Capillary Method

The experimental apparatus developed in the present work for the purpose of measuring the thermal conductivity of molten salts was based on the THWM and finds its predecessors in the work of Omotani et al. [40] and DiGuilio et al. [41]. The apparatus was designed to overcome the many challenges found in the literature and experienced during previous trials, primarily related to the current leakage (or by-pass currents) in the salt. The method is based on a metal-filled capillary, of the type described in Section 2.1 and consists of three main parts: (1) a furnace; (2) a measurement cell containing the material sample to be tested and the capillary probe; and (3) the electrical circuit with the furnace controls and the data acquisition unit (DAQ). In the following lines we explain in detail all the characteristics of the apparatus, underlying the reason behind the choice of specific components and methods, as well as the challenges which lead
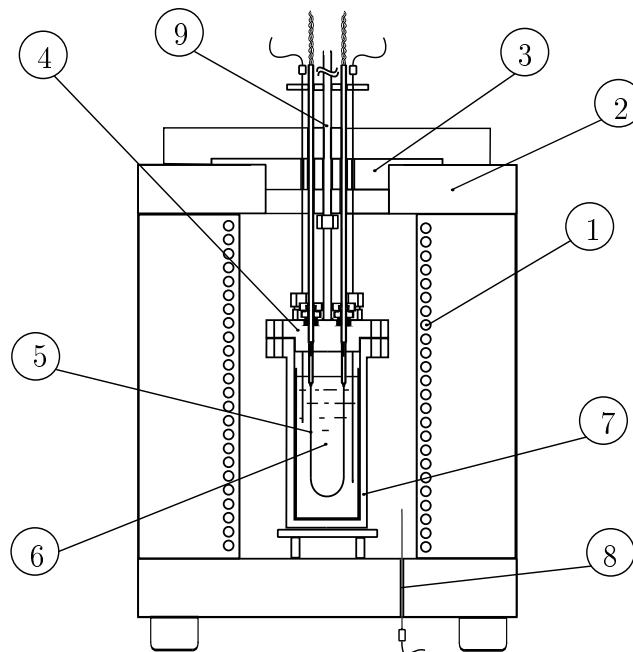
Figure 2.5: Furnace schematic, showing: (1) heating elements, (2) insulation, (3) tap, (4) probe support, (5) quartz capillary, (6) specimen (tested material sample), (7) sample container, (8) external thermocouple, and (9) lifting rod.

to the final design of the apparatus.

2.3.1   Experimental Apparatus

The furnace used is an in-house customisation of a Horbach furnace specifically modified to achieve a temperature distribution inside the sample which is as uniform as possible. A sketch of the furnace is provided in Fig. 2.5. It comprises of a heating cavity, with an internal diameter of approximately 100 mm, closed at the bottom, and a 70 mm aperture at the top. During the experiments the cell is inserted into the cavity and the aperture is closed in order to minimise heat losses. The cell is placed at a slight elevation above the bottom of the furnace to facilitate natural convection around the cell and assure a uniform heating of the cell's surfaces. The heating elements in the furnace are positioned on the side walls of the cavity and are protected by insulating material. A thermocouple is inserted at the bottom to monitor the temperature inside the cavity and for the purpose of avoiding overheating. The furnace is controlled from a computer using as feedback

input the temperature measurement inside the cell, measured by another K-type thermocouple.

A schematic of the measurement cell, employed in conjunction with the furnace described above, is depicted in Fig. 2.6. The cell is constructed using stainless steel and was designed to have enough thermal mass to smooth the thermal fluctuations inside the furnace. The cell consists of a sample container of internal diameter 41 mm and length 77 mm, and a lid. The volume of material sample needed to conduct a single experimental run is approximately $60 - 70$ ml depending on the thermal expansion coefficient of the material. The lid is constructed from a stainless steel flange and acts to provide both structural support for the sensing element and the possibility of hermetically sealing the sample container for the case of high-pressure measurements, if these are required; Fig. 2.7a shows the cell in this arrangement for high-pressure measurements. The lid can be raised and lowered by means of a supporting rod, and is equipped with four sealed pressure fittings for inserting temperature sensors and gas connections. In the standard arrangement, one RTD and two K-type thermocouples are used to measure the temperature and its temporal variation, respectively. Two quartz tubes are inserted into the lid and provide the connection to the Galinstan-filled capillary. Tungsten-rod electrodes are inserted at the end of the quartz tubes and serve as electrical contacts. Each Tungsten rod is laser-welded to two Constantan wires, and connected to the DAQ unit. The Constantan wires are inserted through two double-core alumina rods for electrical insulation. The alumina rods are connected to the lid using standard pressure fittings.

The sensing element consists of a U-shaped quartz-capillary filled with liquid Galinstan whose magnified picture is offered in Fig. 2.7b. The capillary has internal and external diameters of 0.05 mm and 0.08 mm, respectively. It is connected to two quartz tubes, one on each side, which have an internal diameter of 1 mm. The distance between the two quartz tubes in the arrangement shown in Fig. 2.6 is 25 mm, and the connections between each tube and the ends of the
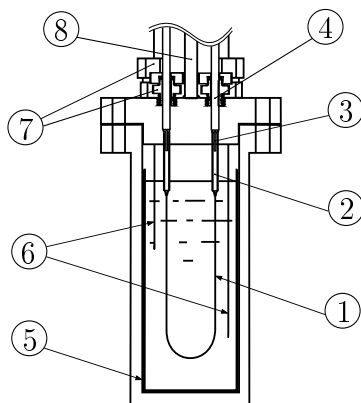
Figure 2.6: Cell schematic, showing: (1) quartz capillary, (2) quartz-tube end-connectors and supports, (3) tungsten rod, (4) alumina rod, (5) tested material sample container, (6) thermocouples, (7) pressure fittings, and (8) lifting rod.

(a)   (b)

Figure 2.7: Pictures of parts of the apparatus: a) measurement cell in the high-pressure- measurements arrangement b) Quartz capillary partially filled with molten Galinstan.

quartz capillary are made by using high-temperature glue. The choice of using a bent capillary instead of using a straight one was mostly made for practical reasons. A U-shaped capillary decreases the volume of the sample needed; this in turn allows us to minimise heat losses from the arrangement, which achieves a more uniform temperature distribution. In addition, the capillary is more easily replaceable compared to a straight arrangement.

The procedure of forming the capillary into the required form is as follows. Firstly, a quartz capillary (CM scientific) of total length 20 cm is allowed to dry in an oven at 300 °C for 2 h. This procedure is essential in eliminating the moisture present in the capillary; any residual moisture will evaporate at high temperature

forming vapour bubbles and interrupting the electrical contacts. Liquid Galinstan is then injected into the capillary through a fine syringe. Paraffin wax is used to seal the syringe needle onto the capillary. The capillary is then cut into a length of approximately $100 - 140$ mm and its length measured. The capillary is then bent in a U-shape and each of its two ends is inserted into a quartz tube, which have been pre-filled with liquid Galinstan. Surface tension assists in creating a good contact between the capillary and the tubes and in avoiding liquid metal spillage. The tubes and the capillary are subsequently sealed by using a combination of high temperature glues (Ceramabond 618-N, Silcoset 158). This operation is the most critical as an accurate and neat sealing has to be achieved in order to electrically insulate the liquid Galinstan without increasing the end effects of the probe. The glue is cured, first at 150 °C and then 300 °C. Later on Silcoset 158 had to be abandoned due to temperature restrictions. The quartz capillary is then tested at high temperature by briefly heating the capillary with a natural gas flame until the quartz glows; its resistance is monitored at the same time to check for abnormal behaviour. The capillary is then heated to the softening point of quartz to form the shape depicted in Fig. 2.6.

The most critical operation is the application of the high temperature glue. This operation is tedious and often causes the capillary to fail halfway through experiment. To avoid such a failure it was found, by trial and error, that it is absolutely crucial that no air bubbles are retrained within the sealing. These air bubbles interrupt the electrical contacts at the higher temperatures due to thermal expansion. The application of the glues once the liquid Galinstan is already inside the capillary minimises the formation of air bubbles and assures a more uniform spreading and sealing of the glue.

A schematic of the employed electrical circuit is depicted in Fig. 2.8. The data acquisition sequence starts when the temperature drift with time, as monitored through the thermocouple inside the cell, falls below 0.1 K/min. The DAQ modules NI-9213 and NI-9237 are then used to acquire continuously the signal from

the thermocouples and RTDs, respectively. A Wheatstone bridge is used to measure the varying resistance of the capillary during the measurements. The bridge comprises two highly precise resistors (R_2, R_3) and a potentiometer (R_1) to manually balance the bridge during an experiment. The nominal value of R_2 is 100 Ω $\pm$ 0.01%. R_3 is composed by multiple accurate 1 Ω resistors with very low resistivity temperature coefficients in an arrangement featuring series and parallel connections. This particular arrangement is adopted to minimise the error due to Joule heating in R_3, which was found to be as high as 3% if standard resistors of the same resistance were used. The bridge is powered by a Tektronix PWS 4205 DC power supply. A MOSFET transistor operated from the I/O port closes and opens the circuit. The switching time of the circuit has been measured and found to be less than 2 ms. The voltage across the Wheatstone bridge (V_{AC}) is measured by a NI-9237 DAQ module at a sampling rate of 2 kS/s. With certain adaptations the 50 Hz (background mains noise injected into the electronics) component was removed, and the noise reduced to approximately 4 μV. Voltages are measured at Points B, D and E using a dedicated NI-9239 DAQ module. Manual switches (not shown in Fig. 2.8) are used to swap between the present circuit and a secondary circuit that is connected to two Keithley 199 DMM digital multimeters. In this way it is possible to measure each resistance in the circuit with at least 1% accuracy during the experiments and minimise the effect of temperature variations.

2.3.2   Measurement Basis and Data Reduction

The thermal conductivity of the sample (liquid) material is found by modelling the electrically heated probe as a perfect line source (of infinite length and infinitesimal diameter), resting in a stagnant (i.e. stationary) liquid domain (of infinite extent). The working equation for this ideal case was derived by Carslaw and Jaegar [29]
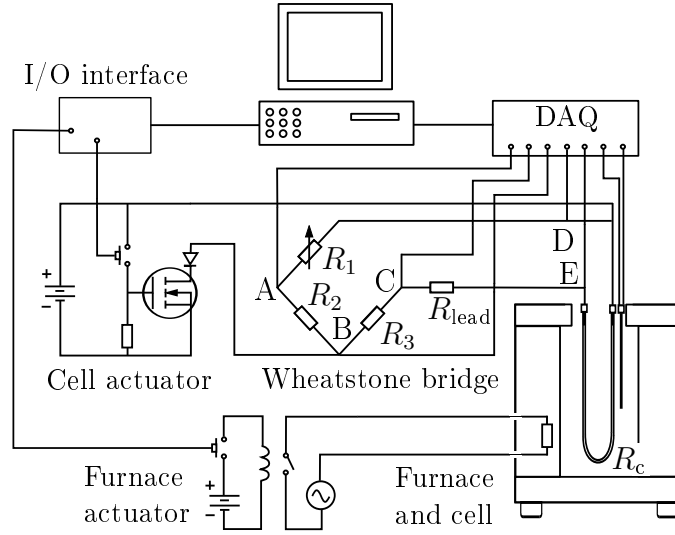
Figure 2.8: Schematic of the implemented electrical circuit. The data acquisition sequence and the furnace are both controlled from the I/O interface.

(see Section 2.1):

$$\lambda = \frac{\dot{q}}{(4\pi)} \frac{1}{\mathrm{d}(\Delta T)/\mathrm{d}(\ln(t))} \, . \tag{2.9}$$

When applied to the quartz-capillary arrangement used in this work, Eq. 2.9 relates the thermal conductivity of the liquid sample to the rise in the temperature of the capillary caused by a thermal input originated by imposing a known electrical power to the capillary probe. The temperature rise of the capillary during an experiment is calculated as:

$$\Delta T = \frac{\Delta R_{\mathrm{c}}}{\mathrm{d}R_{\mathrm{c}}/\mathrm{d}T} \, , \tag{2.10}$$

where R_{c} is the resistance of the capillary as measured by the Wheatstone bridge and $\mathrm{d}R_{\mathrm{c}}/\mathrm{d}T$ is its dependence on the temperature. The measured temperature rise of the capillary during the experiments was between 3 and 7 K, depending on the applied power.

The resistance of the capillary R_{c} is calculated from the voltage measured across the Wheatstone bridge, V_{AE}:
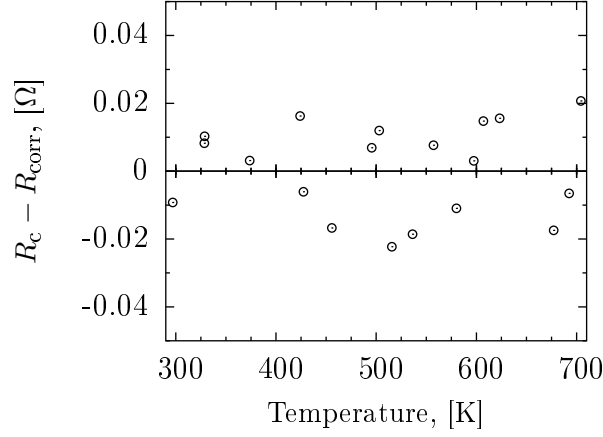
Figure 2.9: Residuals of a linear fit to the capillary resistance versus temperature data. The uniform distribution of the residuals indicates a constant value of dR_c/dT. The resistance of the capillary was around 15 Ω, varying between different probes.

$$R_c = \frac{(R_3 + R_{\text{lead}})\left[R_1 + (R_1 + R_2)\frac{V_{\text{AE}}}{V_{\text{BD}}}\right]}{R_2 - (R_1 + R_2)\frac{V_{\text{AE}}}{V_{\text{BD}}}} \; ; \tag{2.11}$$

where the constants R_1, R_2, R_3 and R_{lead} are the resistances described in Fig. 2.8 and are approximately constant during one measurement while V_{BD} is the voltage applied to the bridge.

Based on the knowledge of the capillary resistance R_c, the value of the derivative term dR_c/dT can be found by plotting the probe resistance R_c as a function of temperature and fitting a linear relationship to the data. A typical plot of the residuals from such a linear fitting is shown in Fig. 2.9 for a probe with a resistance of approximately 15 Ω (and a dR_c/dT value of 0.0122 Ω/K). As indicated by the figure the residuals are uniformly scattered over the temperature range, suggesting that a linear relationship is a reasonable fit to the data, and by extension, that the extracted (constant) value of the derivative dR_c/dT is an accurate measurement of this term.

Furthermore, the total power Q dissipated in the capillary is found by measuring the current I passing through the capillary:

$$Q = R_{\mathrm{c}} I^2 \,. \tag{2.12}$$

The current is calculated from the voltage drop V_{BC} across resistance R_3. The thermal power Q was confirmed as varying only slightly during each measurement run; its average value during each run is used. The power input per unit length $\dot{q}$ is then calculated by dividing Q by the length of the capillary. At this point all terms needed to evaluate the thermal conductivity of the liquid sample λ from Eq. 2.9 are, in principle, known.

Nevertheless, because of inevitable imperfections and end-effects in the connections between the capillary and the supporting quartz tubes, it is impossible to establish exactly the effective length of the capillary exposed to the fluid. In a series of tests, the actual length of the capillary was used to calculate λ for known liquids, and it was found that all measurements suffered from a systematic error of $6 - 10\%$ depending on the probe. It was therefore decided to adopt the same procedure described by Hoshi et al. [39], and to use an effective length l_{e} for calculating $\dot{q}$:

$$\dot{q} = \frac{Q}{l_{\mathrm{e}}} \,. \tag{2.13}$$

The effective length was estimated via an additional set of calibration runs with known (standard) fluids (Section 2.4).

2.3.3   Procedure

Once the data acquisition sequence is initiated, the NI 9237 module commences data logging from the Wheatstone bridge and, subsequently, the I/O interface closes the bridge circuit described in Fig. 2.8. The voltage across the bridge is measured at a typical sampling rate of 2 kS/s and converted to a temperature
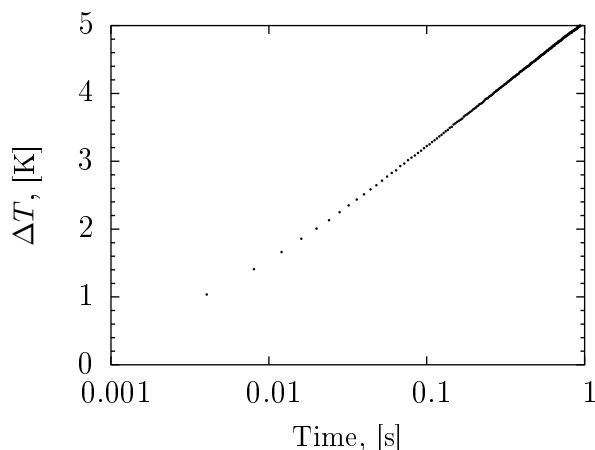
Figure 2.10: Temperature rise of the capillary as a function of time. The mathematical model for transient hot wire method applied to the U-shaped capillary.

rise according to the aforementioned expression; a typical plot of the temperature rise is depicted in Fig. 2.10. The value of $\mathrm{d}(\Delta T)/\mathrm{d}(\ln(t))$ is calculated from linear fitting to the temperature rise versus (logarithmic) time curve. Fig. 2.11 shows the relative residuals of such fitting. The temperature was found to increase linearly with $\ln(t)$ at least between 0.15 and 0.6 s. Before 0.15 s the theoretical model was not applicable due to second order unsteady effects caused by the finite dimensions of the capillary [49]. After 0.6 s, depending on the properties of the sample and the temperature distribution in the cell, natural convection occurred and the rate of rise in the temperature of the capillary diminished. The start of natural convection could be easily detected because the residuals of linear fittings increased drastically. In some cases, convection was found to occur as late as 1.6 s from the start of the measurement.

2.4   Testing and Calibration

A calibration needs to be performed to calculate the effective length l_{e} described in the previous section. The value of l_{e} was calculated by matching the measured thermal conductivity of distilled (DI) water at ambient temperature with its reference value. DI water was chosen as the calibration fluid because its thermal
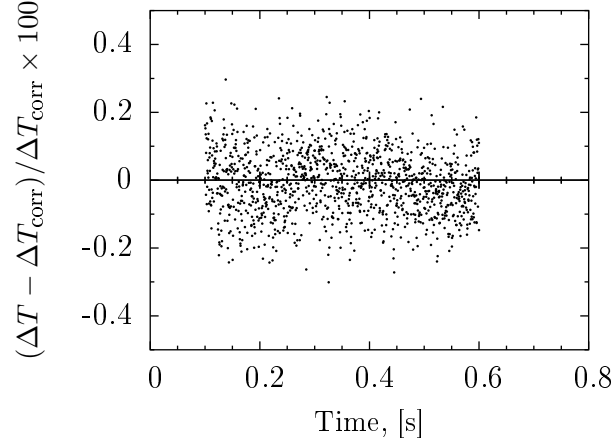
Figure 2.11: Relative residuals of the linear fitting of the temperature rise versus $\ln(t)$. The uniform distribution of the residuals indicates a linear increase of $\ln(t)$ with time.

Table 2.1: Test measurements of the current probe against reference data for DI water, Toluene and Glycerol. The accuracy of the probe, based on these data, was better than 2% up to 430 K.

Liquid	Temp. [K]	λ (meas.) [W/m K]	λ (ref.) [W/m K]	Error [%]
DI Water	305.5	0.6184	0.6184	0.0
	331.1	0.6495	0.6509	-0.2
Toluene	276.2	0.1367	0.1376	-0.7
Glycerol	301.7	0.2903	0.2855	1.7
	326.9	0.2923	0.2886	1.3
	374.6	0.2974	0.2948	0.9
	431.2	0.3028	0.3022	0.2

conductivity is similar to that of molten salts. A water bath was used to ensure a uniform temperature distribution during the calibration measurements. The calibrated probe, along with the established effective length l_e from the DI water runs was then further tested against Toluene and Glycerol at elevated temperatures up to 430 K. The effective length l_e was found to be within 15% of the initial length of the capillary. All the calibrated probes measured the thermal conductivity of Toluene and Glycerol with an error better than 2%. Typical results from the calibration tests are shown in Table 2.1. The reference data for the thermal conductivities of DI water, Toluene and Glycerol were taken from Ramires et al. [22], Ramires et al. [50] and CINDAS [51], respectively.

An analysis of the instrument accuracy on known standards was conducted in accordance with ISO 5725-2:1994 [52]. A complete analysis of the performance of the present method is possible up to 430 K by comparing the measurement results of standard fluids with their relatively accurate literature data. In this range, the precision of the method was quantified by the expanded deviation of repeated measurements, given a 95% confidence interval. The expanded deviation was found to increase slightly with temperature and to reach a value of 0.8% at 430 K. The dominant effect acting to limit precision is attributed to the presence of non-negligible natural convection in the fluid volume inside the cell. It was indeed noticed that when the temperature gradient in the cell was higher, the repeatability decreased. The trueness of the method, as calculated by the maximum difference between the mean of repeated measurements of standard fluids and their reference data, was less than 2%. Considering that the thermal conductivity of the liquids used as a reference is also known within an error, a 2% trueness is considered adequate for measurements up to 430 K. Major sources of bias can reside in the non-negligible natural convection in the fluid, in the end effects, and in the non-straight arrangement of the capillary. Above 430 K a complete analysis of the instrument performance cannot be done due to the absence of thermal conductivity standards.

It is important to discuss briefly the role of the not-straight arrangement of the capillary. This particular arrangement could affect the accuracy of the measurements in three ways: (1) the working equations for the transient hot-wire method do not rigorously apply; (2) the non-vertical alignment decreases the time for the onset of natural convection; and (3) the non-vertical alignment magnifies the error due to natural convection already present is the cell.

With respect to the first issue, we found that Eq. 2.9 could predict satisfactory the behaviour of fluids of known thermal conductivity, and the linearity of $d\Delta T / d(\ln(t))$ was conserved. This is not unexpected if we consider that the diffusive heat transfer length scale λ_d is approximately defined as:

$$\lambda_{\mathrm{d}} = \sqrt{\alpha\tau}\,, \qquad\qquad\qquad (2.14)$$

where α is the thermal diffusivity of the liquid and τ the timescale of the measurement. If we take 5×10^{-7} m^2/s and 1 s as conservative values for respectively α and τ, λ_{d} is approximately 0.7 mm, much less than the overall length of the capillary (about 100 mm).

With respect to the onset of natural convection, we found that this occurs between 0.6 and 1.6 s, that is indeed less than what is usually encountered by using a straight capillary. However the time window is always wide enough to assure an accurate calculation of $\mathrm{d}\Delta T/\mathrm{d}(\ln(t))$ and the aforementioned effect does not undermine the measurement.

Finally, the non-vertical alignment of the capillary would likely cause the diffusion of heat to be parallel to the flow direction and consequently modify the ideal temperature field. To avoid this effect the temperature distribution inside the container is kept as homogeneous as possible and the temperature gradient during a measurement is always less than the differential error between the thermocouples (<0.3 K). Even with this precaution, natural convection could occur with a temperature difference less than 0.3 K and indeed part of the current error could be ascribed to the non-vertical alignment of the capillary.

Another source of error could arises from the quartz capillary which can be regarded as a (relatively) thick insulative layer. An estimation of the correction δT_i, as given in Ref. [30] (see Eq. 2.8) for the presence of an insulative layer, revealed that the change in the evaluation of $\mathrm{d}\Delta T/\mathrm{d}(\ln(t))$ is large (approximately 3-5%). However this correction is indirectly taken into account by calibrating the effective length l_e. As such the error related to the quartz layer is lumped into the overall error in the estimation of the effective length l_e and it does affect much the accuracy of the apparatus, as also reported by Hoshi et al. [39].

The capillary method, as explained in the previous sections was applied to molten salts. Based on the experimental results, which are given in Chapter 3, the overall performance of the present instrument and technique seem satisfactory, achieving a measurements uncertainty of 3.1% for molten Nitrates up to 700 K. The uncertainty regarding the measurements of molten Chlorides (again given in Chapter 3) are much worse but this was found due to problems in the sample preparations. It is rather interesting that the U-shaped capillary is able to give very reasonable results and perform with similar levels of accuracy as those in other studies done with a straight capillary [40], which is more representative of the theoretical model based on which the relationships that are used to estimate the thermal conductivity from the raw measurements (see Section 2.1). This is a welcome result, and can also help towards a better understanding the effect of natural convection on the transient hot-wire method. Specifically, it endorses the claim that the effect of natural convection is negligible, as long as the time window over which the measurements are acquired is short enough not to allow the generation of fluid circulation currents in the tested fluid-material. Of course, such short time-windows over which to make these measurements require sensible electronics and low-noise signals, but this is a condition that today is much easier to achieve than in the past. The U-shaped arrangement will probably not be able to achieve the accuracy of the straight transient hot-wire, which has proven to be capable of going below 1% [41]. However, for its applications in particular systems, such as molten salts, an overall error of less than 4% (taken from a calculated uncertainty of 3.1%) is more than satisfactory and the present method has some practical advantages, such as requiring a smaller sample volume for the measurement.

The capillary probe has proven capable of conducting molten-salt thermal-conductivity measurements with reasonable results up to 760 K. We also conducted some destructive measurements beyond 760 K. The maximum temperature at which we could obtain reliable data was 780 K. After about 760 K, some measurements were found to be erroneous. Unfortunately, therefore the method developed could not

reach the 1000 K temperature threshold which we set as a goal during the design phase. It was identified that the problem resided in the capillary connections to the supporting quartz-tubes, which failed at higher temperature. The connections were found to fail between 760 and 780 K exposing the liquid Galistan to the molten salt or causing the capillary to detach from the support. We tried to solve this problem by using different materials to seal the connection and we partially succeeded by extending the temperature range of the instrument by 80 K (initial connection were found to fail at 700 K). However it seems that this method requires an innovative step in its design rather than a rightful choice of material to extend its temperature range. As for now, the connection between the capillary and the tubes are just too fragile. Alternatively, a single capillary could be produced from stretching a quartz-tube without the need of any connection. In our efforts such method was however very difficult to adopt requiring precision, suitable materials and dedication.

Finally, it is useful to discuss briefly the potential problem of current leakage in the present instrument, as identified in the work by DiGiulio et al. [41]. The authors stated that the quartz lost its electrical insulating properties in their experiments at temperatures higher than 590 K. In our case, we did not encounter any sign of current leakage, at least up to 700 K. If current leakage was present in our system the quality of the measurement would decrease substantially due to preferential current path caused by the U-shape configuration, leading to errors similar to those mentioned above when using temperatures higher than 700 K, essentially because whenever the liquid Galinstan was exposed to the salt this could be very clearly detected in our present arrangement. Indeed the sample container was polarised compared to the Wheatstone bridge so that a minimal short circuit between the two would be easily sensed. DiGiulio et al. [41], however, offered convincing arguments that current was leaking through the quartz. As a possible explanation, we may suggest that the different behaviours between the studies could be ascribed to either the quality of the quartz or the higher reactivity of

liquid Gallium compared to liquid Galinstan.

2.5   Conclusions Chapter 2

This Chapter reported on a successful implementation and validation of an instrument and a related technique based on a Galinstan-filled, U-shaped capillary to measure the thermal conductivity of molten salts. It was demonstrated that:

- The U-shape capillary can satisfactorily behave as the conventional transient hot-wire method based on an infinite line-source, and, in addition, benefits from some practical advantages.

- Contrary to DiGiulio et al. [41], it was noted that the quartz capillary retains its electrically insulating properties, at least up to 760 K.

- The present method appears suitable for measuring accurately the thermal conductivity of high temperature fluids, including that of electrically conducting fluids such as molten salts, up to temperature of 760 K, with an overall error better than 4%.

- The capillary method was found to be significantly hampered by the difficulty in sealing the connection between the capillary and the tubes at high temperature ($>$ 780 K). An innovative step in the design of the method seems to be required to significantly overcome this difficulty; otherwise the capillary method cannot reasonably be expected to reach the 1000 K threshold.

The main difficulties in a previous unsuccessful work (pulsed-THWM) were also reported to offer a better understanding of the challenges involved in these measurements.

Chapter 3

Measurements of Thermal Conductivity: Experimental Data

In this Chapter we report the values of the thermal conductivity of some molten salts. The uncertainty in the literature regarding the thermal conductivity of molten salts is high (20%-60%) and it affects the reliability of numerical codes and models which simulate the thermo-hydraulic behaviour of molten salts processes. Section 3.3 reports the recommended values obtained in this work, which are considered more reliable (average uncertainty of approximately 15%). These values were the results of: 1) our own measurements (conducted with the apparatus described in Chapter 2) which are reported in Section 3.1 and 3.2; 2) a re-evaluation of some data found in the literature and previously considered unreliable. Such analysis of the previous literature is reported in Section 3.3 and contributed most to the tabulated data. Finally in Section 3.4 we discuss the applicability of standard heat transfer correlations to molten salts in light of the new values of the thermal conductivity obtained.

3.1   Experiments: Materials and Methods

The apparatus described in Chapter 2 was applied to measure the thermal conductivity of: 1) molten KNO_3-$NaNO_3$-$NaNO_2$ eutectic, also known as Heat Transfer Salt (HTS); 2) molten LiCl–KCl eutectic. HTS has been selected because its melting point is within the range of temperatures for which the thermal conductivity of standard fluids such as Glycerol is known (see Section 2.4). In this way, the performance of the capillary probe can be further ascertained by allowing a smooth transition between the experimental conditions used for conducting the measurements of standard fluids and the ones used for HTS. Also, more data are available for HTS and, even if an agreement is still lacking, using HTS allows for a more accurate comparison with pre-existing studies. In addition, reliable values (<1 %) of HTS could make this material a high-temperature standard for calibrating thermal conductivity instruments. Molten LiCl–KCl eutectic was chosen for its importance in MSR and its use in nuclear reprocessing. The lack of data related to its thermal conductivity makes his measurement much needed.

HTS was obtained by mixing KNO_3, $NaNO_3$ and $NaNO_2$ in a respective molar-ratio of 0.44:0.07:0.49; all salts were in powder form (>99% purity). The quantity of each salt was weighed using a laboratory scale with an accuracy of ± 0.01 g. The salts were firstly thoroughly mixed, and then melted in the sample container. The high porosity of the powder caused the volume of the salt to decreases as the melting process took place, so that it was necessary to add additional quantities of salt to the container in order to reach the level of liquid required for the measurements. Once the sample container was filled with liquid salt up to the desired level, the probe was lowered and immersed into the liquid. The furnace was closed and insulated, and the temperature was left to stabilise based on a specified set-point until the temperature variations, measured with a 1 mm-thick reference thermocouple, dropped below 0.1 K/min. The steady-state took approximately one hour to be reached. The bridge was then balanced using a current pulse and the data

acquisition sequence started. The measurements were repeated with at least two different power inputs, with at least two repetitions per test. Having completed the measurements at one temperature, the temperature was then changed and the procedure repeated. During the measurements, the temperature range was swept back and forth in order to avoid any change in the capillary behaviour due to thermal ageing, and in order to quantify the possible presence of an hysteresis in the results. Three different probes were used to measure the thermal conductivity of HTS.

LiCl–KCl was obtained by mixing LiCl and KCl at their respective eutectic ratio of 0.557:0.443. The salt was found to be very hygroscopic and was stored inside a desiccator in an Argon atmosphere. The presence of even a small amount of water in the sample would make the experiment at high temperature incredibly difficult, as the fumes released by the hot salt would become very corrosive, degrading any metallic part in the experimental apparatus. This issue happened frequently and several parts of the apparatus had to be replaced. The issue was partially solved by purging the melt sample with argon for 10 minutes before conducting the measurement and by keeping an argon flow inside the measurement cell. The argon flow was interrupted slightly before conducting the measurements in order to decrease temperature fluctuations inside the cell. The measurements were taken with the same procedure applied to HTS and described in the previous paragraph, the only difference consisting in the flow of Argon injected in the apparatus. After the first results were analysed (see next Section), it was noted that different batches of measurements presented a higher volatility when compared to HTS. This was attributed to the purity of the sample, probably its moisture content, which seemed to have a significant effect. Much care was therefore taken to avoid contamination and to conduct all the steps necessary to prepare the sample in an inert atmosphere. Even if all those precautions helped and the quality of the results increased slightly, they did not fully solve the problem, as shown in the next Section.
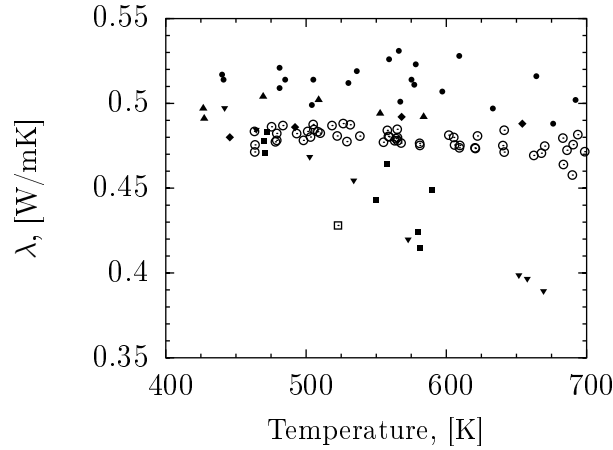
Figure 3.1: Thermal conductivity of HTS: (⊙), present study; (♦), Tufeu et al. [25]; (▲), Omotani et al. [40]; (●), Odawara et al. [53]; (■), Cooke [24]; (▼), Turnbull [27]; (□), Vargaftik [54].

3.2   Experiments: Results

3.2.1   Nitrates

The results of the thermal conductivity measurements performed on HTS are shown in Fig. 3.1 along with data found in the literature. In addition, in Table 6.3a we report the mean value of the measurements and their standard deviation over an interval of ± 10 K. The current data agree well with those of Tufeu et al. [25] who used a concentric-cylider, steady-state method [25]. Omotani et al. [40] used a method similar to the present one with a claimed accuracy of 3% [40]. Their data are approximately 3.5% lower than ours. Considering that the difference between these studies is approximately equal to their respective claimed accuracies, the agreement is more than acceptable.

The results of Odawara et al. [53] lie approximately 8% higher than the current measurements. Odawara et al. [53] used an optical method to measure the thermal conductivity of molten HTS and $NaNO_3$. In his study the thermal conductivity was derived indirectly from the thermal diffusivity of the salt, therefore it is possible that such data reduction introduced an additional uncertainty into the resulting data. It is worth noting that the results of Odawara et al. [53] with respect to

NaNO$_3$ are also higher (by approximately 10%) than the generally accepted values of Kitade et al. [55, 56].

The results of Cooke [24] at relatively low temperatures are very close to those in the present study, while the two studies do show deviations at higher temperatures. To further understand this discrepancy, we carefully reviewed the work done by Cooke. Fortunately the author reported in detail and with very good precision all the measurements, including raw data [24]. Cooke used a variable-gap apparatus consisting of two parallel heated-plates. The apparatus was used to measure the thermal resistance of the liquid between the two plates at different gaps between the plates. The thermal conductivity was then found by calculating the slope of the thermal resistance versus gap thickness curve. At around 470 K the thermal resistance was found to increase with remarkable linearly with the thickness of the gap. This allowed for an accurate calculation of the slope, and also suggested that external effects were negligible. At higher temperatures, on the other hand, the linearity is less clear. This different behaviour may be ascribed to secondary effects such as natural convection or additional heat losses. To overcome these effects, Cooke calculated the thermal conductivity by extrapolating the slope to zero gap thickness. In practice, the author calculated the slope from only the data points obtained using small gaps. The number of those data points was much lower than the overall set of data, and the choice concerning which data points to include in this exercise becomes, at least to some extent, relative. In addition, the relative error in measuring the thickness of the gap increases. The net result is a loss of accuracy and a larger scatter, as is visible in Fig. 3.1. Moreover, it is possible that the aforementioned secondary effects are exacerbating the departure from linearity, and these could also be present when the gap is small due to the elevated temperatures. In our opinion, these are possible reasons that can be used to explain the discrepancy with the current measurements. Nevertheless, Cooke [24] is an excellent effort, and we observed that whenever the linearity was reasonably conserved over the whole data range thanks to the lack of these issues,

Table 3.1: Mean standard deviation (SD) values of the measured thermal conductivity of HTS at different temperatures. The data statistics were compiled from a series of experiments/data points over an interval of $\pm\,10$ K around each state temperature.

Temp. [K]	λ [W/m K]	SD
471.7	0.479	0.0047
503.1	0.483	0.0026
527.3	0.483	0.0045
562.1	0.480	0.0026
606.4	0.477	0.0029
640.9	0.477	0.0054
666.8	0.471	0.0023
689.3	0.472	0.0078

Cooke's data are in very good agreement with ours.

Turnbull [27], as mentioned in Section 2.1 pioneered the application of the transient hot-wire method to molten salts by using a bare metallic wire with no electrical insulation. Current leakage is highly likely to have affected this measurement, as discussed by Omotani et al. [40]. Omotani et al. [40] also noted how previous measurements conducted by their group [39], and later discarded because of current leakage, led to results similar to the ones of Turnbull.

Furthermore, Vargaftik et al. [54] were the first to measure the thermal conductivity of HTS. Unfortunately, their measurement results seem unreliable as the calibration tests gave different results compared to the most widely accepted literature values [27].

Proceeding further, we can now propose the following relationship for the variation of the thermal conductivity of molten HTS with temperature:

$$\lambda = 0.382 + 3.85 \times 10^{-4}\,T - 3.72 \times 10^{-7}\,T^2 \qquad \text{for} \qquad 460\,\text{K} < T < 700\,\text{K}, \quad (3.1)$$

that was derived from a quadratic fitting to the values reported in Table 6.3a.

It is important to mention that the data seem to suggest a maximum thermal conductivity of about 0.483 over the approximate range $500\,\mathrm{K} < T < 530\,\mathrm{K}$, a behaviour also evidenced in the data of both Tufeu et al. [25] and Omotani et al. [40], as shown in Fig. 3.1. However, the deviation caused by such maximum from a simple linear fitting to the data is similar to the present experimental error and it is difficult to state definitively.

It is interesting to calculate the thermal conductivity of HTS as the molar average of the thermal conductivities of its pure constituent components. Unfortunately, only few data are available for $NaNO_2$, and over a limited range of temperatures. If the data of Tufeu et al. [25] are used, the thermal conductivity of HTS over the temperature range between 560 and 600 K (where data for $NaNO_2$ are available) is around 0.480 W/m K, which is less than 1% from the reported relationship above. This additive behaviour of the salt based on the constituent mole fractions, as pointed out in previous studies, e.g. Omotani et al. [40], seems to be confirmed by the present data.

Perhaps, one of the most interesting results was that steady-state methods like the ones used by Tufeu et al. [25] and Cooke [24] can successfully measure the thermal conductivity of molten salts, if properly applied. This finding is in partial contrast with the opinion by which steady-state methods are inevitably affected by large errors due to unavoidable natural convection in the salt. This topic will be discussed in more details in Section 3.3.

It is important to calculate the uncertainty of the thermal conductivity data of HTS, given hereby as the combined expanded uncertainty (95% confidence interval). The combined expanded uncertainty was calculated from the expanded uncertainty in the calculated value of the thermal conductivity and the expanded uncertainty in the drift from the true value caused by systematic errors. The expanded uncertainty in the calculated thermal conductivity was derived from the uncertainties of the measured quantities using Eq.2.9, and found to be 1.3%. The

major component of the uncertainty in the calculated thermal conductivity was found to arise from the term $\mathrm{d}\Delta T/\mathrm{d}\ln(t)$. It is important to note that any errors in the evaluation of the temperature dependence of the capillary resistance, $\mathrm{d}R_\mathrm{c}/\mathrm{d}T$, are embed in l_e and thus need not be considered independently.

The expanded uncertainty in the drift between the calculated and true value of thermal conductivity was evaluated by taking into account the systematic errors affecting the measurements below 430 K and other possible systematic errors arising at high temperature. The expanded uncertainty in the drift caused by the first group was considered equal to the maximum drift found when measuring standard fluids (equal to 2%). Regarding the second group, the only added major source of systematic error that we could identify at higher temperature was radiation.

Insightful studies into the effect of radiation were conducted by Menashe et al. [57] and Nieto De Castro et al. [58]. Nieto De Castro et al., in particular, showed that the error due to radiation in the transient hot-wire method could account for more than 3% of the total error. The effect of radiation induces a concave curvature in the plot of $\mathrm{d}\Delta T/\mathrm{d}\ln(t)$. In some of our measurements we indeed noticed a slight concave curvature. However the curvature was not pronounced and was difficult to detect, probably owing to the lower quality of the data and the different absorptivity of the salt. As a consequence, the analysis of Nieto De Castro et al. is difficult to apply to our study; a preliminary correction over those plots where the curvature was more visible indicated a maximum deviation of less than 0.7% from the present results. The expanded uncertainty caused by radiation was considered equal to this maximum deviation. The combined expanded uncertainty (95% confidence interval) of the present measurements was then calculated from the expanded uncertainty in the calculated value of the thermal conductivity, the expanded uncertainty in the drift from the true value found below 430 K, and the expanded uncertainty caused by radiation. Based on these values, the combined expanded uncertainty was found to be 3.1%.

3.2.2   Chlorides

The thermal conductivity of LiCl−KCl eutectic (0.557:0.443 molar fraction) was measured and compared with the values found in the literature, namely Smirnov et al. [35] and Gheribi et al. [59]; the results are displayed in Fig. 3.2 where each of the different datasets is shown using different colours. The Figure shows the poor repeatability between different sets of measurements (with respect to the measurements of HTS) conducted using samples prepared and used in different days. Unfortunately, the difference between the results of each dataset cannot be explained exhaustively at this stage and additional studies should be performed. In particular, the 5 different datasets were obtained using 3 different capillaries and 5 different samples. The use of almost one different probe for each dataset of measurements was due to the failure of the capillary connection at high temperature. We could argue, however, that the capillary does not influence the measurements, as this is was noticed during the measurements of HTS; also, the datasets obtained using the same capillary (green and red dots in Fig. 3.2) shows the same discrepancies seen between datasets conducted with different capillaries. Excluding the measurement system, it seems that the discrepancy are due to the sample preparation, storing and utilisation. Given the high variability and the limited knowledge about its cause the current measurements are not considered reliable. Further work will need to be conducted to confirm this hypothesis and achieve more reliable measurements.

Table 3.2 shows the data obtained with our method: their mean values and standard deviation over an interval of ± 10 K. The datasets show approximately the same dependence of the thermal conductivity with the temperature. A value of λ of 0.525 W/m K at 697.3 K agrees within a 10% error with the value of 0.569 W/m K estimated from a simple linear extrapolation of the data of Gheribi et al. [60], calculated using Equilibrium Molecular Dynamics (EMD). The values provided by Gheiribi et al. are part of a campaign initiated by the author to
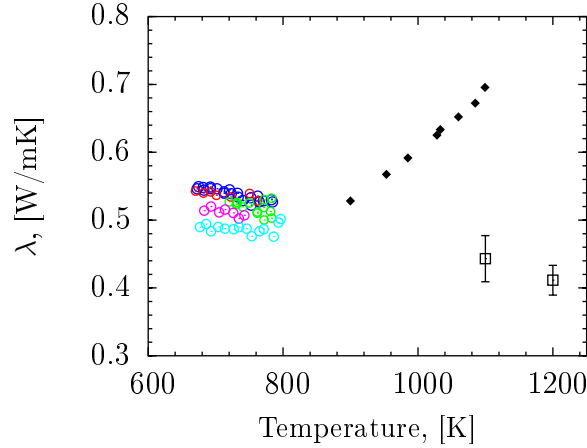
Figure 3.2: Thermal conductivity of LiCl−KCl (0.557:0.443 molar fraction): (⊙), present study, different colours correspond to different sets of measurements; (♦), Smirnov et al. [35]; (⊡), Gheribi et al. [60] (EMD).

calculate the thermal conductivity of molten salts from theoretical considerations and EMD, which has proven effective in recent publications (e.g. [59, 61]).

The present data are in disagreement with the experimental results of Smirnov et al. [35]. The measurements of Smirnov et al. are, however, considered unreliable as they have been compromised by the thermal losses in the steady-state measurement apparatus. A detailed discussion about this issue follows in Section 3.4. An evidence of their unreliability is their positive dependence of the thermal conductivity with temperature, which have now been proved to be erroneous [59].

Unlike for HTS, the temperature range in which thermal conductivity of LiCl−KCl was measured does not allow a comparison with the value of the thermal conductivities calculated from the molar average of its pure constituent salts. Indeed both LiCl and KCl present higher melting temperatures than the maximum temperature measured (778 K).

An estimation of the measurements uncertainty was conducted, similarly to HTS, from the expanded uncertainty in the calculated value of the thermal conductivity and the expanded uncertainty in the drift from the true value caused by systematic errors. The expanded uncertainty in the drift between the calculated and true value of thermal conductivity was taken, similarly to HTS, as given by the sum

Table 3.2: Mean standard deviation (SD) values of the measured thermal conductivity of LiCl–KCl (0.557:0.443 molar fraction) at different temperatures. The data statistics were compiled from a series of experiments/data points over an interval of ± 10 K around each state temperature.

Temp. [K]	λ [W/m K]	SD
678.8	0.530	0.0226
693.3	0.525	0.0235
719.2	0.522	0.0207
736.2	0.516	0.0166
757.5	0.518	0.0205
777.9	0.514	0.0168

of the trueness of the instrument below 430 K (2%) and the possible drift caused by the radiation error (0.7%). The expanded uncertainty in the calculated thermal conductivity, derived from the expanded uncertainties (95%) of the measured quantities using Eq.2.9, was 8.7%, much larger than for HTS. The major source of uncertainty was the poor reproducibility of the data. Using these values the overall expanded uncertainty of the values reported in Table 3.2 is 9.1%. It is important to mention however that, due to the poor reproducibility in the data, the results are considered unreliable.

3.3   Recommended values for the Thermal Conductivity of Molten Salts

In this section we conduct a critical review on the experimental works conducted to measure the thermal conductivity of molten salts. The goal of this review is to assess which values of the thermal conductivity can be considered more reliable and therefore recommended.

3.3.1   Review of the Measurements

The studies related to thermal conductivity measurements in molten salts are few in number and they can be essentially dived in two groups: steady-state and non steady-state measurements. The more recent non steady-state measurements were mostly conducted by Japanese experimentalists during the 1980s and 1990s, using contact-less methods (see Section 2.1 for more information); in particular, these measurements were the results of the efforts of few a groups of co-workers including Nagasaka et al. [42], Harada et al. [44], and Odawara et al. [53]. These measurements are widely considered more accurate than the ones obtained using steady-state methods and, as of today, they represent the most reliable values. Their accepted reliability depends upon different reasons: 1) They present a negative temperature dependence of the thermal conductivity (see a discussion in Gheribi et al. [61]; 2) they are in accordance with numerical and theoretical studies [62]; 3) they are consistent with other experimental studies conducted with other methods, including our own measurements of HTS. With respect to the steady-state methods, apart from few a cases [62, 25], most of the results seem unreliable [61]. To illustrate the scenario, we report in Fig. 3.3 all the available measurements of the thermal conductivity of KCl for which many measurements are available. The main reason for which to consider most of the steady-state measurements unreliable is the positive temperature coefficient of the thermal conductivity, which is contradictory to a supposed increase in lattice free volume due to a thermal expansion of the salt [61]. Also, the large discrepancies between similar studies, conducted with similar steady-state methods, is a clear sign of their the lack of reproducibility.

Different authors gave different arguments for the disagreement in the steady-state measurements. Generally they impute the cause of the disagreement to the natural convection present in the measurement cell which leads to an over-estimation of the real thermal conductivity [56]. Whatever the reason, this is an unfortunate
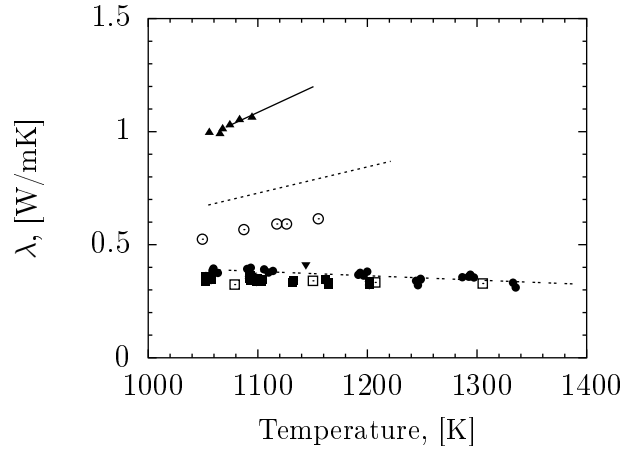
Figure 3.3: Thermal conductivity of KCl: (⊙), Smirnov et al. [35]; (■), Harada et al. [44]; (▲), Polyakov et al. [63]; (●), Nagasaka et al. [64]; (▼), McDonald and Davis [65]; (□), Hatakeyama [66];

scenario as many data were collected with this method and are only available from such studies. The case of FLiNaK is a good example of the present situation. FLiNaK is the eutectic mixture of LiF, NaF, and KF, currently proposed for the MSR. The value of the thermal conductivity of FLiNaK which is used nowadays is the one measured by Smirnov et al. [35]. The author in 1986 measured the thermal conductivity of various molten alkali halides, including FLiNaK. Smirnov found that the thermal conductivity of FLiNaK could be described by the following expression:

$$\lambda = 0.36 + 0.00056 \times T(K) \qquad (\text{W/mK}). \qquad (3.2)$$

The use of Eq. 3.2 has been re-proposed in recent studies (e.g. [67]), mainly because only these values are available in the literature and since Smirnov's studies no substantial progress has been made. A recent measurement [68], conducted by Khokhlov (collaborator of Smirnov's) obtained values similar to Smirnov et al. The apparatus used however was very similar to the one used by Smrinov et al. It is very likely that Eq. 3.2 is not accurate. As showed in Fig. 3.3, when Smirnov's results can be compared with more recent studies the disagreement is large (up to 80%). It is therefore likely that such disagreement exists also for FLiNaK and for those whose thermal conductivity was measured using only steady-state methods.

One of the most interesting results when conducting our own measurements was that steady-state methods, when properly designed, are not inevitably affected by natural convection, as other studies claims. In particular we found that the results of Tufeu et al. [25] and Cooke [24], which were conducted by using a small gap in the steady-state apparatus (<0.3 mm), were reliable. It can be therefore argued that where similar steady-state apparatuses were used but the results were unreliable, the source of error was not due to the natural convection but resided elsewhere. This conclusion is quite important for future experimental campaigns as it suggests that steady-state methods *can* be successfully applied to reliably measure the thermal conductivity of molten salts. Steady-state methods present a few but very important advantages over other methods like the one designed and used in this thesis: 1) they can be effectively applied at high temperature; 2) they are cheap and easy to build; 3) they are easy to utilise. These three advantages by themselves would make steady-state method a significant resource for the experimentalists if the reason for the source of their error is clearly recognised and therefore avoided.

In order to explore the problems regarding steady-state methods we specifically investigated the data obtained with these methods. We found that the steady-state measurements which gave reliable measurements had one particular feature in common: the steady-state thermal losses from the instrument were empirically estimated and taken into account [25]. To further elucidate this point the schematic of a steady state method, CCM, is offered in Fig. 3.4. As mentioned in Section 2.1 the CCM is based on imposing a power Q on an inner cylinder and measuring the steady-state temperature difference between such cylinder and on outer one. The thermal conductivity is then simply found by using the following equation:

$$\lambda = \frac{Q_{\text{tot}}\ln(R_2/R_1)}{2\pi H \Delta T},$$

(3.3)
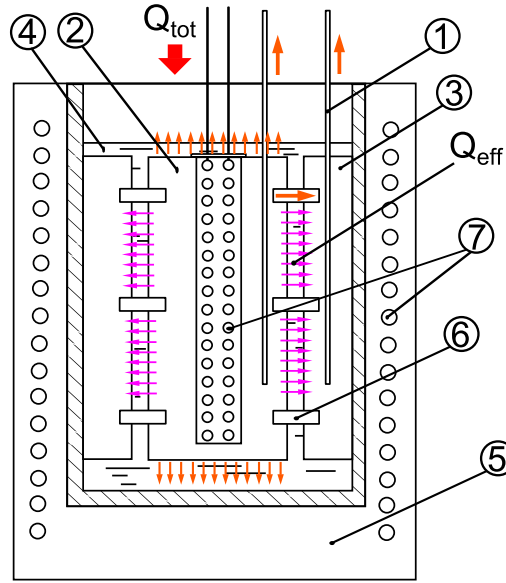
Figure 3.4: Schematic of CCM, showing: (1) thermocouple, (2) inner cylinder, (3) outer cylinder, (4) molten salt (sample), (5) furnace, and (6) spacers, (7) heating coils.

where Q is the total heat imposed, R_1 and R_2 the inner and out cylinder radius, H the cylinder height, and ΔT the temperature difference between the two cylinders. The power imposed is evaluated by measuring the voltage drop over a known resistor; this is indicated with the red arrow in Fig. 3.4. This power, however, is not exactly the one transferred through the salt. Indeed the presence of thermal losses through gap spacers (used to keep the gap space constant), thermocouples and end effects make the effective power through the gap (Q_{eff}) less than the one imposed. Different authors calculated the power losses by measuring the thermal conductivity of standard fluids and found that they can account for up to 30% of the total power [25]. Such thermal losses, if not considered, would explain why the steady-state methods overestimate the actual thermal conductivity of the salt. It is also probably that such losses increase with temperature because of the difficulty in properly thermally insulating the apparatus; this would explain the positive temperature coefficient of the thermal conductivity showed in many steady-state measurements.

In particular, Smirnov and co-workers did not take into account the thermal losses of the instrument and instead used the total power imposed to the instrument

in Eq. 3.3 [35], probably overestimating the thermal conductivity. Because of the relative simplicity by which the thermal losses have been taken into account in previous studies [25] and the large number of Smirnov's measurements, we decided to reprocess his data by trying to calculate and account such losses from his instrument.

3.3.2   Re-evaluation of Smirnov's Measurements

In order to take into account the thermal losses in Smirnov's experimental apparatus we first had to estimate them. Generally speaking, we can infer that:

$$Q_{\mathrm{tot}} = Q_{\mathrm{eff}} + Q_{\mathrm{loss}}, \tag{3.4}$$

where Q_{loss} are the thermal losses. It is important to understand that these are the thermal losses from the inner cylinder and not from the whole furnace containing the apparatus because, at the steady state, such losses are equal to Q_{tot}. Now, it is realistic to assume that the entity of such losses is a function of the difference in temperature between the inner cylinder and the temperature of the environment around this inner cylinder, which is approximately equal to the temperature of the outer cylinder:

$$Q_{\mathrm{loss}} = C_{\mathrm{loss}} \Delta T, \tag{3.5}$$

where C_{loss} is a constant which represents an average heat transfer coefficient multiplied by a constant area. The magnitude of C_{loss} is difficult to estimate as it is possibly composed by some temperature-independent terms (such as the spacers) and by other temperature-dependent terms. It is also possible that C_{loss} varies with the composition of the salt; this would make its estimation rather difficult. An idea of the magnitude of C_{loss} can be achieved by comparing Smirnov's measurements

with other authors' results which are considered more reliable. Indeed, supposing that we have a reliable value for the thermal conductivity, we can estimate the magnitude of C_{loss} by considering that

$$Q_{\text{tot}} = Q_{\text{eff}} + C_{\text{loss}}\Delta T, \tag{3.6}$$

and therefore

$$\frac{2\pi H \Delta T \lambda_{\text{meas}}}{\ln(R_2/R_1)} = Q_{\text{eff}} + C_{\text{loss}}\Delta T, \tag{3.7}$$

where λ_{meas} is the value of the thermal conductivity measured by Smirnov et al.

Taking a step further we can now consider the relation between Q_{eff} and the real thermal conductivity λ_{eff}:

$$\frac{2\pi H \Delta T \lambda_{\text{meas}}}{\ln(R_2/R_1)} = \frac{2\pi H \Delta T \lambda_{\text{eff}}}{\ln(R_2/R_1)} + C_{\text{loss}}\Delta T. \tag{3.8}$$

The previous expression can be simplified to:

$$C_{\text{loss}} = \frac{2\pi H}{\ln(R_2/R_1)}(\lambda_{\text{meas}} - \lambda_{\text{eff}}) \propto (\lambda_{\text{meas}} - \lambda_{\text{eff}}). \tag{3.9}$$

Rearranging Eq. 3.9 we obtain:

$$\lambda_{\text{meas}} - \lambda_{\text{eff}} = C_{\text{loss}}\frac{\ln(R_2/R_1)}{2\pi H} = \Delta\lambda_{\text{loss}}, \tag{3.10}$$

where the term $\Delta\lambda_{\text{loss}}$ is used, for simplicity, instead of C_{loss} to represent the thermal losses. Eq. 3.10 could seem obvious to a first impression, but is not. It entails that the difference between the measured thermal conductivity and the effective one is proportional to the thermal losses, which are usually constant in

an instrument (or dependent on the temperature at which the measurements are conducted).

From Eq. 3.10 we can estimate the value of the thermal losses $\Delta\lambda_{\mathrm{loss}}$ if reliable values of the thermal conductivity is provided. The hope is that such thermal losses are approximately constant with respect to the sample composition (type of molten salt measured). We conducted a literature review to ascertain which salts, measured by Smirnov et al., present reliable values of the thermal conductivity. The following criteria has been used to select the salts (and the relative experimental values) considered reliable: 1) measurements conducted by more than one author are available and agree to within 10%, preferably involving different measurement techniques; 2) data are qualitatively reliable and do not present abnormal behaviours such as positive temperature dependence; 3) data agrees within 10 % with theoretical studies. It turned out that such agreement can be inferred for specific salts in the literature, even if this is seldom the case. The salts found to respect the previous criteria were KCl, RbCl, NaBr, RbBr. In the following lines each of these salts, and suggested values of the thermal conductivity, are discussed in detail.

KCl. The case of KCl is quite fortunate as many data are available in the literature. The results of Bystrai [69], Fedorov et al. [70] and Polyakov [63] and the initial measurement of Smirnov et al.[35] were all obtained with the CCM method and are considered unreliable due to the thermal losses in the apparatus. The results of Harada [44], Nagasaka [64], Hatakeyama[44], and McDonald and Davis [65] are in good accordance with the general trend ($<$10% error). Hirada implemented the LFM while Hatakeyama and Nagasaka used the RSM. Nagasaka claims that his results are more reliable that the ones of Hatakeyama as the author used a more suitable dye ($K_2Cr_2O_7$) with increased reproducibility and accuracy [64]. The Results of McDonald and Davis were obtained using an insulated THWM but no information is given on the time window of their experiment and it is possible that they used, like Turnbull [27], a time window too large to avoid natural con-

vection in the sample; that would explain their positive temperature dependence. The theoretical values of Gheribi et al. [61] also correlate well with the overall trend. It is important to note however that the results of Gheribi were partially derived by "calibrating" their theoretical analysis on KCl, in a procedure similar to the present one. As such, the agreement with the other experimental data is expected. However the reliability of the values for KCl is partially endorsed by the good results which Gheribi et al. obtained for the other salts. For the purpose of our estimation of the thermal losses, the results of Hatakeyama, Harata et al. and Nagasaka et al. are all of good quality and similar. We have however considered accurate the value of Harada et al. The reason is that LFM does not need a dye which, as discussed in Section 2.1, is proved to add an error (see [64]). In addition the results of Harada et al. are basically the same as Hatakeyama et al. and in good accordance with McDonald and Davis (at around 1100 K).

RbCl. Measurements of RbCl were conducted by Bystrai et al. [69], Smirnov [35], Harada [44] and Nagasaka [64]. Similarly to KCl the data of Harada and Nagasaka are very similar while the stead-state methods overpredict the results. The agreement between Harada and Nagasaka, conducted with different methods, is here even better than for KCl and practically the two sets of data are equal. Those results were used for the estimation of the thermal losses.

NaBr. Another fortunate case is NaBr, for which the results of Harada et al. [44], McDonald and Davis [65] , and Nakazawa et al. [71] (co-worker of Nagasaka using the same method) are all in good agreement. Even if the average values agree very well between the authors, the scatter in the results is here worse than the previous cases and the repeatability is particularly poor in the work of Nakazawa et al. Their average values were used for the estimation of the thermal losses.

RbBr. Same situation as RbCl is presented by RbBr. The data of Harada [44] et al. and Nakazawa et al. [71] are in very good agreement while Smirnov et al. overestimates the results.
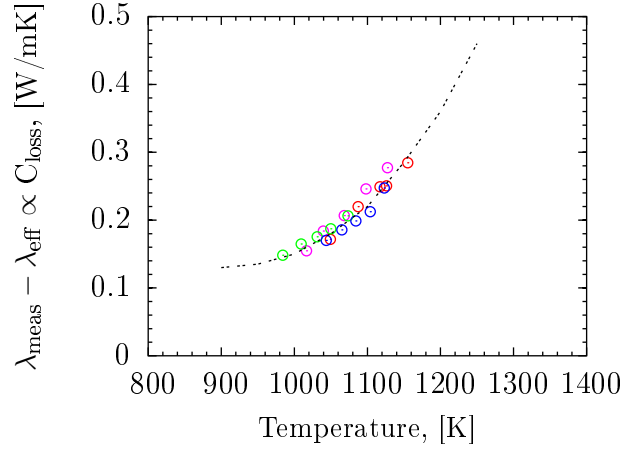
Figure 3.5: Estimation of $\lambda_{\text{meas}} - \lambda_{\text{eff}} \propto C_{\text{loss}}$ for different salts and the correlation used to estimate it.

The thermal losses $\Delta\lambda_{\text{eff}}$ were calculated using those reliable values of the thermal conductivity via Eq. 3.10; they are shown in Fig. 3.5. The small difference in the values of the calculated thermal losses between different salts is a favourable sign, suggesting that the properties of the sample (molten salt) do not change the magnitude of the thermal losses. The independence of the thermal losses on the sample is welcomed because it allows to calculate such losses for all other measurements, even when reliable data from the literature are absent. The thermal losses were correlated as a function of temperature (in K) with the following relation (also shown in Fig. 3.5):

$$\Delta\lambda_{\text{eff}} = 2.84 - 5.84 \cdot 10^{-3}\, T + 3.14 \cdot 10^{-5}\, T^2 \qquad (\text{W/mK}). \qquad (3.11)$$

This relation is considered valid for 900 K $< T <$ 1300 K. As shown in Fig. 3.5 the correlation does not cover only the temperature range for which reliable data of the thermal conductivity are present. It is also extrapolated (or better extended) to higher and lower temperatures ($T > 1180$ K and $T < 960$ K). It was possible to extrapolate the value of $\Delta\lambda_{\text{eff}}$ by a critical comparison with other salts outside the range: 960 K $< T <$ 1180 K, conducted by analysing the temperature coefficient of the thermal conductivity showed by λ_{eff}. It is however important to mention

that outside such range the uncertainty in evaluating $\Delta\lambda_{\text{eff}}$ is probably higher.

Through Eq. 3.11 and 3.10 it is possible to re-evaluate Smirnov's data to find the effective values of the thermal conductivity. The results of such re-evaluation are shown in Fig. 3.6–3.9 for Alkali Halides along with the data found in the literature. As shown by Fig. 3.6–3.9 the agreement between the newly calculated data and the literature is more than satisfactory and very welcome. The re-calculated values of Smirnov et al. are in accordance with the reliable data of Harada et al. [44] and Nagasaka et al. [64] basically for every salt, with an error usually well within 20%. The re-calculated values of Smirnov's et al. not only help to elucidate the literature but, for some important cases such as FLiNaK (not shown in the Figures) and Alkali Fluorides, represent the only reliable measurements available. These new data, along with the literature, were critically analysed to recommend new values of the thermal conductivity. Such analysis is explained in the next Section.

It is important to discuss the uncertainty of the re-calculated data of Smirnov's et al. The uncertainty of the values within the range 960 K $< T <$ 1180 K (for which an accurate quantification of $\Delta\lambda_{\text{eff}}$ was possible) were taken, for each salt, and in accordance with Ref. [52], as the sum of the maximum trueness (calculated from Fig. 3.5 as 3.8%) and the repeatability (standard deviation) of each measurement. For most measurements such uncertainty is within 10%. For the values outside the range 960 K $< T <$ 1180 K, the trueness of the measurements is more difficult to establish and a conservative value of 7% (instead of 3.8%) was considered.

3.3.3   Tabulated Values

The data in the literature were reviewed and compared in light of the new values found by our own measurements (Section 3.2) and the analysis of Smirnov's data. The new recommended values of the thermal conductivity are given in Table 3.3 for Alkali Halides and in Table 3.4 for other specific type of salts. The

(a) **LiF**: (⊙), Smirnov et al. [35]: original (white) and corrected (red); (▲), Ross et al. [72]; (●), Golyshev et al. (1992) [73]; (■), Golyshev et al. (1983) [74]; (▼), Screenivasan [75]; ——, Nagasaka et al. (theory) [62]; - - -, Gheribi et al. (theory) [61].

(b) **NaF**: (⊙), Smirnov et al. [35]: original (white) and corrected (red); (▼), Polyakov et al. [76]; ——, Nagasaka et al. (theory) [62]; - - -, Gheribi et al. (theory) [61].

(c) **KF**: (⊙), Smirnov et al. [35]: original (white) and corrected (red); ——, Nagasaka et al. (theory) [62]; - - -, Gheribi et al. (theory) [61].

(d) **RbF**: (⊙), Smirnov et al. [35]: original (white) and corrected (red); ——, Nagasaka et al. (theory) [62]; - - -, Gheribi et al. (theory) [61].

(e) **CsF**: (⊙), Smirnov et al. [35]: original (white) and corrected (red); ——, Nagasaka et al. [62]; - - -, Gheribi et al. (theory) [61].

Figure 3.6: Thermal Conductivity Measurements of Alkali Fluorides

(a) **LiCl**: (⊙), Smirnov et al. [35]: original (white) and corrected (red); (▲), Lucks et al., as reported by [61]; (●), Nagasaka et al. [64]; (■), Shurygin et al., as reported by [61]; (▼), McDonald and Davis [65]; (⊡), Bystrai et al. [77]; - - -, Gheribi et al. (theory) [61].

(b) **NaCl**: (⊙), Smirnov et al. [35]: original (white) and corrected (red); (◆), Harada et al. [44]; (▲), Turnbull et al. [27]; (●), Nagasaka et al. [64]; (■), Golyshev et al. [74]; (▼), McDonald and Davis [65]; ·····, Fedorov et al. [70]; - - -, Gheribi et al. (theory) [61].

(c) **KCl**: (⊙), Smirnov et al. [35]: original (white) and corrected (red); (◆), Harada et al. [44]; (▲), Polyakov et al. [63]; (●), Nagasaka et al. [64]; (▼), McDonald and Davis [65]; (⊡), Hatakeyama [66]; ·····, Fedorov et al. [70]; ——, Bystrai et al. [69]; - - -, Gheribi et al. (theory) [61].

(d) **RbCl**: (⊙), Smirnov et al. [35]: original (white) and corrected (red); (◆), Harada et al. [44]; (●), Nagasaka et al. [64]; ——, Bystrai et al. [69]; - - -, Gheribi et al. (theory) [61].

(e) **CsCl**:(⊙), Smirnov et al. [35]: original (white) and corrected (red); (●), Nagasaka et al. [64]; ——, Bystrai et al. [69]; - - -, Gheribi et al. (theory) [61].

Figure 3.7: Thermal Conductivity Measurements of Alkali Chlorides

(a) **LiBr**: (⊙), Smirnov et al. [35]: original (white) and corrected (red); (▲), Lucks et al., as reported by [61]; (▼), McDonald and Davis [65]; ——, Nagasaka et al. (theory) [62]; ---, Gheribi et al. (theory) [61].

(b) **NaBr**: (⊙), Smirnov et al. [35]: original (white) and corrected (red); (♦), Harada et al. [44]; (●), Nagasaka et al. [64]; (▼), McDonald and Davis [65]; ---, Gheribi et al. (theory) [61].

(c) **KBr**: (⊙), Smirnov et al. [35]: original (white) and corrected (red); (♦), Harada et al. [44]; (●), Nagasaka al. [64]; (▼), McDonald and Davis [65]; ---, Gheribi et al. (theory) [61].

(d) **RbBr**: (⊙), Smirnov et al. [35]: original (white) and corrected (red); (♦), Harada et al. [44]; (●), Nagasaka et al. [64]; ---, Gheribi et al. (theory) [61].

(e) **CsBr**: (⊙), Smirnov et al. [35]: original (white) and corrected (red); (♦), Harada et al. [44]; (●), Nagasaka et al. [64]; ---, Gheribi et al. (theory) [61].

Figure 3.8: Thermal Conductivity Measurements of Alkali Bromides

(a) **LiI**: ——, Nagasaka et al. (theory) [62]; - - -, Gheribi et al. (theory) [61].

(b) **NaI**: (⊙), Smirnov et al. [35]: original (white) and corrected (red); (♦), Harada et al. [44]; (●), Nagasaka et al. [64]; (▼), McDonald and Davis [65]; - - -, Gheribi et al. (theory) [61].

(c) **KI**: (⊙), Smirnov et al. [35]: original (white) and corrected (red); (♦), Harada et al. [44]; (●), Nagasaka et al. [64]; (▼), McDonald and Davis [65]; - - -, Gheribi et al. (theory) [61].

(d) **RbI**: (⊙), Smirnov et al. [35]: original (white) and corrected (red); (♦), Harada et al. [44]; (●), Nagasaka et al. [64]; - - -, Gheribi et al. (theory) [61].

(e) **CsI**: (⊙), Smirnov et al. [35]: original (white) and corrected (red); (●), Nagasaka et al. [64]; - - -, Gheribi et al. (theory) [61].

Figure 3.9: Thermal Conductivity Measurements of Alkali Iodides

values in table 3.3 were calculated by considering mainly the work of Smirnov's et al. (re-evaluated), Harada et al. [44], and Nagasaka and co-workers [64]. These works were assumed to be reliable, and often the difference in the values between these studies was less than the reported experimental errors. Other studies, such as McDonald and Davis [65], were also considered for specific salts. Specifically, the value reported (for each temperature interval) were an average of the values reported in each study considered reliable. The temperature at which values are given was chosen so that enough measurements were available to calculate meaningful statistics. When this was not possible, the uncertainty reported was marked with " * ". The reported uncertainty (95%) was taken equal to the reproducibility (95%) between the different studies, or, in other words, equal to the standard deviation of all the measurements obtained in a particular temperature interval. When only the values of one author were available (often the case of Smirnov's recalculated data), the reported uncertainty was conservatively taken equal to 20%. The value of 20% was chosen because it was found that basically all the re-calculated measurements of Smirnov's et al. were within 20% from the study of Harada et al. [44], and Nagasaka and co-workers [64]; as such, 20% is an indication of the maximum expected uncertainty. The maximum uncertainty of 20% reported in this work is much less than what is usually stated in the literature for molten salts. Also, reliable values regarding mixture of salts (mainly Chlorides and Fluorides) are now available. In the particular case of FLiNaK, the thermal conductivity at 1000 K was found to be 25% lower than the accepted value (based on Smirnov's original results) [78];

3.4   Heat Transfer Correlations of Molten Salt Flows

In this section we conducted an analysis of the applicability of standard heat-transfer correlations to molten salts in light of the new (and more reliable) values of the thermal conductivity. The validity of heat transfer correlations is essential

Table 3.3: Thermal conductivity of molten Alkali Halides (recommended values). References marked with " * " are considered best estimates due to the lack of data.

Salt	T K	λ [W/m K]	Uncertainty (95%)	Salt	T K	λ [W/m K]	Uncertainty (95%)
LiF	1125	1.27	8.5%	LiBr	896	0.436	8.7%
	1225	1.24	13.3%		1021	0.431	9.1%
	1376	1.19	18.9%		1221	0.402	9.8%
NaF	1276	0.72	20%*	NaBr	1028	0.309	4.7%
	1299	0.75	20%*		1122	0.305	3.9%
	1348	0.73	20%*		1265	0.294	5.0%
KF	1129	0.40	20%*	KBr	1023	0.235	4.9%
	1207	0.37	20%*		1196	0.211	4.3%
	1262	0.37	20%*		1246	0.207	5.5%
RbF	1092	0.31	20%*	RbBr	984	0.197	4.1%
	1198	0.29	20%*		1260	0.171	6.7%
	1241	0.26	20%*		1321	0.168	7.2%
CsF	981	0.24	20%*	CsBr	937	0.150	10.4%
	1155	0.21	20%*		1195	0.134	12.5%
	1245	0.17	20%*		1312	0.138	20%*
LiCl	960	0.65	10.3%	LiI	725	0.346	30%*
	1126	0.60	9.0%		1041	0.298	30%*
	1278	0.52	10.8%		1358	0.250	30%*
NaCl	1086	0.496	6.2%	NaI	960	0.220	8.0%
	1180	0.470	6.7%		1048	0.222	10.6%
	1340	0.437	6.3%		1109	0.218	10.6%*
KCl	1054	0.345	3.6%	KI	937	0.158	14.8%*
	1159	0.353	3.2%		1017	0.150	14.8%*
	1247	0.348	3.8%		1236	0.125	14.8%*
RbCl	994	0.271	4.1%	RbI	939	0.160	16.0%*
	1075	0.266	3.6%		1092	0.137	16.0%*
	1116	0.249	4.8%		1226	0.114	16.0%*
CsCl	917	0.189	4.7%	CsI	914	0.145	18.4%*
	1062	0.174	4.7%		1070	0.118	18.4%*
	1288	0.163	6.2%		1219	0.112	18.4%*

Table 3.4: Thermal conductivity of specific molten salts (recommended values). References marked with " * " are considered best estimates due to the lack of data.

Salt	T K	λ [W/mK]	Uncertainty (95%)
LiF−NaF	1140	1.01	20%*
(80.0:20.0)	1191	1.07	20%*
	1264	1.12	20%*
(60.0:40.0)	1163	0.90	20%*
	1220	0.95	20%*
	1268	0.97	20%*
(40.0:60.0)	1131	0.78	20%*
	1200	0.83	20%*
	1252	0.87	20%*
(20.0:80.0)	1219	0.77	20%*
	1261	0.80	20%*
	1304	0.80	20%*
LiF−KF	1079	0.89	20%*
(80.0:20.0)	1131	0.91	20%*
	1218	0.93	20%*
(60.0:40.0)	1090	0.78	20%*
	1137	0.79	20%*
	1217	0.79	20%*
(40.0:60.0)	1100	0.72	20%*
	1175	0.71	20%*
	1225	0.70	20%*
(20.0:80.0)	1098	0.63	20%*
	1147	0.63	20%*
	1220	0.60	20%*
LiF−NaF−KF	792	0.775	20%*
(46.5:11.5:42)	878	0.762	20%*
	1017	0.750	20%*
	1074	0.744	20%*
LiCl−KCl	678	0.541	7.3%
(55.7:44.3)	776	0.520	7.3%
	900	0.415	20%*
	1027	0.454	20%*
	1098	0.470	20%*
NaCl−KCl	1015	0.360	20%*
(50.0:50.0)	1069	0.373	20%*
	1122	0.367	20%*

to conduct any thermo-hydraulic modelling. Molten salts are considered as Newtonian fluid, therefore standard correlations should be applicable in theory. An analysis of the work was however deemed necessary to be assured that heat transfer correlations can be incorporated with reliability (within 20% error) into numerical models. For a Newtonian fluid, such as water, the thermo-hydraulic behaviour is well described by correlations involving dimensionless numbers. For example, the heat transfer in a turbulent pipe flow can be described by the Dittus-Boelter (DB) equation:

$$Nu = 0.023 Re^{4/5} Pr^{0.4}. \tag{3.12}$$

In this equation Nu, Re, and Pr are respectively the Nusselt, Reynolds and Prandtl number. Studies have been conducted to see if the previous correlations can be applied to molten salts. From the beginning of the Molten Salt Reactor Experiment in the 1960s, many authors have experimentally monitored the heat transfer of molten salts (particularly FLiNaK) in pipe flow. The experiments generally consisted in electrically heating the wall of a pipe in which molten salts are pumped. The power and the temperature of the salt at the inlet and exit of the pipe are measured; from such measurements, and the knowledge of the thermal properties, it is possible to calculate the heat transfer coefficient between the wall and the liquid salts, and therefore to check the validity of Eq. 3.12. Because of several issues in conducting these type of experiments, only the simplest geometries, namely pipe flows, have been considered by the literature. The first studies have been carried out by Grele et al. and Hoffman et al. at Oak Ridge National Laboratories using FLiNaK [79, 80, 81]; later, Vriesema and Silverman repeated and extended the measurements [82, 83]. More recently, new measurements have been obtained using other type of salts [84]. An insightful study has been conducted by Wu et al. [85], in which the author confronted several kinds of molten salts and concluded that, as a general rule, the usual correlations for heat transfer in pipe flow can be applied to molten salts within 25% error.

Because the thermal properties are required to calculate the dimensionless number of Eq. 3.12, the correct evaluation of any heat-transfer correlation is based on the knowledge of the thermal conductivity. Previous authors used values which were substantially different from the now accepted ones. In particular for FLiNaK, they used a value of λ of approximately 4.5 W/m K which is 500% higher than the one found in this work (see Section 3.3). From these initial studies it was therefore very dubious if Eq. 3.12 could be applied to molten salts, as it seemed to largely over predict the heat transfer in many cases. Ambrosek et al. [67, 86] recently studied this issue by reprocessing previous data using the thermal conductivity of Smirnov et al. (which, even if unreliable still is an order of magnitude different from the value of 4.5 W/m K). Ambrosek et al. concluded that molten salts can be considered Newtonian fluids, even if some experiments largely departed from the standard relation. Following the work of Ambrosek et al. we reprocessed the previous data using the more accurate value reported in this study, which is around 15-25% lower than the one used by author [67]. The values of the thermo-physical properties used in the various studies, with the exception of the thermal conductivity, were taken as reported from the study of Ambrosek et al.. Fig 3.10 reports the re-calculated measurements of Vriesema et al. [82] Grele et al. [79] and Hoffman et al. [80], along with the DB correlation.

The DB correlation was found to underpredict the experimentally measured heat transfer coefficient. The average deviation between the experimental data and the DB correlation is less than 20%, which is typical for heat transfer correlations. Considering the uncertainties present in the measurements, molten FLiNaK was confirmed to behave as a Newtonian fluid, as stated by previous literature [82, 67].
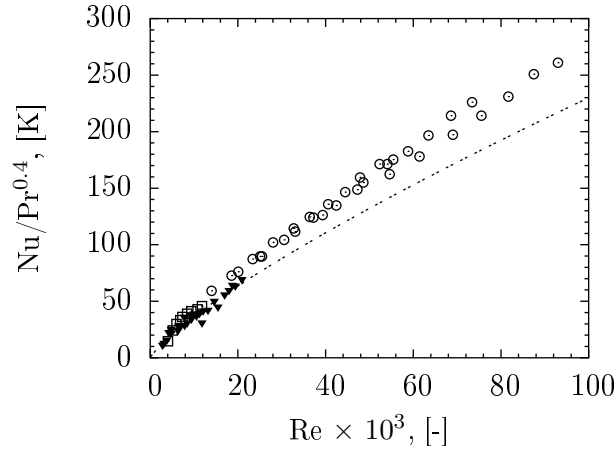
Figure 3.10: Results of the heat transfer experiments using FLiNaK re-calculated using the new values of the thermal conductivity, as indicated by Ambrosek et al. [67]. (⊙), Vriesema et al. [82]; (▼), Grele et al. [79]; (⊡), Hoffman et al. [80]; (--), DB correlation (Eq. 3.12).

3.5 Conclusions Chapter 3

The overall aim of this Chapter is to recommend suitable values of the thermal conductivity of molten salts, which can be then used in thermo-hydraulic models to make reliable predictions. The following conclusions can be inferred:

- Measurements of HTS and LiCl–KCl eutectic were conducted up to approximately 775 K (500 °C). The thermal conductivity of HTS was found to range from 0.48 W/m K at 500 K to 0.47 W/m K at close to 700 K, with a reported expanded uncertainty (95% confidence interval) of 3.1%. The thermal conductivity of LiCl–KCl was more difficult to measure and was found to range from 0.53 W/m K at 680 K to 0.51 W/m K at close to 780 K, with a reported expanded uncertainty (95% confidence interval) of 9.1%. The measurements of LiCl–KCl are considered unreliable due to the higher scatter in the data, which was found to be due to the purity of the sample.

- Contrary to the general opinion we found that steady-state method can be very accurate when properly designed and used. We have re-evaluated with a simple procedure the measurements of Smirnov et al. by accounting for

the thermal losses in the instrument. The new re-evaluated data showed to be very reasonable (negative temperature coefficient) and highly consistent with respect to the literature.

- We carefully reviewed the literature regarding thermal conductivity data and included the new measurements, as well as the newly re-evaluated data of Smirnov's et al. Thanks to this analysis, the uncertainty on the thermal conductivity of most common salts (including FLiNaK was found by this work to be less than 20%, compared with the 10%-80% of previous literature.

The new values of the thermal conductivity were used to reprocess the experimental data of heat transfer experiments, in a similar manner to Ambrosek et al. [67]. Molten salts were confirmed to behave as Newtonian fluids following the Dittus-Boelter (DB) correlation.

Chapter 4

Modelling Transient Freezing in Piping Systems

In this Chapter a model is developed to predict transient freezing in internal flow. As mentioned in the introduction, this condition is nowadays of importance, given the increased use of high temperature melts, but it is not, or only approximately, considered by standard thermo-hydraulic codes. The objective of this chapter is to present a model which was derived with the purpose to simulate transient freezing in complex piping systems, with the following characteristics: (1) able to quantify (within 30%) the solid build-up, heat transfer coefficients, temperatures and flow-rates; (2) easily applicable in standard thermo-hydraulics codes for the analysis of industrial piping systems.

4.1   Previous Works

As briefly mentioned in the introduction, the problem of freezing/solidification has been analysed by many authors over the last century. In the following lines we briefly indicate some of the most important theoretical and experimental works, referring to Ref. [14], [13] and [87] for a more comprehensive discussion.

The pioneers in tackling freezing were probably Stefan and Neumann, which studied and described mathematically the solidification of a stagnant fluid in contact with an isothermal wall. This problem was named the Stefan-Neumann problem and comprises three equations: two heat conduction equations through the fluid and the freezing layer and an energy conservation equation at the interface. This is probably the most simple problem of freezing. In general other conditions make this problem far more complicated, especially because all the moving-interface problems are, generally speaking, non-linear and singular (due to the presence of an interface). Such moving interface problems were later generally referred to as "Stefan-type" problems. In the work described in this thesis we focus on freezing with internal flow which, being a moving interface problem, is also considered a Stefan-type problem and, indeed, it shares many features with the original Stefan-Neumann problem.

With respect to the experimental work regarding freezing with internal flow, the pioneers were Zerkle and Sunderland, who studied both experimentally and theoretically the steady-state freezing of water in pipe flow [88]. Their experiment is described in detail in Zerkle's PhD thesis [89]. Two sets of experiments were conducted by Zerkle and Sunderland, one focused on the visual observation of solid/liquid interface and the other on steady-state measurements. Fig. 4.1 depicts the steady-state profile found by the author for a fluid solidified on a cold surface. As visible in the picture, there is a thermal entry region where the solidified layer is thin; further right, the thickness of the layer becomes constant.

The authors compared the steady-state profile with the theoretical one described by the relevant Stefan-type problem. One of the results of the comparison was that free convection in the developing thermal boundary layer made the heat transfer greater in this region. As a consequence the layer was thinner where it begins to form than what the theory predicted. The steady-state curvature of the ice layer profile agrees with the theory if the free-convection heat transfer coefficient developed by Oliver [90] is used instead of standard laminar flow correlations.
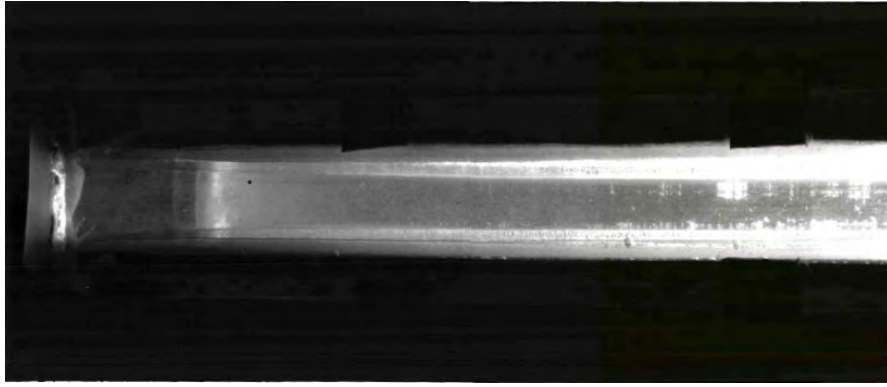
Figure 4.1: Photograph of the ice layer profile in the experiment conducted by Zerkle. Image taken from [89].

Zerkle and Sunderland therefore found how an accurate knowledge of the heat-transfer coefficient and, consequently, of the fluid velocity profile which drives it, is essential to make accurate predictions of the freezing process. Another result of the experimental study was that the pressure drop was extremely sensitive to the presence of the ice layer. This can be ascribed to the change in viscosity due to the drop of the fluid temperature at the wall. The increase in pressure drop is therefore more evident when the fluid is significantly superheated (when it has a temperature much higher than the melting temperature).

Following the work of Zerkle and Sunderland, other similar, steady-state, experiments with water were performed, namely [91], [92] and [93]. These studies, as in [88], mainly focused on steady-state measurements of the ice layer profile and their comparison with the theory. A practical approach to the problem of freezing came from the study of DesRuisseaux and Zerkle [94], which developed a technique to predict when an hydraulic system freezes shut, meaning complete blockage of the flow. Specifically, the authors indicated, as a function of the process variables, the minimum pressure which needs to be maintained across a pipe to avoid freeze shut of the liquid in contact with a wall at a uniform and constant cold temperature. Successive studies also focused on predicting when a water pipe flow freezes shut. Different conditions were analysed in these studies, one important example being Arora, who studied the problem in turbulent flow [95].

All the mentioned studies focused on providing criteria for a steady-state analysis of the conditions in a pipe; as such they are of limited use with respect to a transient analysis. The problem of transient freezing indeed did not receive much attention and most studies focused on its analytical and numerical treatment. Ozisik developed a system of transient equations to study the problem [96] and allow predictions of whether a pipe will freeze shut or not. The author calculated that blockage is important only in problems involving flows from a reservoir at constant pressure with insufficient super-heating; this however is a condition often incurred in when dealing with molten salt systems. Martinez [97] and Savino et al. [98] also developed an analytical model to simulate transient freezing. Because of its relevance to our study, the work of Savino, which conducted experiments along with the theoretical study, will be discussed more in detail Chapter 5. There are however some difficulties in applying the results of these last two mentioned works to practical applications. First, the boundary conditions analysed both in the experiment and in the theory differ from the ones encountered in molten salt applications. An example is the zero wall heat capacity assumption used by the mentioned authors, which in molten salt systems is unrealistic, given the possibility of large thermal excursions. As we will show in the next Chapter the application of these codes to our experimental data does not successfully predict the behaviour. Another difficulty is also the complex treatment of the equations which make their implementation in codes computationally hard.

With respect to the research conducted in most recent years, the general trend in the literature was to favour the development of numerical tools, like CFD, which greatly improved our prediction capabilities. However limited work has been conducted on internal flow with transient freezing. Almost the totality of CFD studies on solidification/melting were indeed conducted for phase change materials (PCMs) applications, such as thermal energy storage, and do not involve forced convection or internal flow. Also the increase in numerical prediction capabilities came at the expenses of the experimental efforts, with new experiments being rare

and usually limited to natural convection.

As a completion of this brief literature survey, we mention also the studies undertaken on freezing in turbulent flows. These studies showed that the otherwise uniform layer of salt, in the case of turbulent flow, can present ice-band structures in the form of waves (for relatively high Reynolds numbers). Such structures are particularly important because they severely increase the pressure drop in the piping. On this matter, important are the works of Gilpin [99] and Hirata [100]. More recently, Weigand also studied the formation of such structures in a noozle [101]. Because the flows considered in most molten salt applications do not usually present a high Reynolds number, we did not consider such an eventuality in our study.

The scientific research mentioned so far and briefly summarised was mainly motivated by both the interesting mathematical formulation of the freezing problem and the need to predict the freezing of water flow in domestic as well as industrial applications (e.g. food conservation). As such, the formulation of the problem which was mostly analysed was very specific and, as briefly mentioned before, unrelated to the practical conditions found in molten salt units operation. To summarise, the main differences between the studied problems and those one encountered in molten salt applications are: (1) apart from few notable exceptions, all the experimental studies focused on steady-state analysis which are unsuitable to make predictions in real transient systems. (2) The theoretical solutions proposed are highly computationally expensive and difficult to apply to calculate the behaviour of large piping systems. In addition to this, most of such theoretical works on transient problems do not offer any experimental validation. (3) Almost all the experimental and theoretical work dealt with boundary conditions typical of freezing water, such as low thermal capacity of the fluid, low heat transfer rate at the wall and low thermal capacity of the wall. We therefore decided to develop a model, which we will describe in the next section, with the specific purpose to address these issues.

4.2   Freezing Model

We developed a 1-Dimensional freezing model with the precise goal of applying it to complex piping networks. We also wanted the model to be capable of being easily incorporated in standard 1-Dimensional thermo-hydraulic codes. Taking pipe flow as a reference, the liquid is supposed to start freezing when the temperature of the wall T_w, assumed to be uniform, falls below the melting temperature of the liquid T_{melt}. The solidification of the salt is modelled by assuming the formation of an azimuthally uniform annular layer of solidified salt around the pipe wall perimeter (with a flow of liquid salt in the core of the pipe). To reduce the computational complexity we did not opt for modelling multiple sub-layers in the solidified layer of salt. Instead, the presence of a solidified layer was taken into account by adding specific terms to the energy balance and mass balance in the ordinary thermo-hydraulic equations. In the following lines a detailed discussion on this approach is given. First however, we discuss briefly the assumption of the formation of a solid layer. This is not always the case as the solidified material could be detached from the wall by friction forces and end up in the bulk of the fluid. In this condition freezing would be a bulk-phenomena resulting in the formation of a slug. The occurrence or not of this condition would depend on the adhesion forces between the type of salt and the wall material used. We did not take into account this condition in our work as it is much easier to treat and results in safer scenarios as freezing is greatly delayed.

For our treatment we assumed a pipe divided across its length in elements of length ds. In each of these elements, freezing is modelled independently by assuming the formation of a layer of solid fluid of thickness X_s, function of the mass of salt solidified per unit length m_s. The relation between X_s and m_s depends on the geometry of the flow section; for a pipe it is

$$m_\mathrm{s} = \rho_s \pi [R_0^2 - (R_0 - X_s)^2] = \rho_s \pi (R_0^2 - R(m_\mathrm{s})^2), \qquad (4.1)$$

where ρ_s is the density of solid salt, R_0 is the pipe radius and $R(m_\text{s})$ the reduced radius of the pipe available to the fluid due to the mass of solidified salt. The interface between the solid and fluid phases is assumed to be at the melting point of the material. The mass of solidified salt per unit length is found through an energy balance over the whole layer of solid:

$$\left[\Delta H + (T - T_\text{melt})c_\text{p} + \psi(m_\text{s}, T_\text{w}) \right] \frac{\partial m_\text{s}}{\partial t} = h(T - T_\text{melt})P - q_\text{sf}P_\text{w} \,, \qquad (4.2)$$

On the right hand side of Eq. 4.2 two terms are present which represent the heat fluxes at the boundaries of the solidified layer respectively for the fluid side (first term) and wall side (second term); h is the liquid-side heat transfer coefficient, P is the perimeter of the cross sectional area of the pipe available to the liquid, P_w is the wall perimeter (P equals P_w when no solidified material is present), and q_sf is the solid-side heat flux at the interface between the liquid/molten salt and the solidified mass of salt. Looking at the left hand side of Eq. 4.2 all the terms in the square bracket represent various contributions to the energy required to melt/solidify a mass of salt per unit length m_s. The first term, ΔH, is the enthalpy of fusion. The second term is the enthalpy difference between the fluid at its melting point and the bulk of the fluid, c_p being the specific heat, T the bulk temperature and T_melt the melting temperature; such energy is required to cool/heat a mass of fluid before/after it is melt. The third term, $\psi(m_\text{s}, T_\text{w})$, represents the thermal energy loss/gained in the layer of solidified salt due to a change in its mass per unit length m_s. The coloured area in Fig. 4.2 represents this last energetic contribution in melting/solidifying a mass of salt per unit length m_s.

The expression for $\psi(m_\text{s}, T_\text{w})$ is calculated by Taylor expansion of the thermal energy (E_s) differential in the solid layer caused by the solidification of a mass per unit length δm_s and assuming quasi-steady temperature profiles in the salt, such that:
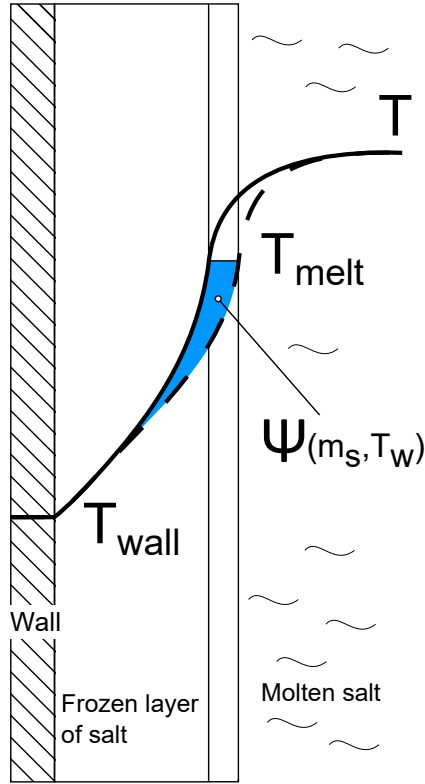
Figure 4.2: Schematic of the temperature profiles across the liquid salt, frozen layer and wall. The blue area corresponds to $\psi(m_\text{s}, T_\text{w})$ and represents the thermal energy lost or gained in the layer of solidified salt due to a change in its mass per unit length m_s.

$$\psi(m_\text{s}, T_\text{w}) = \frac{\partial E_\text{s}}{\partial m_\text{s}} \simeq \frac{\delta E_\text{s}}{\delta m_\text{s}}. \tag{4.3}$$

For a pipe of radius R_0 the expression for $\psi(m_\text{s}, T_\text{w})$ is

$$\psi(m_\text{s}, T_\text{w})) = c_\text{p}(T_\text{melt} - T_\text{w}) \left[\frac{1}{2} \ln \left\{ \frac{R_0}{R(m_\text{s})} \right\} + \frac{1}{4} \left\{ \ln \frac{R_0}{R(m_\text{s})} \right\}^2 + \frac{1}{4} \left\{ \ln \frac{R_0}{R(m_\text{s})} \right\}^2 \frac{R_0^2}{R(m_\text{s})^2} \right]. \tag{4.4}$$

Eq. 4.2, combined with Eq. 4.1 and Eq. 4.4, are used to calculate the mass of solidified salt per unit length in each element of pipe. The addition of these equations in standard thermo-hydraulic code is enough to model the occurrence of a freezing layer in a piping system. If the wall temperature is not fixed and is, instead, calculated through and energy balance, such energy balance needs to be

modified to account for the presence of the solidified layer of fluid. As an example
of this approach, the energy balance used to calculate the wall temperature T_w in
our code simulating the molten salt reactor piping system is:

$$(A_w \rho_w c_{p_w}) \frac{\partial T_w}{\partial t} + \xi(m_s) \frac{\partial T_w}{\partial t} = -h_{ext}(T_w - T_{ext})P_{ext} - q_{sw}P_w \,. \qquad (4.5)$$

Here, the subscripts "w" and "ext" indicate, respectively, the conditions on the in-
side/internal wall of the pipe (in contact with the salt) and on the outside/external
wall of the pipe. A_w is the pipe cross sectional area and q_{sw} is the heat flux to
the wall from the solidified mass of salt. The term $\xi(m_s)$ has a similar role to
$\psi(m_s, T_w)$ and is function of the mass of salt solidified per unit length m_s. This
term accounts for the thermal energy lost or gained in the layer of solidified salt
due to a change in T_w. Indeed the energy required to raise the wall tempera-
ture must account for the mass of solidified salt in contact with it. The energetic
contribution is shown by the coloured area in Fig. 4.3.

The function $\xi(m_s)$ is calculated by assuming a quasi-steady temperature profile
in the salt and by expanding the thermal energy (E_s) differential in the solid layer
caused by an increase in the wall temperature δT_w and taking only the first order
term:

$$\xi(m_s) = c_p \rho \pi \left[\frac{R(m_s)^2 - R_0^2}{2} \ln \left\{ \frac{R(m_s)}{R_0} \right\} + R_0^2 \right] \,. \qquad (4.6)$$

Eqs. 4.1–4.6 define the freezing model and are used, in the next Chapters to
simulate the solidification of fluids during internal flow.
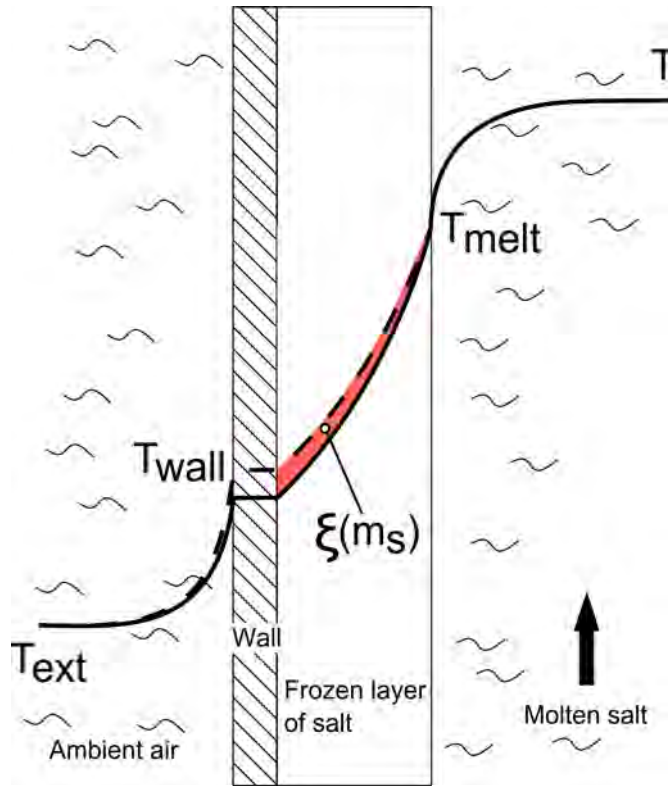
Figure 4.3: Schematic of the temperature profiles across the liquid salt, frozen layer and outside air. The red area corresponds to $\xi(m_{\mathrm{s}})$ and represents the thermal energy lost or gained in the layer of solidified salt due to a change in T_{w}.

4.3   Checking the Consistency of the Model with Theory

The model described in the previous Section was compared with the results derived from theory to understand its applicably limits. Analytical and numerical solutions of relatively simple, "Stefan-like" problems are available to benchmark the model. These analytical problems were derived to calculate the formation of a solidified layer upon freezing of a liquid. Strong assumptions are usually used, such as neglecting the heat capacity of the solid layer and the wall; the model developed in the previous section was then modified to describe freezing under these simplifying conditions.

The analytical, Stefan-like problem hereby considered was the one closest to real applications and involves an infinite solidified layer of thickness X_{s}, initially sup-

posed of zero thickness, with both sides in contact with two fluids, the first being the fluid solidifying and the second being immiscible and providing the cooling power. The two fluids have constant bulk temperatures T_l and T_{ext} respectively for the fluids solidifying and the fluid providing cooling power. The heat transfer between the fluid and the solidified layer is regulated by means of constant and uniform heat fluxes h_l and h_{ext}. The problem is formulated as follows:

$$\frac{\partial T}{\partial t} = \alpha_s \frac{\partial^2 T}{\partial x^2} \qquad \qquad 0 < x < X_s(t), t > 0 \quad \text{heat equation}$$

$$k_s \frac{\partial T}{\partial x}(0,t) = h_{ext}(T(0,t) - T_{ext}) \qquad t > 0 \qquad \qquad \text{boundary condition}$$
on the left

$$T(X_s(t), t) = 0, \qquad \qquad t > 0 \qquad \qquad \text{melting temeperature at}$$
the water/solid interface

$$\rho_s \Delta H \frac{\partial X_s}{\partial t} = -h_l(T_l - T_{melt}) + k_s \frac{\partial T}{\partial x}(X_s(t), t) \quad t > 0 \qquad \text{Stefan condition}$$

$$T(x, 0) = T_{melt} \qquad \qquad 0 < x < X_s(t) \qquad \text{initial temperature}$$
distribution

$$X(0) = 0 \qquad \qquad \qquad \text{initial layer thickness}$$

$$(4.7)$$

The terms α_s, k_s, ρ_s, ΔH represent respectively the thermal diffusivity, thermal conductivity, density and heat of fusion of the solidified salt and are assumed to be constant. The steady-state solution of this problem is readily found by solving for the steady-state thickness $X_s(t \to \infty)$:

$$X_s(t \to \infty) = \frac{k_s}{h_l} \frac{T_{melt} - T_{ext}}{T_l - T_{melt}} - \frac{k_s}{h_{ext}}. \qquad (4.8)$$

A numerical solution to this problem was offered by Goodman [102]. Hereby we compared the transient solution found by Goodman with the approximated solution calculated by the model. The values of the physical properties of the solidified layer were chosen similar to the ones typical of a molten eutectic of chlorides. The boundary condition used were also similar to the ones which could be found in a practical application, such as in a molten salt/air heat exchanger: $h_{ext} = 150$, $T_{ext} = 60$ °C and $h_l = 500$. Fig. 4.4 shows the results of the model
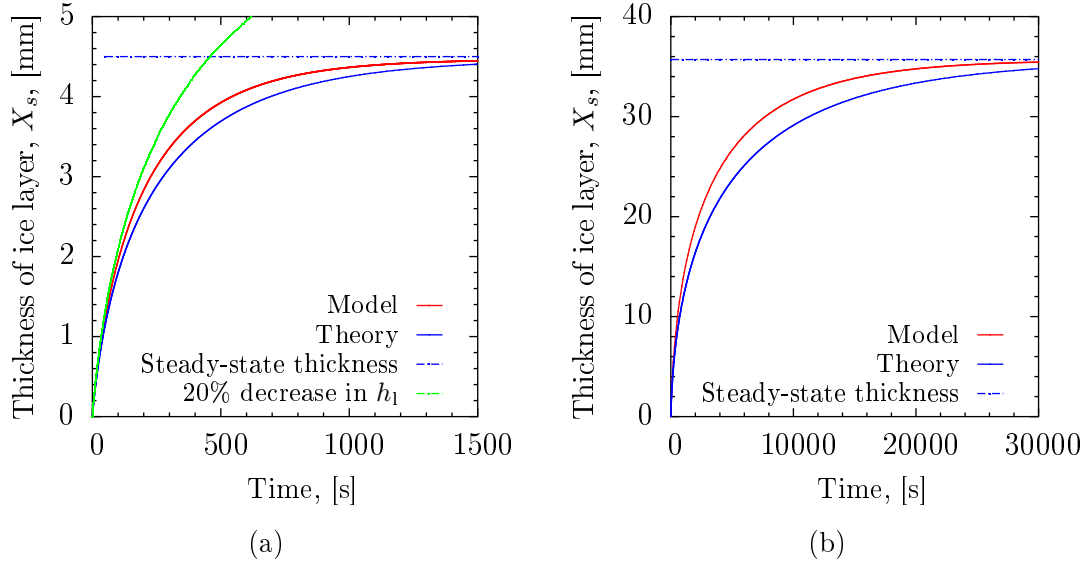
Figure 4.4: Theoretical and simulated solidified layer thickness versus time. The problem solved is defined by Eq.4.7 for molten chlorides eutectic with $h_{ext} = 150$, $T_{ext} = 60$ °C and $h_l = 500$, for values of super-heating (T_l - T_{melt}) of: a) 50 °C, b) 10 °C.

compared with theory for two indicative cases with values of super-heating (T_l - T_{melt}) of 50 °C and 10 °C respectively.

As shown in the figures, the model tends to over-predict the theoretical solution. This is explained by the use of a steady-state temperature profile in the layer of solidified salt. Because of this assumption, the temperature information across the solidified layer travels with infinite speed which results in a higher degree of heat removal with respect to the ideal solution. The overestimation is therefore worse the thicker is the solid layer; this can be seen by comparing Fig. 4.4a and Fig. 4.4b. The error induced by the model with respect to theory is estimated to be however less than 10% for all practical cases, which is a good trade-off given its simplicity. In addition the disagreement between the model and the theory is insignificant if related to other errors, such as the ones derived from the uncertainties in the values of the thermal properties or the heat transfer coefficient used. The green line in Fig. 4.4a shows the effect of a 20% decrease in the value of the fluid heat transfer coefficient. As shown, the resulting difference is higher than the difference between the model and the theory. Fig. 4.4a also demonstrates

the importance of accurately knowing the value of the thermal conductivity of the liquid phase. Indeed, at low Reynolds numbers, a 20% error in the value of the thermal conductivity will result in a respective error in the value of the heat transfer coefficient, significantly overestimating or underestimating the growth of the solid layer. As mentioned in the introduction it is therefore of paramount importance the use of accurate values of the liquid thermal conductivity, which was the motivation behind the work undertaken in Chapters 2 and 3.

4.4   Model of the Piping Systems (DRACS)

The freezing model described in the previous section can be easily incorporated in standard thermo-hydraulic codes. In this section we give an example of such codes, which has been applied to model the piping system of DRACS (the results of such analysis are described in Chapter 6). We refer to the schematic in Fig. 6.1 and the relevant discussion in Section 6.1, in Chapter 6, for additional details regarding DRACS. The present model is a system of non-linear, partial differential equations (PDEs) whose main variables are the temperatures and flow-rates in the piping system (in this case the two DRACS loops), which need to be solved in space and time. The piping system is modelled by using a one-dimensional (1-D) approach with the spatial coordinate s representing the position along the axis (in the flow direction).

The assumptions used to derive the equations are: (1) the flows are incompressible, (2) the Boussinesq approximation is valid, (3) axial heat conduction is negligible, (4) heat transfer coefficient correlations can be used under quasi-steady conditions, and (5) viscous heat dissipation is negligible. The fundamental equations are presented below.

From assumption (1), the continuity equation applied on a piping system reduces

to:

$$\frac{\mathrm{d}W}{\mathrm{d}s} = 0\,, \tag{4.9}$$

where W is the mass flow-rate, which is, therefore, only a function of time. This equation was used even in the case of liquid freezing for simplicity.

In addition, and considering assumption (2), the equation of momentum conservation for a pipe section of length $\mathrm{d}s$ can be written as:

$$\frac{\mathrm{d}W}{\mathrm{d}t}\frac{1}{A} = g\rho\{1 - \beta(T - T_0)\} - \frac{(\tau_{\mathrm{w}})P}{A} - \frac{\mathrm{d}p}{\mathrm{d}s}\,, \tag{4.10}$$

where ρ, β, T and p are the density, coefficient of thermal expansion, temperature and pressure of the (liquid, molten) salt; g is the gravitational acceleration; A and P are the cross-sectional area and wetted perimeter of the pipe flow, and τ_{w} is the wall shear stress. It is important to note that A, P and τ_{w} are, generally speaking, functions of the position in the loop, due to the different geometry present in each loop section and the possibility of solidification of the salt.

In case of DRACS, which is composed of two natural circulation loops, we can follow the approach described by Vijayan and Austregesilo [103] and integrate Eq. 4.10 over the loop length. By imposing the circular condition on the loop ($\oint \mathrm{d}p = 0$) we obtain:

$$\frac{\mathrm{d}W}{\mathrm{d}t}\left(\oint\frac{1}{A}\mathrm{d}s\right) = g\rho\beta\oint T\mathrm{d}z - \oint(\tau_{\mathrm{w}})\frac{P}{A}\mathrm{d}s\,. \tag{4.11}$$

In a circular pipe, the frictional pressure drop per unit length can be written using the friction factor f through the Darcy-Weisbach equation as:

$$\tau_{\mathrm{w}}\frac{P}{A} = f\frac{W^2P}{2\rho A^3} = \frac{a}{8Re^b}\frac{W^2P}{\rho A^3}\,, \tag{4.12}$$

where Re is the Reynolds number (which is, again, a function of the position along the pipe), and a and b are two constants related to the flow conditions. In our model, we consider that $a = 64$ and $b = 1$ for laminar flow, and $a = 0.316$ and

$b = 0.250$ for turbulent flow. The transition from laminar to turbulent flow is assumed to take place at $Re = 2300$.

Eq. 4.12 is strictly valid for pipes with constant cross-sectional area. Where other elements are present which impose a specific pressure drop on the flow, such as a restriction, the reactor core, or the shell-side of a heat-exchanger, the value of $\tau_\mathrm{w} P/A$ is calculated in terms of the corresponding pressure drop ΔP using standard correlations (a relevant discussion follows in Section 4).

Proceeding further, and using assumptions (3), (4) and (5), the energy conservation equation for the liquid salt in each section of the piping system leads to:

$$\frac{\partial T}{\partial t} + \frac{W}{A\rho}\frac{\partial T}{\partial s} = -\frac{h(T_\mathrm{w} - T)P}{A\rho c_\mathrm{p}} \, , \tag{4.13}$$

where T_w is the temperature at the wall, h is the local wall heat transfer coefficient and c_p is the specific heat capacity of the liquid (molten) salt.

In the particular case of DRACS, which will be introduced in detail in Chapter 6, the section of the loop where the reactor vessel is present requires an additional heat-addition term to be inserted into the energy equation, which represents the heat transferred to the fluid from the reactor, or:

$$\frac{\partial T}{\partial t} + \frac{W}{A\rho}\frac{\partial T}{\partial s} = -\frac{h(T_\mathrm{w} - T)P}{A\rho c_\mathrm{p}} + \frac{\dot{Q}}{L_r A\rho c_\mathrm{p}} \, , \tag{4.14}$$

where $\dot{Q}$ is the power generated in the reactor and L_r the reactor length.

Eq. 4.5, described in the previous section, is used to find the wall temperature. When the freezing model is artificially disabled (i.e. no freezing is considered) Eq. 4.5 is replaced with the following equation:

$$\frac{\partial T_\mathrm{w}}{\partial t} = -\frac{h_\mathrm{ext}(T_\mathrm{w} - T_\mathrm{ext})P_\mathrm{ext}}{A_\mathrm{w}\rho_\mathrm{w} c_\mathrm{p_w}} - \frac{h(T_\mathrm{w} - T)P}{A_\mathrm{w}\rho_\mathrm{w} c_\mathrm{p_w}} \, , \tag{4.15}$$

we recall that the subscripts "w" and "ext" indicate, respectively, the conditions

on the inside/internal wall of the pipe (in contact with the salt) and on the out-side/external wall of the pipe. With respect to DRACS, in the molten-salt/molten-salt heat exchanger, the external side of the pipe wall corresponds to the secondary molten-salt loop, while in the case of the molten-salt/air heat exchanger, the external side of the wall is corresponds to the ambient air and, because the heat exchanger is assumed to be horizontal and flat, T_{ext} is considered a constant (see Section 6.1).

The thermohydraulic model describing the piping system in DRACS comprises therefore of Eqs. 4.11 – 4.15 for the primary loop; Eqs. 4.11 – 4.13, and 4.15 for the secondary loop, with Eqs. 4.1 – 4.6 governing the freezing process in the molten-salt/air heat exchanger. The model is completed by providing expressions for the various heat transfer coefficients h, ambient air temperature T_{ext}, and geometric variables A, P and r, as functions of the position in the loops and the mass of the solidified salt (only for the molten-salt/air heat exchanger). The expression for these quantities for DRACS will be given in Chapter 6 along with an detailed description.

The aforementioned system of equations can be solved using standard numerical schemes. In our case it was solved in MATLAB using a first-order upwind explicit scheme (FTUS). The approach is briefly summarised here to provide an example of such methodology. First, the pressure drops are calculated, then the flow-rates in each of the loops are computed based on the buoyancy caused by the spatial temperature distributions; the heat transfer coefficients are then calculated and, finally, the temperature distribution is solved in each loop to find the temperature at the next step. When freezing occurs, an additional step is added to calculate the mass of solidified salt. The mesh resolution used in the various simulations was such that the steady-state temperature error deriving from using a twice-finer mesh was less than 1%. It is important to mention that solving the advection equation in a piping system which include a natural convection loop, such DRACS, is problematic. Indeed, depending on the discretisation scheme used and the mesh

resolution, numerical diffusion can help in stabilising the system, as demonstrated in publications by Ambrosini and co-workers (see, for example, Ref. [104]). Of course, in a real system, diffusion is present in terms of axial heat diffusion along the fluid and the pipe walls so that some numerical diffusion appears beneficial for a realistic simulation. However, numerical diffusion does not match actual processes, and simulated oscillatory behaviour of the loop can be dampened or magnified with respect to the real system depending on the scheme/mesh resolution used (see in this respect the study of Mangal et al. [105]). Choosing the right mesh/scheme is therefore difficult but important in the study of the oscillatory behaviour of natural convection loops. Nevertheless, because the studied DRACS design is unconditionally stable and we are not interested in stability analysis, we chose to adopt the FTUS scheme which is straightforward and relatively accurate. It is still worth noting though that, where oscillations are particularly strong, such as in the very early stage of DRACS transients, the simulations can be in error.

4.5   Checking the Consistency of the Combined Model

The overall approach described in the previous sections should be compared with experimental results; such comparison is the topic of this section. Specifically, the various assumptions made during the development of the freezing model in the present work (Eqs. 4.1 – 4.6) require experimental validation due to the complexity of the physical processes involved. Unfortunately, a complete experiment of freezing in a complex piping system, such as in a natural convection loop, is not available for comparison with the model predictions. We therefore validated the model through comparisons with two targeted experimental studies which can reproduce some of the physical processes taking place in more complex systems. We should however mention that the conditions of these experiments, as well as other ones which can be found in the literature, can be significantly different from the conditions encountered in molten salt applications. Therefore, even with the

following experimental validation, the application of this model to simulate molten salt freezing is not straightforward. More information in this regard will be given in Chapter 5.

4.5.1   Transient freezing: Test case (1)

The first test case used for validating the model for transient salt freezing is the experimental study of McDonald and co-workers [106]. This experiment involved monitoring the freezing time of a pipe section full of water as a function of the thermal conditions on the pipe surface. In particular, a 5.08 cm Schedule 80 pipe full of water was subjected to natural and forced convection with an outside air temperature spanning the range from -6 °C to -26 °C. The temperature of the water was measured at the centreline of the pipe using a thermocouple. The total freezing and cooling time was calculated by measuring the time required to drop the temperature to and below the freezing point, when solid cooling occurs.

The experiment was simulated by considering a 4.93 cm ID pipe (corresponding to a 5.08 cm, Schedule 80 pipe) full of quiescent water at approximately 21 °C (the stated initial temperature in the experiments). The value of the heat transfer coefficient on the outside surface of the pipe was taken as being equal to the reported values in the experimental study for both natural and forced convection. The thermophysical properties of the pipe material (steel) and ice were evaluated at 0 °C. The liquid-side heat transfer coefficient was calculated by assuming $Nu = 3.66$, which is the limiting solution for a laminar pipe flow and a constant pipe wall temperature.

The comparison between the results of the model and the experiments is shown in Fig. 4.5 and Fig. 4.6. The error bars in the figures indicate the range of results obtained by changing the thermophysical properties of water, air and ice over a reasonable temperature range ($\pm$ 15 °C). A good agreement can be seen between the model and the experimental data, even if the results for the forced convection

Figure 4.5: Comparison between the total freezing time measured by McDonald et al. [106] (circled dots) and the simulated freezing time (bars) for a 5.08 cm Schedule 80 pipe full of water under forced convection.

case are underestimated for air temperature values approaching zero. Considering the simplicity of the current approach and the possible experimental errors, the results are deemed satisfactory.

4.5.2 Transient freezing: Test case (2)

In order to validate our model of transient salt freezing when significant flow of fluid is present, data from a second experimental study, that of Cheung and Baker [107], were used. This experiment was intended to measure the penetration length into a pipe reached by a liquid phase before complete freezing occurred. The experimental setup used in this study is shown in Fig. 4.7 and consists of a coiled tube fully immersed in liquid nitrogen. During an experiment, water is injected into the initially dry tube through the fast opening of a valve. The flow velocities of the water inside the tube was varied by using different water pressures. The authors measured the penetration length by weighing the amount of water present in the tube after the experiment and related it to different parameters such as the
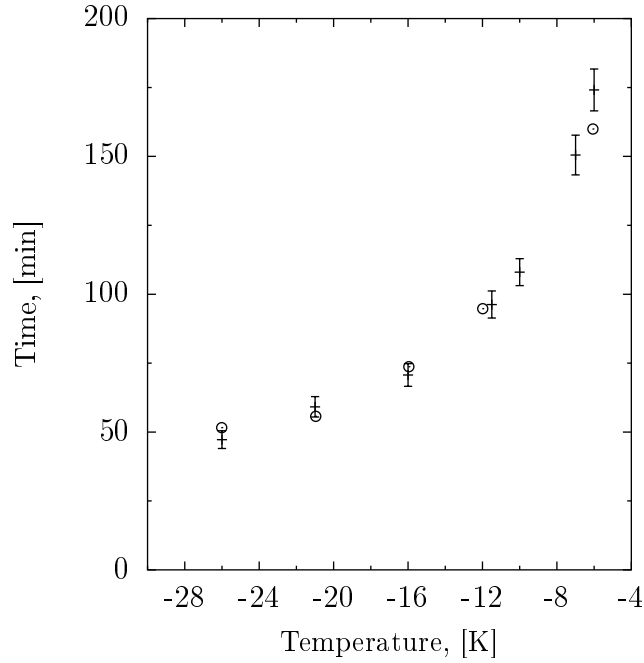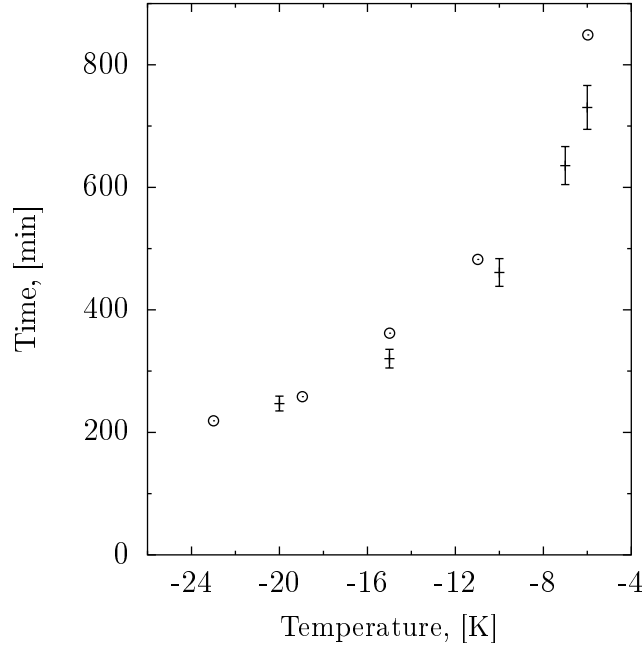
Figure 4.6: Comparison between the total freezing time measured by McDonald et al. [106] (circled dots) and the simulated freezing time (bars) for a 5.08 cm Schedule 80 pipe full of water under natural convection.

initial temperature of water (ranging from 0 °C to 90 °C) and the average flow velocity inside the tube (ranging from 0.6 m/s to 1.4 m/s). The diameters of the pipe used in the experiment were 0.476 cm and 0.794 cm.

To simulate the experiment we adapted our model by considering a tube partially immersed in liquid nitrogen, with a fixed wall temperature (-196 °C). This assumption is justified by the very high heat transfer coefficient between the pipe and the boiling liquid nitrogen on the outside of the pipe. At $t = 0$ the non-immersed part of the tube is considered full of water with an initial velocity V_0 and the immersed part of the tube is considered empty. A constant pressure is imposed on the fluid. The average velocity of the water during an experiment is therefore a function of both the initial fluid velocity and the imposed pressure. The current approach is motivated by the lack of information about the experimental setup upstream of the coiled tube. The simulation ends when a section of the cryogenic pipe becomes clogged. The penetration length is computed by calculating the amount of water which flowed in the cryogenic pipe over the total simulation time.
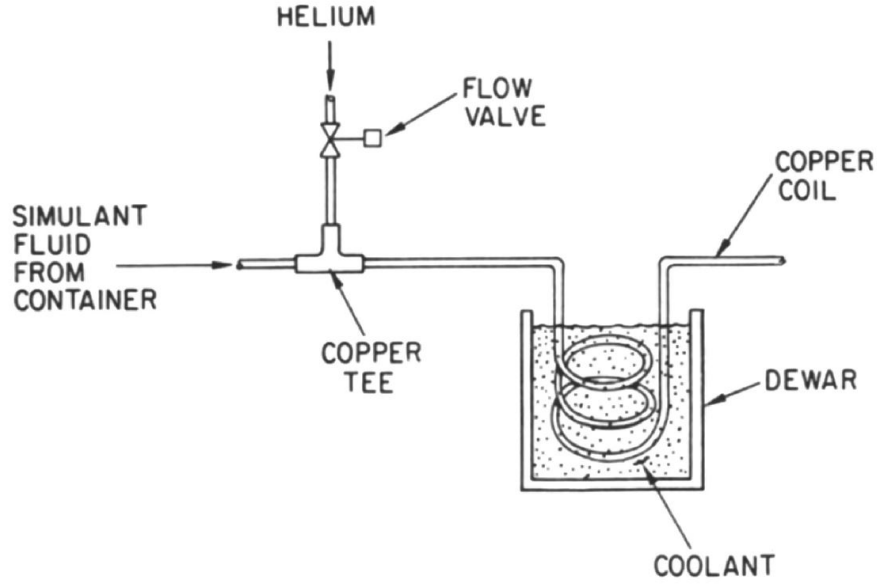
Figure 4.7: Experimental setup used by Cheung and Baker to study the transient freezing of water [107].

The thermophysical properties of ice were calculated at -98 °C, which is an average between the freezing temperature of water and the boiling temperature of liquid nitrogen. The liquid-side heat transfer coefficient is calculated using the Sieder-Tate correlation for turbulent flow (which is the flow condition for the range of observed Re), which takes into account the variation between the bulk viscosity μ and the viscosity at the wall μ_{w}:

$$Nu = 0.027 Re^{0.8} Pr^{0.3} \left(\frac{\mu}{\mu_{\mathrm{w}}}\right)^{0.14}. \tag{4.16}$$

The comparison between the results of the model and the experimental data is shown in Fig. 4.8. The error bars correspond to the results obtained by conducting a sensitivity analysis on the major uncertainties of the model. Specifically, we checked for the robustness of the model by varying within a reasonable range: (1) the thermophysical properties in the model; and (2) the initial velocity and pressure of the water. The last point is particularly important as the values of these two quantities are assumed, to an extent, arbitrarily and there are multiple combinations of the two which results in the same average flow velocity (reported
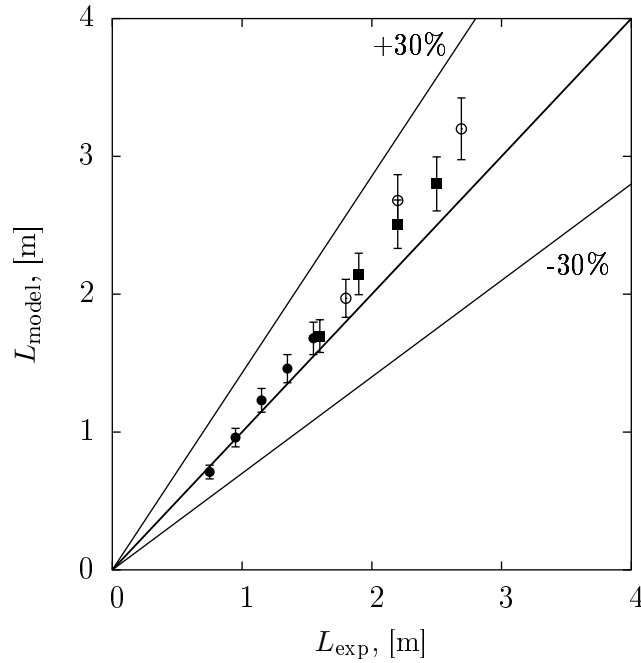
Figure 4.8: Comparison between the penetration length measured by Cheung and Baker [107] (L_{exp}) and the penetration length simulated by the model (L_{model}). The squares refer to an average velocity of 0.6 m/s in a 0.794 cm ID pipe. The opened and closed circles refer respectively to an average velocity of 0.6 m/s and 1.45 m/s in a 0.476 cm ID pipe. The results for each set are obtained by using different liquid initial temperatures (0-80 °C).

in the experiments).

Referring to Fig. 4.8, the model predictions are well within ±30% deviations from the corresponding experimental data, with an average deviation less than half of this value. Considering the relative simplicity of the model and the fast dynamics of the physical process involved, this is considered a satisfactory agreement. Some of the simulations do show a degree of overestimation of the experimental results, which is found to increase at higher initial liquid (water) temperatures. This behaviour may be partially ascribed to an overprediction of the heat transfer coefficient in the current approach using the Sieder-Tate equation, which results in heat fluxes of the order of $\sim 10^4$ W/m^2 when the liquid was almost all frozen.

4.6 Conclusions Chapter 4

In this Chapter we developed an analytical model to simulate transient freezing of molten salts in piping systems. The biggest assumption in the model was to assume steady-state temperature profile in the ice layer, which will worsen the predictions for thick ice layers. A study over the disagreement with standard theory, however, showed that the error is not significant when compared to other sources of error, such as the uncertainties regarding the value of the thermal conductivity of the liquid phase. The model was developed with the purpose to be incorporated in standard thermo-hydraulic codes, such as the one describing the behaviour of DRACS, also derived in this Chapter. The combined model (transient freezing + thermo-hydraulic model of the piping system) was successfully validated against two transient experiments found in the literature.

Chapter 5

Transient Freezing: Experiments

Previous experimental work on freezing in internal flow revolved around the study of water solidification. A literature review describing the most relevant studies has been conducted in Section 4.2. Usually the coolant was a mixture of water and a low-boiling point organic fluid, such as an alcohol. The temperatures reached by the wall-side of the flow were therefore between 10-40 °C less than the bulk temperature of the water freezing. In a molten salt unit, however, this difference in temperature can be considerably higher. For example, in DRACS, the molten salt/air heat exchanger is exposed by the tube-side to the hot molten salt at around 500 °C and from the wall-side to ambient air at 60°C. This much higher temperature difference has the effect of increasing the importance of the heat transfer through the ice layer and of the wall heat capacity on the overall freezing process. Therefore, previous studies might not capture appropriately the physical processes taking place under these conditions. In this Chapter we describe the experimental study of a channel flow of water freezing in contact with a cold plate cooled by a liquid nitrogen flow. The aims of such experiments, whose apparatus and techniques are described in Sections 5.1, 5.2, and 5.3, are to: (1) validate the code described in Chapter 4 under the specific conditions of high temperature difference between the hot and cold fluids. A comparison between the experiment

and the model is given in Section 5.4; (2) further characterise transient freezing in the mentioned conditions. A description of the experimental results is given in Section 5.4.

5.1 Experimental setup

The experimental setup consists of a recirculating flow facility which is capable of pumping water under different conditions inside a test section, where the actual measurements are conducted through the use of laser-based diagnostic techniques. Specifically, the experiment consists of measuring the thickness of a solidified layer of water during its constant growth. Freezing is accomplished by placing a cold surface in contact with a laminar channel flow of water. The current set-up and methodology took inspiration from the work of Savino and co-workers [98] and the difficulties reported by the authors.

5.1.1 Flow facility

A schematic of the flow facility showing its main components is given in Figs. 5.1 and 5.3a. Tap water from the mains is used as the test fluid and is stored in a 25l tank which serves as a reservoir. Glass hollow spheres (LaVision, 11.7 μm mean diameter) and a dye (Sigma-Aldrich, Rhodamine B) are added at low concentration (<1 g/L) to the water in order to conduct the measurements. The presence of these additives was found in previous studies [108] to not modify appreciably the density and viscosity of the fluid. The independence of the freezing point of the solution on the additives was experimentally confirmed. The water is pumped from the tank through the circuit using a standard centrifugal pump. The water flow-rate is controlled by a ball valve and measured via a rotameter placed downstream of the test section. The rotameter was installed in this position in order to reduce the amount of air bubbles flowing through the test section during the
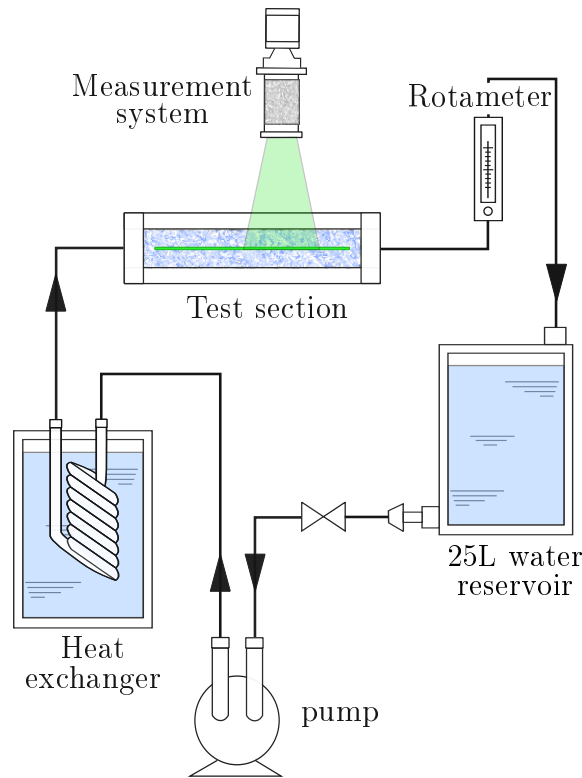
Figure 5.1: Schematic of the flow circuit used in the experiments.

experiments. It was indeed found that the rotameter entrained tiny air bubbles which would get released during the pump start-up or even by changing the flow-rate. The readings of the rotameter were manually checked. A heat exchanger is used to control the water temperature which was measured at the entrance of the test section using a K-type thermocouple. The heat exchanger was produced in-house using copper piping and standard fittings.

5.1.2   Test section

The test section, whose details are offered in Figs. 5.2 and 5.3b, was specifically designed to allow for studying solidification under high heat flux which can be present in operational units utilising high melting-temperature salts. It comprises a 6 mm thick, 30 cm long Perspex channel cut out on one side to allow for the placement of a 1 mm thick, 20 mm long copper plate which serves as a cold surface for the solidification of the water. The dimensions of the channel were chosen
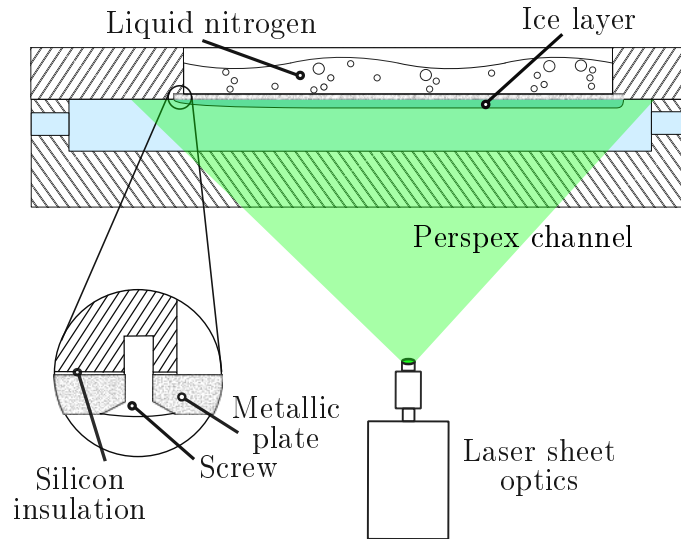
Figure 5.2: Schematic of the test section used in the experiments.

so that the fluid flow and the heat transfer through the solidified layer were 2-dimensional where the measurements were taken. Heat removal is accomplished by placing the other surface of the plate in contact with boiling liquid nitrogen (-197 C). The dimension of the copper plate is smaller than the channel so that the plate does not touch its side-walls. This arrangement was decided in order to avoid higher solidification rates along the side walls where the velocity and therefore the heat transfer coefficient is less. A thicker ice-layer close to the wall would obstruct the field of view of the camera making measurements impossible. Liquid nitrogen is poured directly in the cavity formed by the plate and the thick Perspex channel (see Fig. 5.2). Water is injected in the channel through three access points in order to reduce bubble formation and large-scale turbulence. Steel meshes are present at the entrance and exit of the channel to further reduce large-scale turbulence and achieve the appropriate flow condition. The main feature of the channel is that it can be tilted up to 210°. The main reason behind this arrangement is to clear the channel from air bubbles which are inevitably present at the start and accumulate during the experiment. A camera, part of the measurement system, is placed on the same frame as the channel and it is tilted with it so to decrease measurement errors after the calibration is carried out (see next section).

<table>
<tr><td>(a)</td><td>(b)</td></tr>
</table>
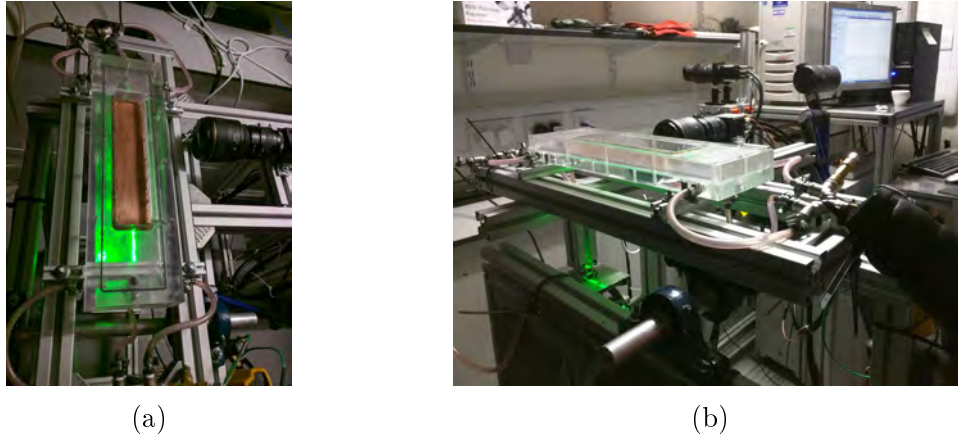
Figure 5.3: Picture of: a) flow facility, b) test section.

5.1.3   Diagnostic techniques

Particle image velocimetry (PIV) and laser induced fluorescence (PLIF) were utilised to measure the thickness of the solidified layer of water. These techniques were employed to overcome some important problems identified in the literature and early stage experimental trials, in which temperature-driven light distortions made it difficult to locate the interface precisely [98]. PIV was also used to measure the velocity field, whose knowledge proved very important to process the data and to allow for a proper comparison between the simulations and the experiments. PIV and PLIF are hereby briefly summarised. More details can be found in Ref. [108]. The glass particles and the dye are illuminated with a laser sheet and reflect light to the camera. With PLIF the light fluoresced by the dye present in the fluid is detected and the fluid therefore appears as uniformly coloured with respect to the solid parts. PIV takes measurements of velocity fields by taking two images in short sequence. The glass particles added to the fluid appear as bright spots and it is possible to calculate the distance that each particle covered by comparing the two images. The velocity is then found by knowledge of the time gap between the two images.

5.2   Procedure

The following procedure was conducted for each set of measurements. First, the diagnostic techniques were calibrated by using a specific target placed inside the test section facing the camera. Then the target was carefully removed, paying particular attention to vibrations which could change the position of the camera relative to the test section. The test section was then closed and the flow initiated through the pump. The test section was then tilted up to 90° into a vertical position. Almost all the air bubbles stuck in the test section would then be removed leaving a clear view for the camera. The heat exchanger was then turned on to provide heat or cooling power to the circuit, and then the whole setup was left to stabilise until the temperature and the flow-rate reached the desired values. The temperature was maintained within ±0.2 °C for all the duration of the experiment. The laser was then fired and the recording started which lasted for up to 3 minutes. Soon after the laser was initiated, liquid nitrogen was poured on top of the copper plate and continuously added thereafter for all the duration of the experiment.

The measurements were taken towards the end of the copper plate where the layer thickness achieved an uniform profile. Indeed towards the start of the copper plate, where the thermal boundary layer is not fully developed, the layer is progressively thinner. Particular care was taken to avoid water moisture to flow in front of the camera and the laser apparatus. This water moisture was produced by the drop in temperature caused by the cold boiling liquid nitrogen.

5.3   Data processing

Acquired data were reduced to compute the thickness of the layer versus time as well as all the other important quantities needed for an accurate comparison of the experiments with the model. By far the most difficult task was to track the solid/liquid interface. This was initially achieved by taking the signal refracted
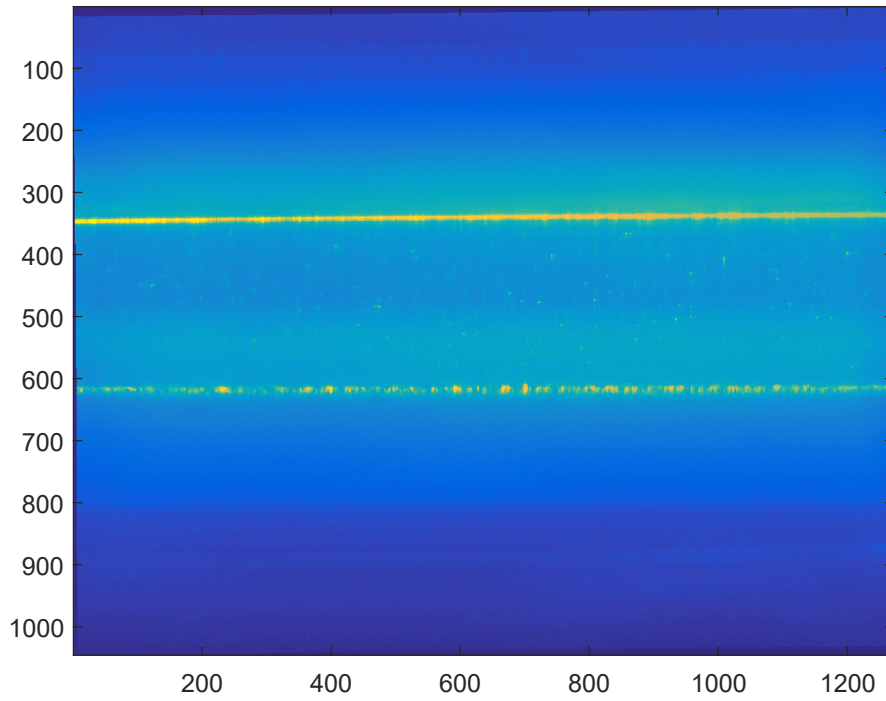
Figure 5.4: Filtered image of the channel as recorded by the digital camera. The bottom and top interface are clearly visible.

from the interface and scattered by the glass particles stuck at the solid/liquid interface (see Fig. 5.4).

We reference to this method as Method 1 because, as explained in the next lines, not all the data were processed in this way. The scattered signal from the interface was clear when flow velocity and temperatures were relatively low and allowed to spot the interface accurately. However, at higher temperatures and flow velocities, the position of the interface was more difficult to locate and impossible in certain cases. To locate the interface under these conditions we used the flow velocity data acquired through PIV (Method 2). The flow was indeed 2-Dimensional as expected from theory and the velocity profile was very clear and in many cases perfectly parabolic. The velocity profile was then extrapolated to find the interface (velocity equals zero). Fig. 5.5 offers a comparison between the two methods. As shown by the figure, the results of the two methods are very similar (within the experimental error). In this way it is possible to find the interface even for those conditions where Method 1 does perform well. Also, by positively comparing
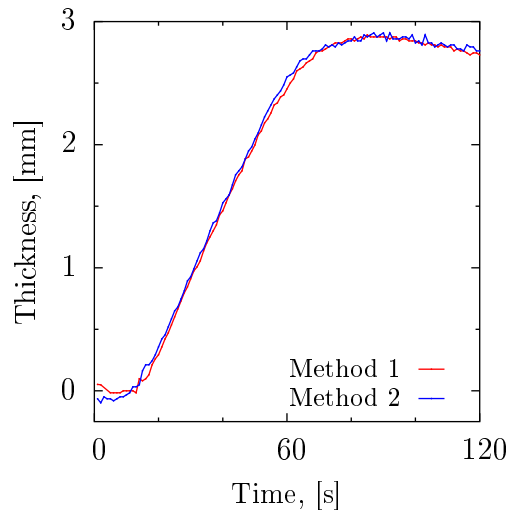
Figure 5.5: Thickness of the solidified layer of fluid versus time computed using two different methods: (1) scattered signal from the interface; (2) extrapolation of the 2D velocity profile to the wall. The two methods performed similarly suggesting that the approach was reliable.

the methods we were able to cross-check the validity of the present approach. It is worth mentioning that the velocity-based interface measurement (Method 2) became very noisy when the velocity was low, due to the lower accuracy of PIV. Fortunately, at low flow velocities, the first method was very accurate and velocity data were not needed.

It can be beneficial to briefly discuss the problem of interface location in light of the present findings. As mentioned in previous literature locating the interface can be difficult and simple approaches do not perform well [98]. This problem arises mainly from the light distortions caused in proximity of the interface by regions of cold and hot fluids which possess different refractive indices. During our first trials we noticed that it was very difficult, if not impossible, to do this accurately by using standard techniques (like shade-ography). This conclusion was reached by Savino et al. which ultimately measured the interface position by adopting a cathetometer and by a temperature-probe method (see [98] for details). Given the accuracy of the results offered in Fig.5.5 and the disadvantages of the previous methods, we think that our approach offers a reliable answer to the problem of interface location and should be used when possible.

PIV data were also used independently to acquire the velocity profile. Knowledge of the velocity profile was important to check for the validity of the 2-dimensional flow assumption used in the model. Also, because the thickness of the channel decreases while the ice-layer is growing, velocity data are invaluable to know precisely the local Reynolds number in the flow, which varies as a function of time.

5.4 Results and discussion

5.4.1 Experimental data

From the experimental setup and methods described before we could acquire, as a function of time, the thickness of the solidified layer and the local Reynolds number; this for different flow-rates of water and inlet temperatures. Fig. 5.6 reports the thickness of the solidified layer versus time for different experimental conditions. Water does not start solidifying as soon as liquid nitrogen is poured in the cavity; the solidification is delayed and happens later. This is shown in the picture by an initial "buffer" period where the thickness of the ice layer is zero even if liquid nitrogen has been poured in the cavity. The extension of this buffer period depends on the inlet conditions of the water flow, increasing with the inlet temperature and the water flow-rate. The presence of this buffer period can be easily explained: it is related to the time needed to cool the copper plate below the melting temperature of water. Once the temperature of the copper plate is below the melting temperature of water, the water in contact with the plate is sub-cooled and solidification starts. The newly formed layer of ice grows steadily until cooling power is ceased. The thickness of the ice layer grows almost linearly with time and ends abruptly towards the end of the experiment when no more liquid nitrogen is present in the cavity.

Curves similar to Fig. 5.6 were observed for all the experimental conditions used
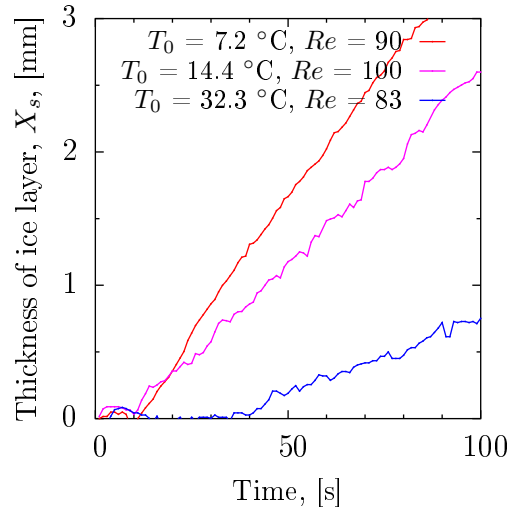
Figure 5.6: Measured thickness versus time for different conditions. This was found to increase approximately linearly with time.

in the study. The linearity of such curves is somewhat counter-intuitive as one would expect that the thicker the ice-layer is, the higher is the resistance to the heat transfer, and thus, the slower the growth. The linearity of the curves is however easily explained when we take into account the thermal mass of the plate. Indeed the copper plate is subjected to continuous cooling throughout the experiment and its temperature continuously decreases, similarly to what happens in the buffer period. The effect of steady temperature drop of the copper plate is to increase the temperature difference between the plate and the water, which compensate for the larger resistance to heat transfer offered by the growing ice layer. These two opposite effects balance each other leading to an almost linear growth rate of the ice layer.

Thanks to their linearity, each curve can be characterized by a growing rate, which is its slope. Fig. 5.7 reports these growth rates of the ice layer as a function of the inlet water condition, namely its temperature and flow-rate.
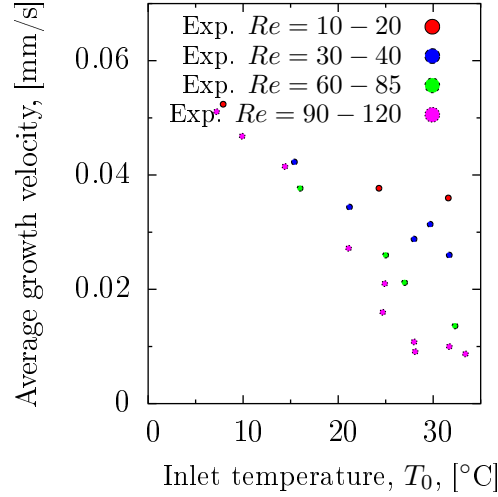
Figure 5.7: Measured average growth rate of the ice layer versus inlet temperature T_0 for different values of Re.

5.4.2   Simulations

The freezing model described in Chapter 4 was applied to simulate the experimental conditions described in the previous section and the results of the simulations were compared with the experiments. The simulated 1-dimensional case consists of a 20 cm long channel, divided along its length in increments of length $ds = 1$ mm. The system of equations described in the previous Chapter were solved for each space increment using the FTUS scheme (first order upwind explicit) to find the lumped fluid temperature T, plate wall temperature T_w and thickness of the solid layer X_s, proportional to the mass of fluid solidified per unit length m_s. With respect to the boundary conditions, the bottom surface of the channel was considered adiabatic while the top surface, representing the 1 mm copper plate, was assumed in contact with boiling liquid nitrogen (T_{ext} = -196 C°). The heat transfer coefficient between the plate and boiling liquid nitrogen h_{ext}, given in W/m^{2}K, was taken from Ref. [109]:

$$h_{ext} = 125 + 0.079\,(T_w - T_{ext}). \qquad (5.1)$$

Because the simulations were found to be sensitive to the value of h_{ext}, we posi-

tively double-checked for its accuracy by measuring the volume of liquid nitrogen evaporated per unit of time across the duration of the experiment and derived an average heat transfer coefficient through an energy balance. We conducted this operation twice and the calculated heat transfer coefficient was within 20% of the one predicted by Eq. 5.1

A brief discussion is needed on the time at which the liquid nitrogen flow in the cavity is stopped. In the experiment this is not a specific time but rather a window when the plate is not fully covered with liquid nitrogen. In the model we cannot simulate this condition, instead we interrupted the flow of liquid nitrogen by imposing $h_{\text{ext}} = 0$ at the average time between when the plate was starting to be uncovered by the liquid nitrogen and when it was completely uncovered.

The fluid, initially at a constant temperature T_0, was assumed to have a constant Re which was taken equal to the average Re measured in the experiments. The inlet temperature of the fluid was also taken to be T_0. The expression for the thermal properties of ice, water, and copper were taken from Ref. [110]. The thermal properties were calculated at each iteration based on the mean temperature of the material. Specifically for water, whose properties vary significantly with temperature, they were evaluated at the average temperature between the bulk temperature and the melting temperature.

The value of the water/ice heat transfer coefficient h was taken from the correlations for laminar flow in non-circular pipes [111], using a Nusselt number Nu of 8.2 when no ice layer is formed (constant heat flux boundary condition) and $Nu = 7.5$ when ice is formed (constant temperature boundary condition). Further studies revealed that the heat transfer coefficient measured using the mentioned correlations was over-predicted by up to 50% in some cases. The value of h was indeed calculated for few studies by measuring the bulk fluid temperature drop along the channel and by conducting an energy balance. A brief discussion on the causes of this over-prediction is carried out in the end of Section 5.4.3.

5.4.3   Comparison

A comparison between the model and the experimental results is offered in Figs. 5.8–5.11 and hereby discussed. Fig. 5.12 also reports the predicted growing velocities of the ice layer along with the ones experimentally measured. As mentioned before, the values of these velocities were found by linear interpolation of both the experimental and simulated profile. Because a slight departure from linearity is always present, these values are considered as an "average" growth velocity. Overall good agreement was found between the model and the experimental results, indicating the applicability of the present approach.

The main sources of error between the experiments and the model are discussed in the following lines and are: (1) low initial, wall side heat transfer coefficient, (2) partial interruption of liquid nitrogen flow, and (3) lower ice/water heat transfer coefficient. By far the most prominent source of error was (1), whose effect are offered in Fig. 5.13 which reports the typical result, here for a fluid of initial temperature $T_0 = 16$ °C and an average $Re = 94$.

In Fig. 5.13 two simulations are shown along the experimental data named "corrected" and "uncorrected" simulations. The difference between the lines referring to the two types of simulations is a shift along the axis. The uncorrected simulations are the results simulated by the model as described before. The predictions of the model seem accurate with respect to reproducing the overall behaviour of the system, however it seems that the formation of ice starts before the experimental results. It appears clear that there is a physical behaviour of the system which the simplified model described previously is not able to capture. If the results of the model are artificially "shifted" so that the formation of ice takes place at the same time of the experiments, then the profile is predicted with good accuracy.

To understand the shift between the experimental results and the model we plotted such shift in Fig. 5.14 as a function of the inlet temperature T_0. The Re was

Figure 5.8: Experimental results and simulations for an inlet fluid temperature $T_0 = 8\,°C$ and an average $Re = 20$: a) channel thickness versus time. b) local axial velocity component as a function of the dimensionless position along the channel of width d_0.
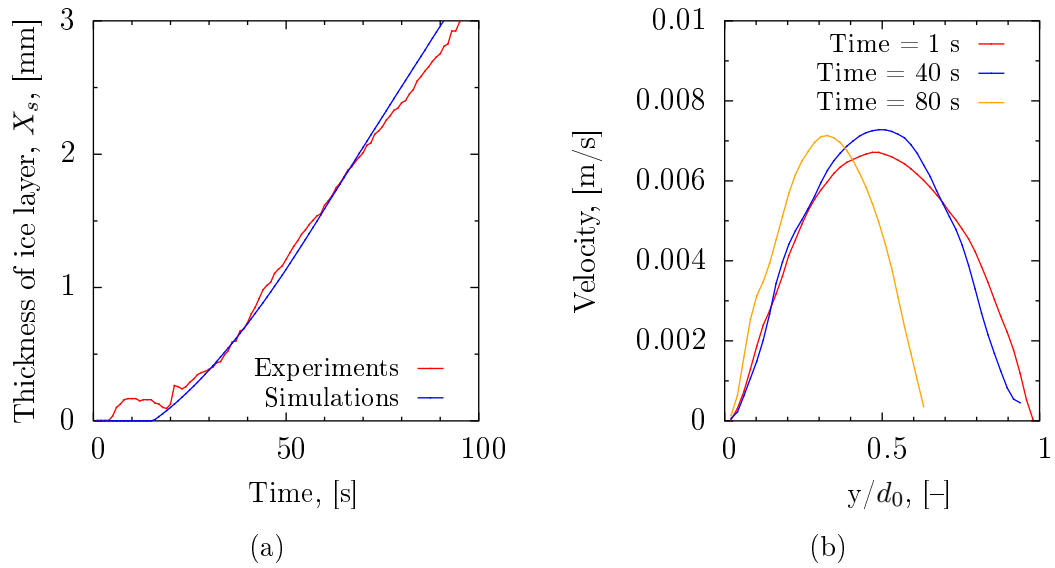
Figure 5.9: Experimental results and simulations for an inlet fluid temperature $T_0 = 24\,°C$ and an average $Re = 20$: a) channel thickness versus time. b) local axial velocity component as a function of the dimensionless position along the channel of width d_0.

(a)

(b)
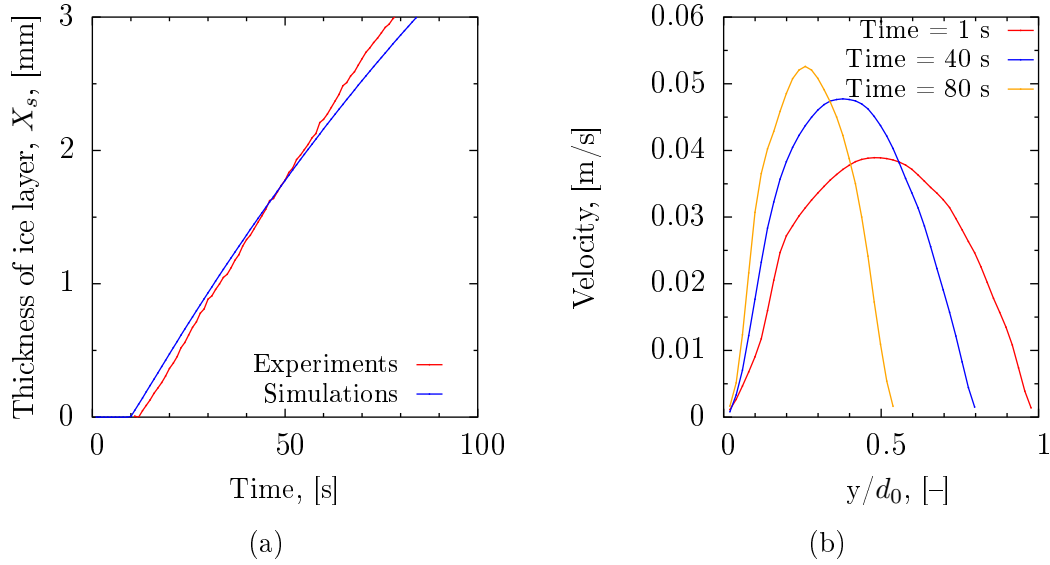
Figure 5.10: Experimental results and simulations for an inlet fluid temperature $T_0 = 10$ °C and an average $Re = 100$: a) channel thickness versus time. b) local axial velocity component as a function of the dimensionless position along the channel of width d_0.

(a)

(b)

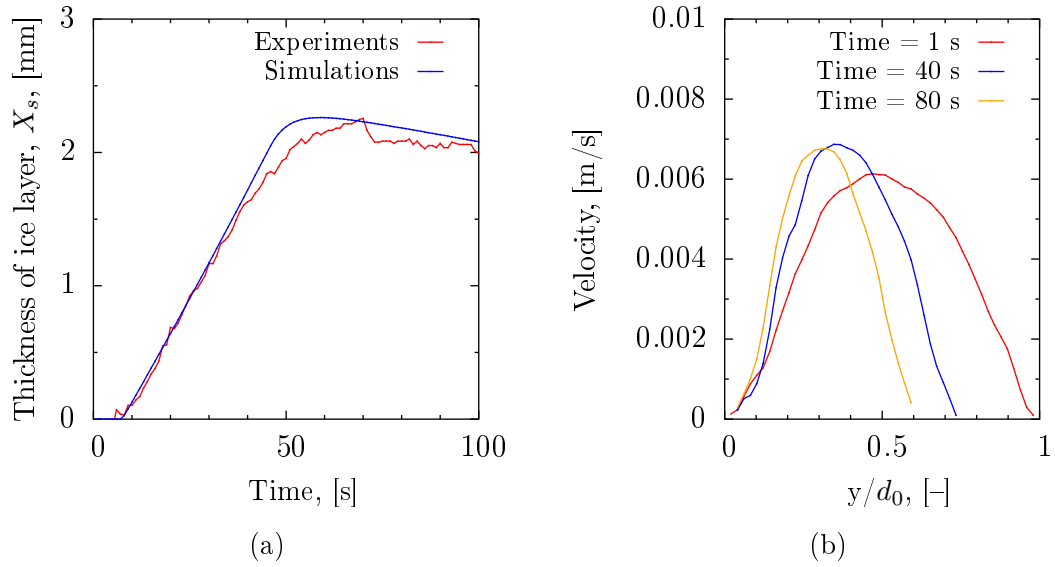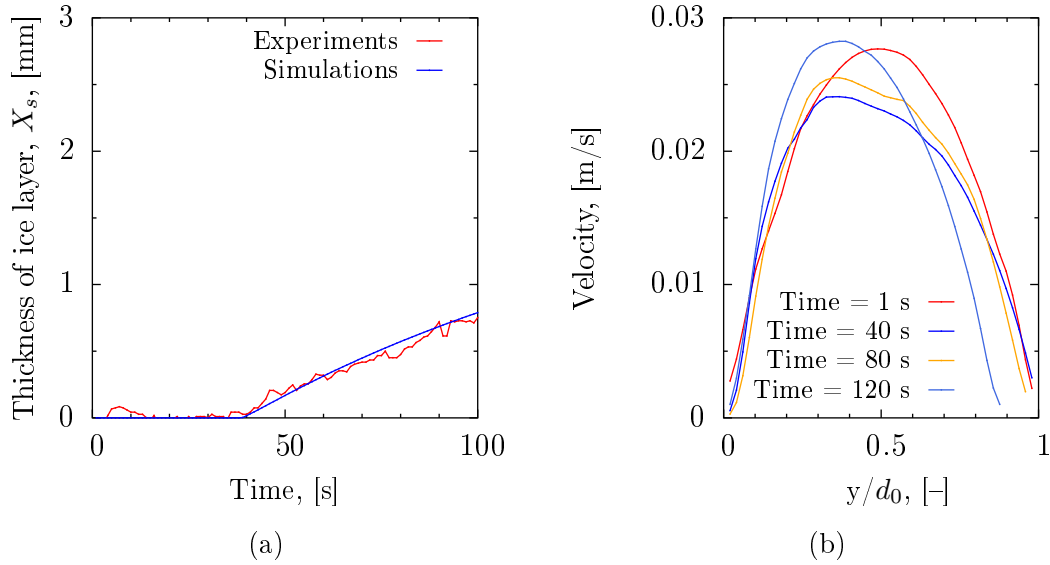Figure 5.11: Experimental results and simulations for an inlet fluid temperature $T_0 = 32.3$ °C and an average $Re = 94$: a) channel thickness versus time. b) local axial velocity component as a function of the dimensionless position along the channel of width d_0.
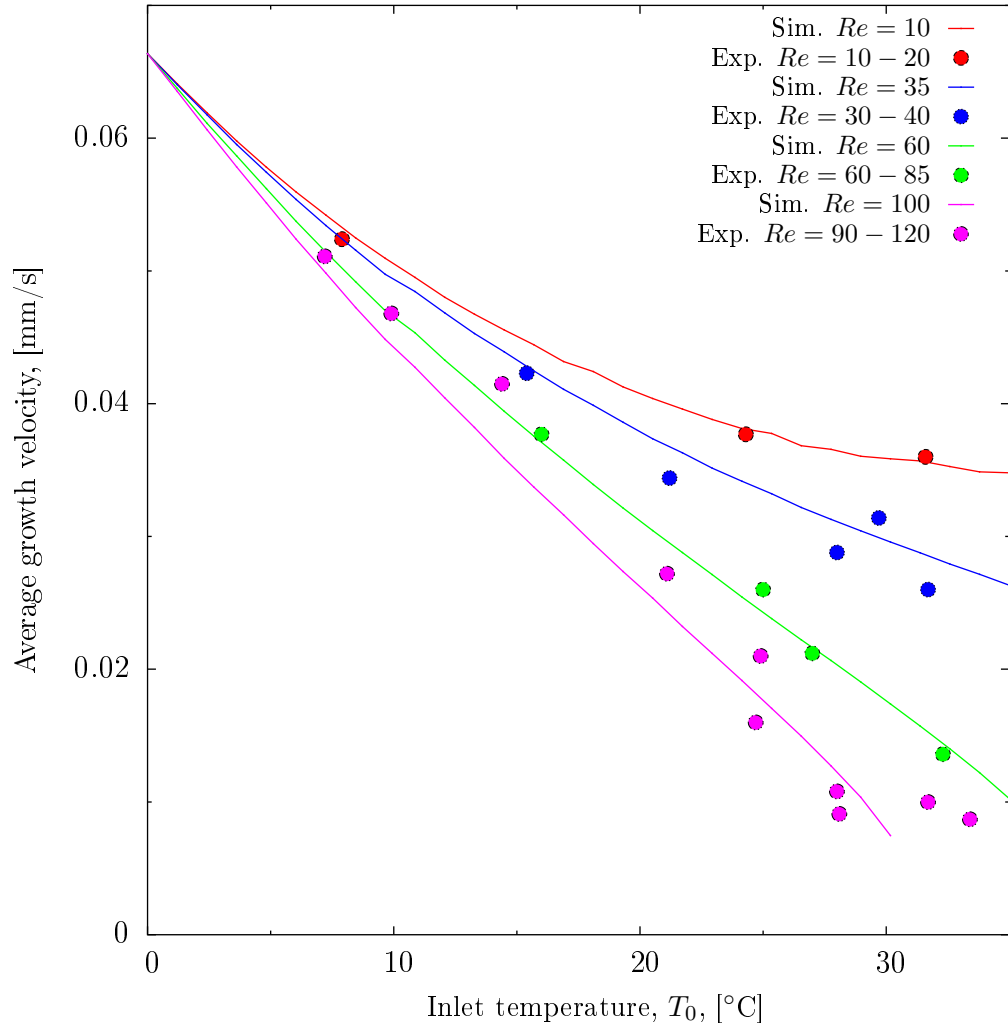
Figure 5.12: Measured and simulated average growth rate of the ice layer versus inlet temperature T_0 for different values of Re.
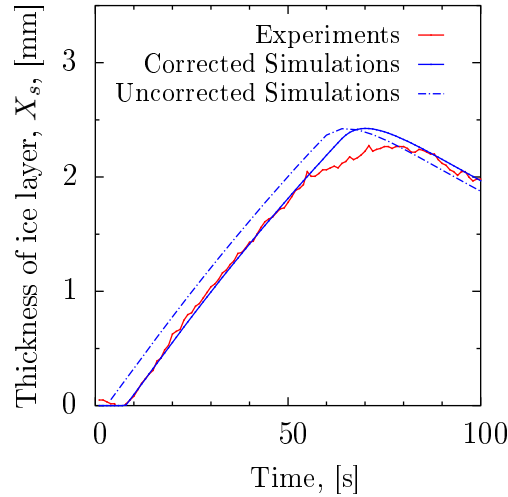
Figure 5.13: Measured and simulated channel thickness versus time. Inlet fluid temperature T_0 and average Re are respectively 16 °C and 94.

found to not affect significantly the starting time of ice formation neither in the experiments nor in the simulations for the inlet temperatures considered ($T_0 < 35$ °C). As shown by the figure, the shift is fairly constant and amounts to approximately 7 s. The reasons for this shift can be multiple and, as for now, it is not well understood. One possible reason is that the heat transfer coefficient between the plate and boiling liquid nitrogen is initially very low. It is indeed known that liquid nitrogen, once placed in contact with a warm surface, develops a layer of vapour which temporarily insulate it from the material.

One cause of the additional shift between the model and the experimental results at higher temperature is also explained by considering the thermal transient in the channel before the formation of the ice layer, which the model is not able to capture properly. In the model ice is formed when the temperature of the wall drops below the freezing point and thus the time required to develop the first ice crystal is the time to cool down the wall from its initial temperature down to the freezing temperature of water. Because the model is 1-dimensional and uses a lumped water temperature, the overall heat per unit length required to drop the wall temperature is simply $A_\mathrm{w}\rho_\mathrm{w}c_{\mathrm{p_w}}(T_0 - T_\mathrm{melt})$, which in the present case of thin wall is relatively small. In reality, the layer of fluid in contact with the
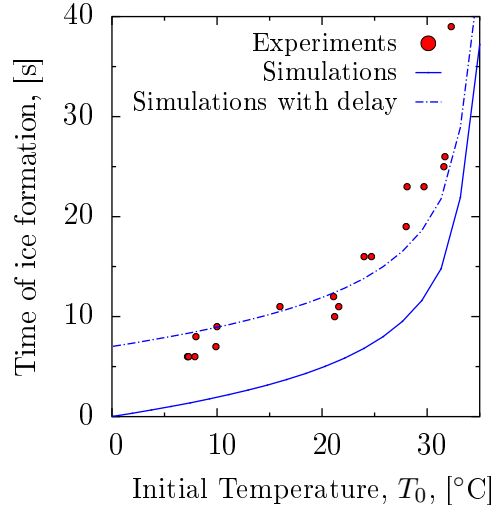
Figure 5.14: Measured and simulated start time of ice formation as a function of the initial temperature T_0 (equal to the inlet fluid temperature). The dashed line corresponds to the continuous line shifted by 7 s. The Re of the flows considered ranged from 20 to 100.

wall needs also to be cooled down. The thickness of the layer of fluid affecting this transient process can be estimated by considering the timescale of the wall temperature drop, τ, which is of the order of 3 s. This timescale is less than the timescale of the convection process in the channel $\sim L/\overline{V}$, where L is the plate length ($\sim$25 cm) and $\overline{V}$ is the average velocity ($\sim$0.02 m/s), which means that the drop in wall temperature affects significantly the temperature profile in the water over the initial transient. The thickness of the fluid layer can be roughly estimated by $\sqrt{\alpha\tau}$, where α is the thermal diffusivity of water, and it is approximately 1 mm. This length scale is comparable with the thickness of the wall, indicating that the initial process of wall temperature drop cannot by described accurately by the present approach.

Another source of disagreement between the theory and the model is found when the flow of liquid nitrogen is interrupted. At this moment the simulated layer of ice is thicker than the one measured (see figure 5.13). This disagreement is a direct consequence of the simplified assumption made before regarding the interruption of the liquid nitrogen flow.

The last source of error between the simulations and the experiments is due to

the higher value of the heat transfer coefficients predicted by the used correlations with respect to ones found in the experiments. Even if the predictions of the model were in fair agreement with the simulations with respect to the growth of the ice-layer, the agreement over the measured fluid temperature along the channel and the thickness of the ice layer during remelting was dubious. The cause for the apparent good agreement between the simulations and the experiments during the growing phase of the ice layer was that the process is governed mainly by the wall temperature, and not by the fluid side, during this initial stage. The reason for the lower heat transfer coefficient compared to the literature was identified in the temperature gradient in the liquid, which caused the viscosity to change significantly along channel section. This effect was much more pronounced in our experiment than in the literature because only one side of the channel is cooled and therefore the velocity profile is severely skewed towards the warmer side of the channel. Fig. 5.15 shows the local velocity measurements for a fluid with an inlet temperature $T_0 = 32.3$ C° and an average $Re = 80$. The departure from a pure parabolic profile, shown in the same figure, is significant and decrease the heat transfer coefficient considerably. The effect of the use of a higher heat transfer coefficient are shown in the next section.

5.4.4   Sensitivity analysis

A sensitivity analysis was conducted on the model for the following two reasons: (1) to check for the robustness of the model results with respect to the choice of physical parameters and (2) to see how error in the value of the thermal conductivity used can affect the results. Results of the sensitivity analysis for the thermal conductivity are shown in Fig. 5.16. From Fig. 5.16a we can see the percentage change in the time to freeze 30% of the channel cross section as caused by a 20% increase in the value used for the thermal conductivity of water for different Re. For low Re the impact of an uncertainty in the thermal conductivity is low while
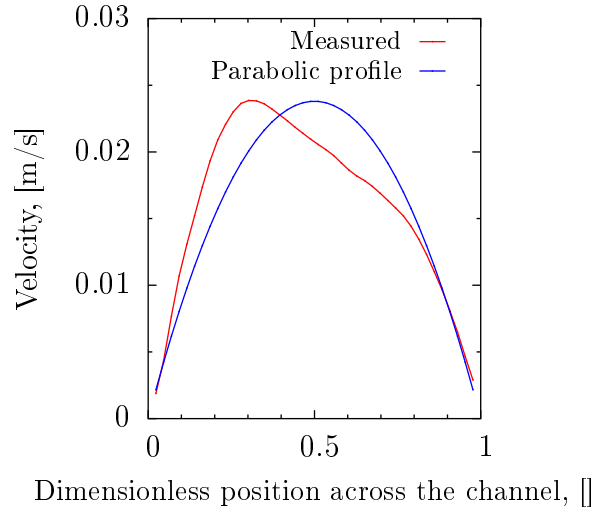
Figure 5.15: Measured local axial velocity component along the channel width compared with the perfect parabolic profile of a fluid with the same flow-rate. Inlet fluid temperature T_0 and average Re are respectively 32.3 °C and 80. The cold surface is at axis position 1.

at high Re it is significant. Same pattern is shown for different inlet temperatures, whose results are offered in Fig. 5.16b. For high Re and high inlet temperature these effects are combined and can result in a significant error in the simulations.

The larger disagreement present between the model and the experimental results at high Re and high T_0 could be therefore explained by the uncertainty in the physical parameters used in the model (which are arbitrary taken as an average between the hot and cold point in the fluid). Also, the present analysis shows again how it is paramount to know accurately the value of the thermal conductivity of the fluid to model freezing at relatively high Re and inlet temperature. This is indeed the case in molten salt nuclear reactor, as it will be shown in the next chapter.

5.5 Conclusion Chapter 5

In this Chapter we described the experimental setup used to study freezing under condition of high wall heat fluxes and high temperature difference between the
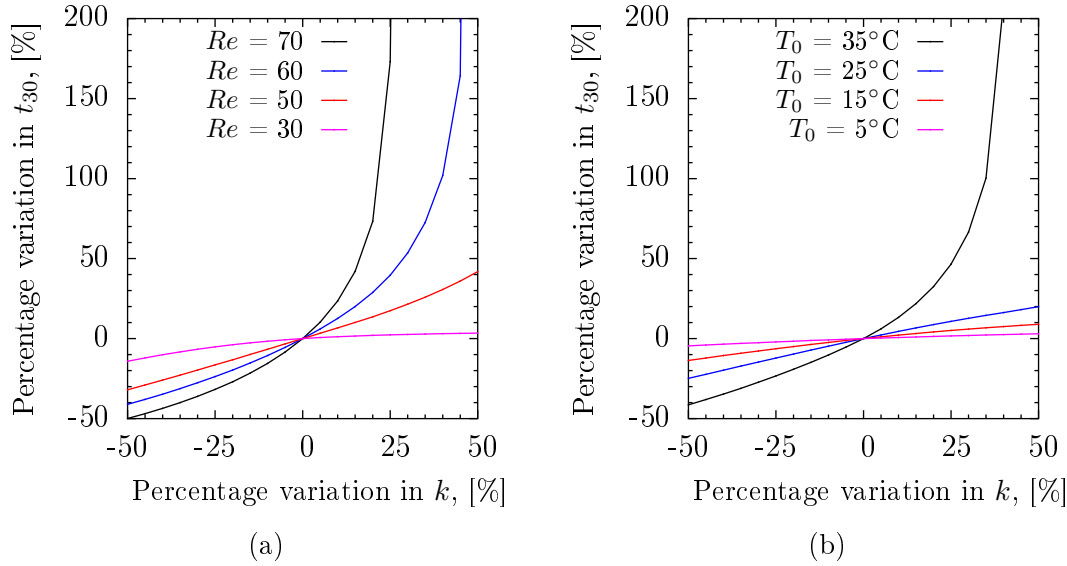
Figure 5.16: Sensitivity analysis of the time to freeze 30 % of the channel, t_{30} on the percentage variation of the thermal conductivity k: a) results for different Re at $T_0 = 30$ channel thickness versus time. b) results for different T_0 at $Re = 50$ channel thickness versus time.

hot and cold fluid. The main results from the experiments and the corresponding numerical simulations are here summarised:

- Accurate tracking of the ice/water interface was possible by (1) measuring the intensity of the scattered signal from the interface and (2) by extrapolating to zero the velocity profile as measured by PIV technique. The two methods gave very similar results with PIV-based measurements performing better at higher Re.

- The growth of the ice thickness with time is approximately linear. This is due to the steady drop in the wall temperature throughout the experiment which partially offsets the increased resistance to the heat transfer caused by the ice growing layer.

- The model described in the previous Chapter can reasonably predict the experimental data with the major sources of error being: (1) time-delay in providing cooling power at the start of the experiment, (2) non-uniformity of the liquid nitrogen at the end of the experiment, (3) uncertainty in the

heat transfer coefficient and physical parameters.

Chapter 6

Transient Freezing in MSR: DRACS Behaviour Under Accident

In this Chapter we show a practical application of the approach described in Chapter 4. We simulated the transient behaviour of the passive safety system DRACS under accident conditions. DRACS, introduced in Section 6.1, is the passive safety system envisioned for the molten salt reactor and it is a critical component of the design which can be prone to freezing. The work undertaken in this thesis has been mostly motivated from the necessity to predict DRACS behaviour as accurately as possible, especially with respect to the issue of coolant freezing in the molten-salt/air heat exchanger. Section 6.2 describes the application of the thermo-hydraulic model developed in Chapter 4 to DRACS. In Section 6.3 the results of the simulations are shown and discussed.

6.1   Introduction to MSR and DRACS

'Generation-IV' molten-salt reactors (MSRs) have been recently experiencing a renaissance, with a growing interest in proposing new reactor concepts and, specifically, in developing various MSR designs [112, 7]. The renewed interest in molten-

salt reactors arises from a variety of factors including, primarily, their inherent safety; it is undoubtedly true that these reactors can be operated at low pressures, severely reducing the danger of catastrophic structural failure and loss of coolant (LOCA) accidents. The high boiling point and good chemical stability of molten salts also means that the reactor can be operated safely over large temperature excursions, while a high negative reactivity coefficient vastly increases the stability of the reactor core.

However, MSRs can be susceptible to other potential safety issues which do not affect most of the reactors currently in operation. One of these safety concerns involves the freezing of the molten salt, which is a sensitive problem, mainly because of the relatively high melting points of the salts (approximately 450 °C) and the lack of sufficient practical experience with such events. Freezing can be harmful mainly for two reasons: (1) by damaging equipment through volumetric expansion due to phase change; and (2) by clogging the pipes and preventing fluid circulation for heat removal (cooling).

These issues were recognised long ago during the early (proof of concept) stages of employing molten salts as coolants in the molten-salt reactor experiment (MSRE) in the 1960s. The MSRE test reactor featured a series of auxiliary electric heaters to prevent the salt from solidifying. In addition, the radiator, which served as the heat rejection unit for the reactor, was equipped with magnetic air doors which were automatically shut in case of a power failure. Their purpose was to passively prevent an uncontrolled air flow through the radiator in case of accident, which could lead to the possible freezing of the salt, dangerously clogging the heat rejection unit [113]. Unfortunately all these safety features, which relied on an external power supply, could not guarantee the safety of a scaled-up reactor.

In order to assess further the safety of MSRs it is therefore very important to achieve a good understanding of the salt freezing issue and to find suitable safety criteria to avoid its occurrence. As part of this effort, we have conducted a thermo-

hydraulic analysis of DRACS, the passive safety system envisioned for the MSRs. DRACS is a promising passive safety system capable of removing the decay heat from the reactor through the natural convection of the molten salt. In this context, damage to this safety system caused by a freezing event, can hamper its effectiveness in removing the decay heat from the reactor under accident conditions, leading to serious problems.

Referring to the schematic in Fig. 6.1, in its most basic form DRACS comprises two thermally interconnected natural-convection loops (termed 'primary' and 'secondary') with molten salt as the heat-transfer fluid in both loops, connected through the DRACS heat exchanger (DHX). It also features a natural draft heat exchanger (NDHX), which is a molten salt/air heat exchanger whose purpose is to reject the decay heat from the secondary loop to the environment. During normal operation, the circulation of molten salt in the two DRACS loops has to be reduced in order to avoid parasitic losses of thermal energy and (thus) maintain the efficiency of the reactor. The inhibition of such parasitic flow is accomplished by: (1) the presence of a fluid diode in the primary loop which greatly reduces the upwards flow through the diode and into the DHX when the pumps are active; and (2) the partial or total closure of the air inlet at the NDHX, which increases the temperature and reduces the natural circulation in the secondary loop. In case of accident, such as loss of forced circulation (LOFC), the air inlet is opened and natural circulation is initiated by the temperature differences in both the primary and secondary loops. Because the decay heat is ultimately removed through the NDHX, freezing of the molten salt in this heat exchanger could be catastrophic. Indeed the mass of solidified salt could severely reduce, if not completely stop, the circulation in the secondary circuit creating a strong temperature difference between the DHX and the NDHX, and compromising the heat removal capability of DRACS. It is therefore important to assess the susceptibility of DRACS to this mode of failure.

The objective of the next sections is to study the potential for transient freezing
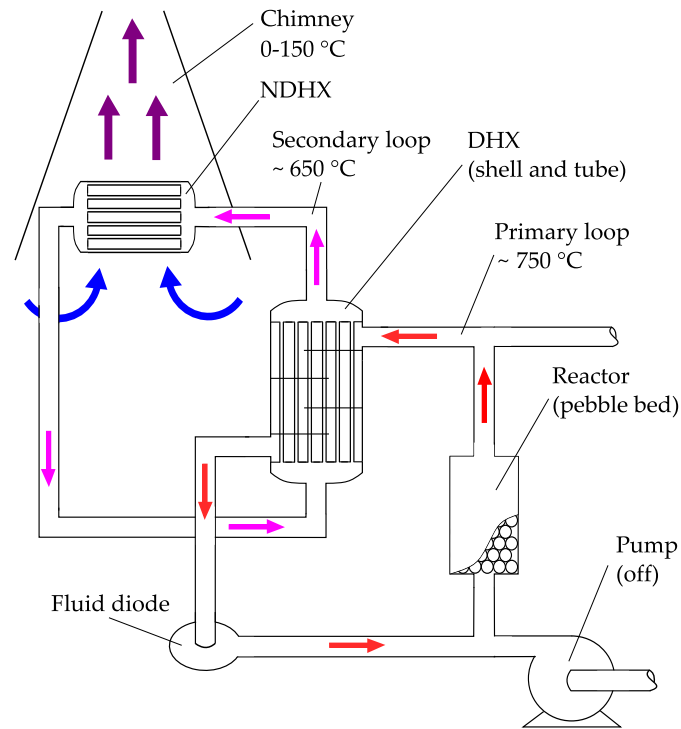
Figure 6.1: A schematic of DRACS during loss of coolant accident. The downwards flow direction through the DHX and the fluid diode in the primary loop indicated in the figure is the preferential direction during accident conditions. During normal operation this flow, as well as the counter-clockwise flow in the secondary loop, are inhibited by the fluid diode and by closing the external air inlet at the NDHX so that the majority of the high pressure molten salt delivered by the pumps flows mainly through the reactor and out (to the right in the figure) to the thermodynamic power cycle.

in DRACS following a blackout with consequent LOFC and loss of power to the (possible) electric heaters, with scram, and to give design criteria to avoid it. As an illustrative case, we base the present work on the preliminary DRACS design described in Ref. [114].

6.2   Model Application to DRACS

The model described in Chapter 4 and comprising the freezing model (Section 4.2) and the thermo-hydraulic model (Section 4.4) was applied to DRACS. The performance of DRACS greatly depends on its design, which consists of a number of different units, each with its own geometrical parameters. Because a comprehensive, full-parametric study of DRACS is difficult and too complex to reveal basic insight, it was decided to apply the model to an arbitrarily-chosen, particular design, with the aim of extracting valuable general information and illustrating any possible safety issues. The design adopted in the current study is very similar to the preliminary design described by Lv and co-workers [115]. The rationale behind this choice is that a good amount of valuable work has already been done on such a design by the mentioned authors and enough information is available on its main components. Where specific information on their design could not be found, assumptions are made so that the steady-state conditions (flow-rates, pressure drops, temperatures) are replicated. The design adopted in this study is summarised below.

The primary loop is a 150 mm ID, 170 mm OD pipe with an overall elevation of 4 m. The differential elevation between the bottom of the reactor and the top of the DHX (3.5 m) is chosen so that the nominal flow-rate of 1.84 kg/s (Ref. [115]) is obtained under steady-state conditions. The pebble-bed reactor is supposed to be a porous medium of area 1.77 m^2 and height 2.5 m, with a 44% porosity. The decay heat of the reactor is taken to be 0.2 MW, unless otherwise stated. The

DHX is a one-pass, shell-and-tube heat exchanger. It is composed of 196, 15.9 mm OD, 13.3 mm ID tubes of length 1.21 m, placed vertically in a triangular layout. There are 4 baffles with a 25% baffle cut. The diameter of the shell is 0.35 m, while the diameter of the tube bundle is 0.34 m. The secondary loop is a 150 mm ID, 170 mm OD pipe with an overall elevation of 0.5 m. The latter value is again decided in order to reproduce the steady-state secondary flow-rate described in Ref. [115]. The NDHX is assumed to compose of 100, 15.9 mm OD, 13.3 mm ID tubes of length 1.93 m, placed horizontally in two rows. The chimney is taken to be 10 m tall with a cross-sectional area of 4 m^2.

The coolant in the primary loop is molten FLiBe, initially assumed to have a (spatially) uniform temperature $T_{1,0}$ in the range $650 - 850$ °C, and a zero initial flow-rate $W_{1,0} = 0$. The secondary-loop coolant is assumed to be FLiNaK, with a spatially uniform, initial temperature equal to the primary-loop initial temperature. The external air-duct is supposed closed initially (at $t < 0$) with zero heat flux at the NDHX. The ambient temperature $T_{\mathrm{air,in}}$ is conservatively considered to be 0 °C, which results in outlet temperatures $T_{\mathrm{air,out}}$ between 50 °C and 100 °C. Some clarification is needed on this choice of initial conditions. They refer to the ideal case where parasitic loses from the reactor are absent. Even if, in reality, heat losses will occur from the secondary loop, they are likely to be severely reduced by the closure of the air shutters. The air shutters need to be closed during normal operation to avoid the very likely freezing of the salt in the NDHX. With the absence of air circulation in the NDHX before the LOFC, it is not unreasonable to adopt the current conditions for the initial state of DRACS.

The thermophysical properties of the two molten salts, the air, fuel and steel used in the simulations are evaluated at each iteration based on the average temperatures in each section of each loop. The values of the thermophysical properties of the molten salts were taken from Ref. [116]. The density of solid FLiNaK was taken from Ref. [117], while its specific heat capacity and heat of fusion were taken from Ref. [118], in accordance with Ref. [115]. Even if the more accurate values of the

Table 6.1: Correlations used for the thermophysical properties of molten salts. References are given in the text. T is the absolute temperature in [K] throughout.

	Thermal conductivity $(\mathrm{W\,m^{-1}\,K^{-1}})$	Specific heat $(\mathrm{J\,kg^{-1}\,K^{-1}})$	Density $(\mathrm{kg\,m^3})$	Viscosity $(\mathrm{kg\,m^{-1}\,s^{-1}})$
Molten FLiBe	$0.63 + 5 \times 10^{-4}T$	2415	$2410 - 0.49T$	$1.1 \times 10^{-5}\exp\left(\frac{3755}{T}\right)$
Molten FLiNaK	$0.43 + 5 \times 10^{-4}T$	1884	$2730 - 0.73T$	$4.0 \times 10^{-5}\exp\left(\frac{4170}{T}\right)$
Solid FLiNaK	0.486	$1300 - 0.97T +$ $1.53 \times 10^{-3}T^2$	2320	—

thermal conductivity (given in Section 3.4) should be used, the present approach allows for a direct comparison with the results of previous studies (Ref. [115]). It is however important to mention that the use of the more accurate and lower value of the thermal conductivity of the liquid salts would further promote the freezing of the coolants. The melting point of FLiNaK is considered to be the generally accepted value of 454 °C, while its heat of fusion was taken again from Ref. [118] as being equal to 3.98 $\times$ 10^5 J/kg. The thermal conductivity of solid FLiNaK was taken from Ref. [119]. All the thermophysical properties are summarised in Table 6.1.

Pressure drops in pipes are calculated according to the Darcy-Weisbach equation as described by Eq. 4.12. The pressure drop in the shell-side DHX is calculated following the approach described in Chapter 10 of the Chemical Engineering Handbook [110]. The pressure drops at the fluidic valve and on the air-side of NDHX are calculated using form (minor) loss coefficients:

$$\Delta P = K \frac{W^2}{2\rho A_\mathrm{d}^2}\,. \tag{6.1}$$

For the fluidic valve, a value of 0.38 is taken for K, determined approximately from the study of Lv et al. [120], and the area A_d is assumed to be approximately 0.001 m^2, such that the pressure loss in the reactor is approximately 330 Pa at 1.84 kg/s (see Ref. [115]). The values of K and A_d for the NDHX are calculated so

that the steady-state air flow-rate is 3.31 kg/s. The pressure drop in the reactor is calculated using the Ergun equation:

$$\Delta P = \frac{170\mu L_r}{D_p^2}\frac{(1-\epsilon)^2}{\epsilon^3}\frac{W}{\rho A} + \frac{1.75L}{D_p}\frac{(1-\epsilon)}{\epsilon^3}\frac{W^2}{\rho A^2}\,. \tag{6.2}$$

The average porosity ϵ is assumed to be 0.44 while the effective particle diameter D_p is taken equal to 0.03 m. With such values the pressure drop at a mass flow-rate of 1.86 kg/s is around 13 Pa.

The pipe-side heat transfer coefficients are calculated using the following relations for laminar and turbulent flow:

$$\begin{cases} Nu = 3.65 + \frac{0.0668RePrD/L}{1+0.04RePrD/L} & \text{for} \quad Re < 2300\,; \\ Nu = 0.027Re^{0.8}Pr^{0.3} & \text{for} \quad Re > 2300\,. \end{cases} \tag{6.3}$$

The shell-side heat transfer coefficient in the DHX is calculated following the approach described in Chapter 10 of the Chemical Engineering Handbook [110].

Regarding the conditions in the NDHX, T_{ext} which represent the ambient air temperature (Eq. 4.15), is considered constant because the heat exchanger is assumed to be horizontal and flat. The value of T_{ext} is taken as an average between the ambient temperature entering the chimney $T_{\text{air,in}}$ (which is given and fixed) and the temperature leaving the chimney $T_{\text{air,out}}$. This latter temperature is found by assuming that the flow through the chimney is adiabatic and by considering an energy balance over a control volume around the NDHX:

$$T_{\text{air,out}} = T_{\text{air,in}} + \frac{h_{\text{ext}}(T_{\text{w}} - T_{\text{ext}})P_{\text{ext}}}{W_{\text{air}}c_{\text{p air}}}\,, \tag{6.4}$$

in which W_{air} is the mass flow-rate of air through the chimney and $c_{\text{p air}}$ is the specific heat capacity of the air. The mass flow-rate W_{air} is found by matching the total draft pressure ΔP_{draft} with total pressure loss in the chimney, which is composed of the pressure loss over the NDHX (ΔP_{NDHX}) and the (major) frictional

loss along the length of the chimney ΔP_{chim}:

$$\frac{\mathrm{d}W_{\text{air}}}{\mathrm{d}t}\frac{L_{\text{chim}}}{A_{\text{chim}}} = \Delta P_{\text{draft}} - \Delta P_{\text{NDHX}} - \Delta P_{\text{chim}}\,, \qquad (6.5)$$

where L_{chim} and A_{chim} are the length and average surface area of the chimney. The NDHX air-side heat transfer coefficient was not calculated through a correlation. Indeed the results were found to be very sensitive to the air-side heat transfer coefficient in the NDHX. It was therefore decided to conduct a parametric analysis in which the steady-state heat transfer coefficient h_{ss} was used an input parameter in the model and the results of the simulations were expressed as its function (see next section). The transient heat transfer coefficient in the NDHX is obtained from the steady-state coefficient h_{ss} using:

$$h = h_{\text{ss}} \left(\frac{W_{\text{air,ss}}\rho}{W \rho_{\text{air,ss}}} \right)^{0.6}\,, \qquad (6.6)$$

where $W_{\text{air,ss}}$ and $\rho_{\text{air,ss}}$ are the nominal (steady-state) mass flow-rate and density of air. Eq. 6.6 was derived from the predictive equation for air flow through finned tubes described in Ref. [110]. In the reactor the heat flux is imposed and, as such, no heat transfer coefficient is needed.

A brief comment has to be given regarding the validity of applying the code previously developed to DRACS. In Chapter 4 and 5 the overall model was tasted against experimental and theoretical studies with reasonably good results. Unfortunately however an experimental test case for freezing in a natural convection, which could provide a strong case to benchmark any code, does not exist. However, models similar to the one described in Section 4.4 (without taking into account any freezing) have been tested on experiments done on natural convection loop, see in this respect Ref. [121]. We can therefore have a reasonable assurance that the overall model of the system (freezing + thermo-hydraulics) is still valid. It could indeed be argued that the thermohydraulic dynamics of the whole loop are relatively decoupled from the physical processes of freezing. With respect to sim-

ulating the thermohydraulic behaviour of the loop, the freezing process can be considered very similar to an added, time-varying, pressure drop. Correspondingly, the behaviour of the loop can be regarded as a time-varying inlet condition with respect to the problem of transient freezing in pipe flow.

6.3 Results of DRACS Transient Simulations

To illustrate the potential safety issues in DRACS arising from the possible freezing of the coolant in the NDHX, we consider different scenarios obtained by varying the steady-state, air-side heat transfer coefficient h_{ss}. The value of the h_{ss} is usually assumed during the design stages of DRACS, and is then used to size the NDHX. Therefore, the results provided in this section can be seen as an investigation of possible errors in designing the NDHX, and the consequences thereof, due to uncertainties or over-conservative approaches in estimating h_{ss}. In general, two potential dangerous behaviours can be encountered for too large a value of h_{ss}: (1) the salt freezes slowly but continuously after the early transient until complete clogging of the pipes occurs; and (2) the salt freezes in the early stages of the transient when the loops exhibit a highly oscillatory behaviour. For a average/high initial loop temperature, Case (2) is unlikely to occur and Case (1) is more important.

To illustrate the first mode of failure, Case (1), we conducted two simulations using different values of h_{ss}. In the first simulation, a 'nominal' value of 35 W/m^{2}K was assumed, which is approximately equal to the nominal heat transfer coefficient that matches the nominal temperatures, flow-rates and pressure drops found in Ref. [115]. In the second simulation, a value of 60 W/m^{2}K was used, which represents a 71% increase with respect to the nominal heat transfer coefficient value. The results of the two transient simulations corresponding to these two scenarios are shown in Figs. 6.2a–6.4b. For both simulations an initial temperature

of 650 °C was assumed.

(a)   (b)

Figure 6.2: Transient profiles for different value of the NDHX steady-state heat transfer coefficient h_{ss}: a) Transient mass flow-rate of the secondary loop, b) Transient mass flow-rate of the primary loop.

In the $h_{\mathrm{ss}} = 35$ W/m^{2}K case, instabilities (fluctuations) are observed in the temperatures and flow-rates which last for approximately 1500 s, after which the transient profiles are found to almost reach steady-state. The temperature at the exit of the NDHX is seen to drop significantly from 650 °C to 560 °C in the first 100 s (Fig. 6.3a), as a result of the low secondary flow-rate (Fig. 6.2a). However, the temperature increases again once the secondary flow is initiated. The maximum temperature in the reactor during this early transient increases by approximately 50 °C. Importantly, the wall temperatures of the NDHX and everywhere else in DRACS are always above the melting temperature of the salt (Fig. 6.4b), such that no salt freezes in the NDHX (Fig. 6.4a). Overall the behaviour of DRACS is considered acceptable with the temperatures being maintained within the safety limits.

When using a value of $h_{\mathrm{ss}} = 60$ W/m^{2}K, the results predicted by the model are substantially different. Similarly to the nominal-value simulation, the early transients/instabilities last approximately 1500 s, during which time all quantities of interest remain within the safety limits. However, an augmented natural circula-

Figure 6.3: Transient profiles for different value of the NDHX steady-state heat transfer coefficient h_{ss}: a) Transient temperature profiles at the entrance ($T_{2,in}$) and exit ($T_{2,out}$) of the NDHX, b) Transient temperature profiles at the entrance ($T_{1,in}$) and exit ($T_{1,out}$) of the reactor.

tion in both loops is observed, compared to the nominal-value simulation, due to the higher temperature differences in each of the loop legs, which is caused by the higher value of imposed h_{ss}, as expected. The inlet and outlet temperatures of the reactor are lower than those found in earlier case with the lower value of h_{ss}, due to the higher rate of thermal-energy removal at the NDHX. As in the previous case, the temperature at the exit of the NDHX drops in the early stage of the transient and quickly recovers. However, once the flow stabilises, the wall temperature close to the exit of the NDHX starts to decrease slightly until it falls below the melting temperature of the salt (see Fig. 6.4b). At this point (after around 1350 s), freezing of the molten salt takes place at the wall surface, as shown in Fig. 6.4a. The newly formed mass (deposit) of salt on the pipe wall partially obstructs the pipe cross-section at this location, leading to an increased pressure drop in the NDHX, which in turn causes the secondary flow-rate to slightly decrease (see the blue line in Fig. 6.2a). A diminished flow-rate, results in a lower heat-capacity rate ($\dot{m}c_{p}$) and a higher temperature drop in the bulk of the liquid salt, which consequently leads to further freezing.
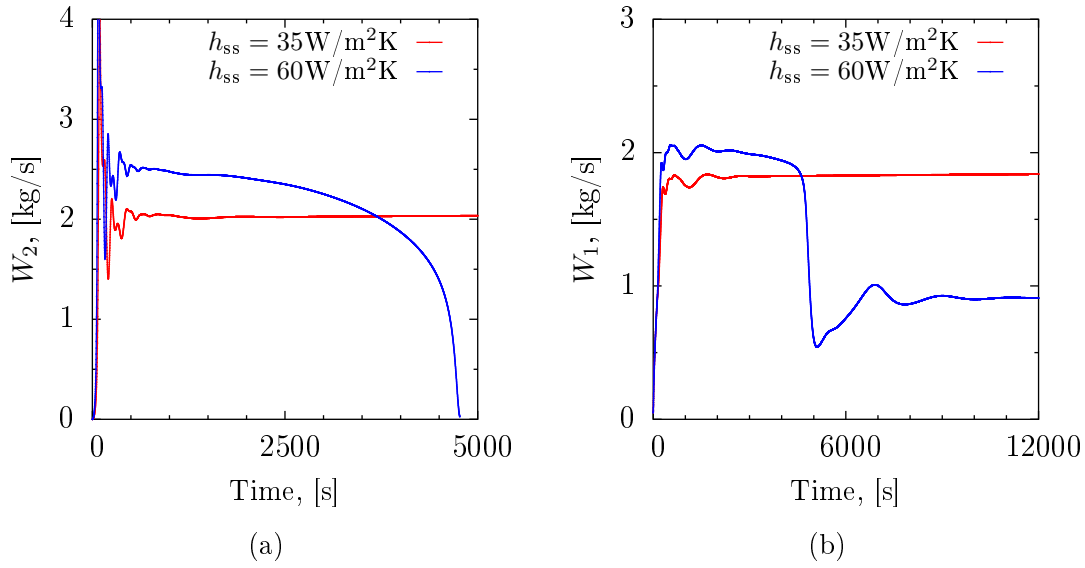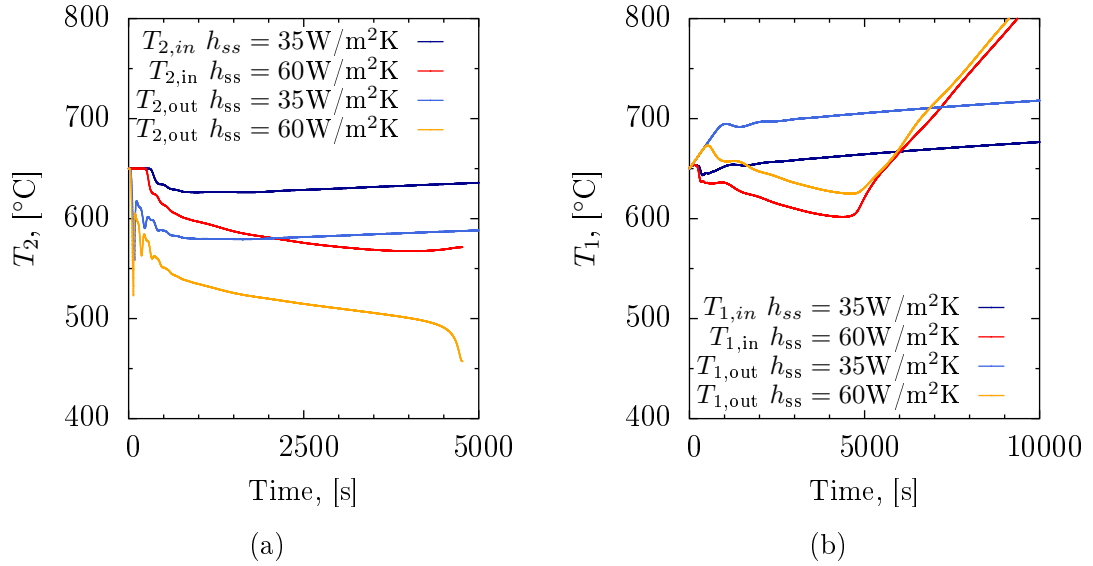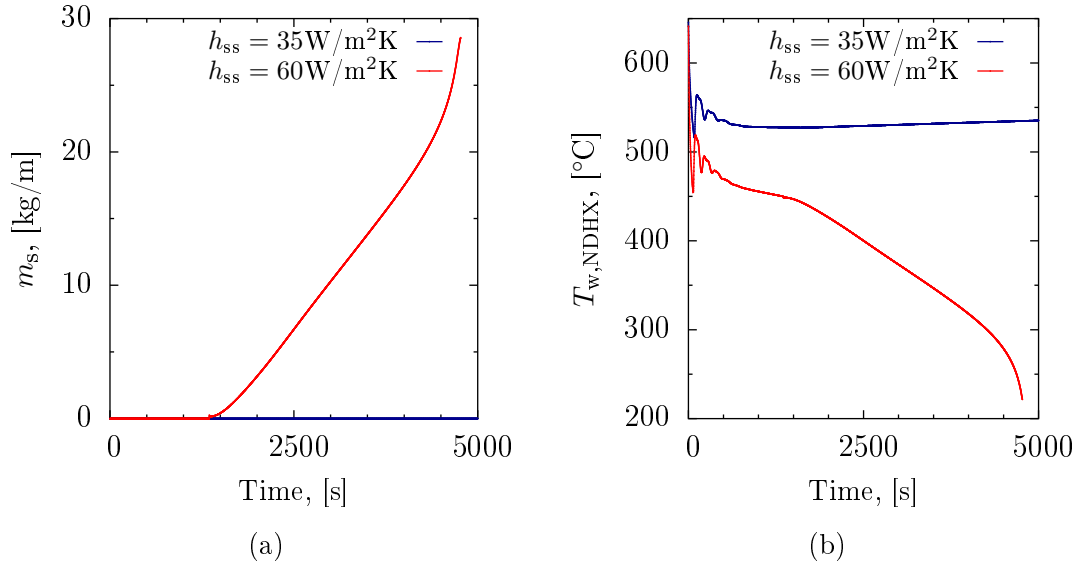
Figure 6.4: Transient profiles for different value of the NDHX steady-state heat transfer coefficient h_{ss}: a) Solidified mass of salt per unit length in each pipe close to the exit of the NDHX, b) Transient wall temperature profiles close to the exit of the NDHX.

It is observed from the results here that this process does not stabilise at some equilibrium condition, instead it progresses until the NDHX pipes are completely clogged. In the simulation, the secondary flow ceases after approximately 4700 s (Fig. 6.2a). Without any secondary flow, the temperature in the reactor rises steadily (Fig. 6.3b) until it goes outside the safety limit (not shown in the figure). It is noted that the primary mass flow-rate does not go to zero, even if it severely diminishes, due to the remaining (non-zero) temperature differences in the legs of primary loop. This mode of failure of DRACS is caused by an intrinsic instability of the coupling between the freezing process and the flow in the natural convection loop. The scenario, however, is not always the case and, depending on the conditions, a stable flow can be achieved even in the presence of a frozen layer of salt in the pipes. In this latter case, the frozen layer of salt acts as a thermal insulator without obstructing excessively the flow of liquid in the loop.

The second mode of DRACS failure, Case (2), is related to freezing in the NDHX during the early transient when the secondary flow is highly unstable. In this case, the occurrence or not of any pipe clogging is related to the initial conditions on the

DRACS system, in particular its initial temperature. A higher initial temperature of the loop will delay the freezing of the salt until the secondary loop achieves a stable condition. This scenario is shown in Figs. 6.5a – 6.6b, which show results from the DRACS simulations for two different initial loop temperatures: 650 °C and 660 °C. The decay heat of the reactor here was set to 0.4 MW and the value of h_{ss} to 100 W/m²K. Figure 9 shows, in both cases, that the wall temperature at the exit of the NDHX drops well below the freezing point of the salt very quickly, giving rise to freezing. For an initial temperature of 650 °C this leads to complete clogging of the pipe after 1500 s, as a consequence of which the secondary flow-rate goes to zero (Fig. 6.6a) and the temperature of the reactor exceeds the safety limit (Fig. 6.6b). For an initial temperature of 660 °C, however, the situation recovers with partial re-melting of the salt (Fig. 6.5a). In this case, the higher initial temperature of the liquid delays the freezing process for enough time, until the loop achieves a stable thermohydraulic condition. It is worth noting that, contrary to what found previously for the Case (1) failure mode, this stable condition allows for the wall temperature at the exit of the NDHX to be below the freezing point. In this case, a stable solidified layer of salt acts as a thermal insulator, as shown in Fig. 6.5a.

From the previous analysis it emerges that two fault conditions need to be evaluated when designing DRACS for a molten-salt reactor. The first is related to an unstable behaviour in the loop close to steady-state and the second one is related to a sudden freezing of the salt in the early transient. Because of the large number of parameters involved in the design of these systems, and the absence of experimental data, it is difficult to provide precise guidelines on DRACS design to avoid salt freezing. In Ref. [114] the bulk temperature of the salt in the NDHX was taken as a criterion for an evaluation of the susceptibility of DRACS to freezing. *We consider that this criterion should be used with caution.* Indeed most of the simulations which predict the clogging of the NHDX, showed bulk temperatures always above the melting point when run with the freezing model artificially dis-
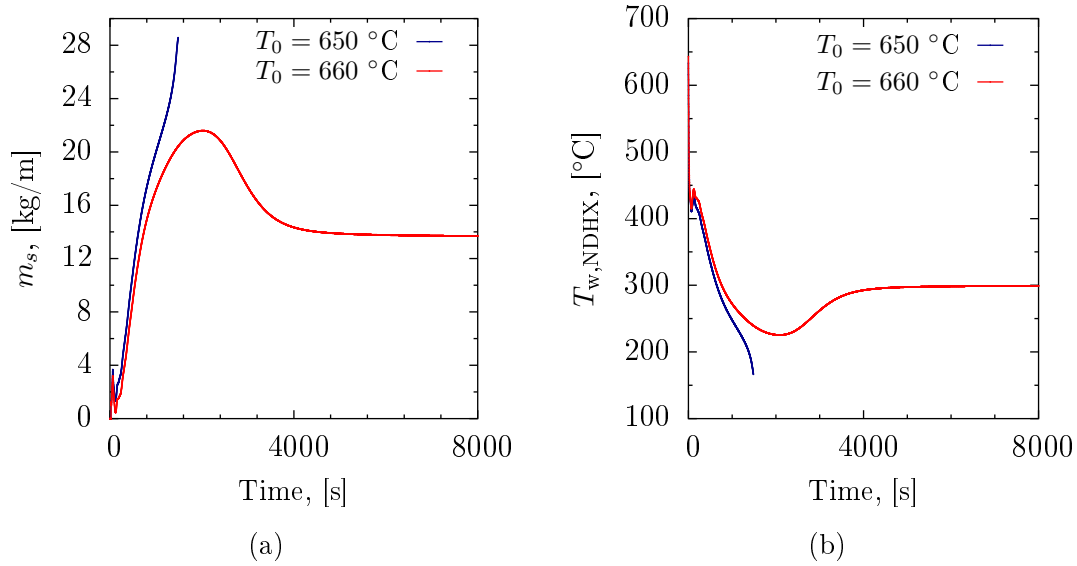
Figure 6.5: Transient profiles for different initial loop temperature T_0: a) Solidified mass of salt per unit length in each pipe close to the exit of the NDHX, b) Transient wall temperature profiles close to the exit of the NDHX.

abled. We suggest that, in light of this complex thermo-hydraulic behaviour, that the wall temperature should be considered as an improved criterion to quickly check for the validity and soundness of a DRACS design. In particular, it would be desirable for the wall temperature not to drop below the freezing point of the salt in any parts of the loop, or:

$$T_{\mathrm{w}}(t, s) > T_{\mathrm{melt}} \quad \forall\, t,\, s\,. \tag{6.7}$$

Due to the large number of DRACS design parameters and the considerable uncertainties associated with their values, it can be difficult to establish with confidence whether a design is safe of not with respect to freezing. In an effort to understand further which conservative criteria can be facilitate quick, early-stage design evaluations, we conducted a parametric analysis on some of the most important and least certain parameters. One of these parameters is the decay heat from the reactor which, especially for molten salt reactors, cannot be known accurately due to the very few experimental data available in the literature.

Figure 6.7 shows the freezing time required to clog 99% of the pipe cross-sectional
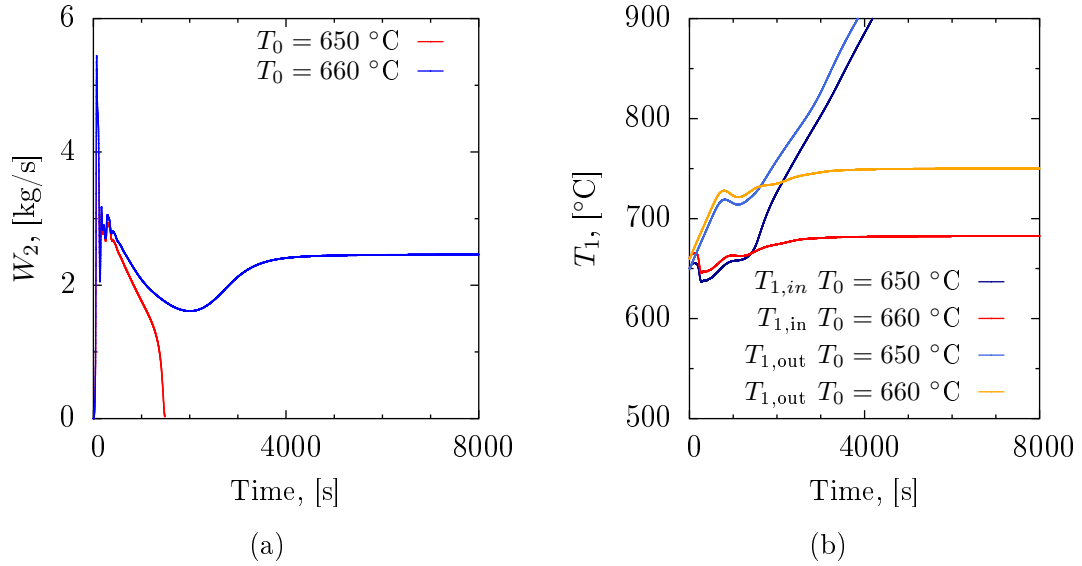
Figure 6.6: Transient profiles for different initial loop temperature T_0: a) Transient mass flow-rate of the secondary loop, b) Transient temperature profiles at the entrance $(T_{1,\text{in}})$ and exit $(T_{1,\text{out}})$ of the reactor.

area for different values of the decay heat $\dot{Q}$ and h_{ss}, for an initial loop temperature of 650 °C. In all the simulations larger decay heat values are found to suppress the freezing process. This is understandable, as a larger decay heat will increase the temperature of both the primary and secondary loops. A larger decay heat, however, also increases the oscillatory behaviour in the early transient which could act to promote an early freezing of Type (2). This effect, on the other hand, was found to be largely compensated for by the increase in the temperature of the loops. Therefore, a lower value of the decay heat is considered conservative for a safety analysis.

In Fig. 6.8 the results of a parametric analysis on the initial temperature of the loops are shown. The freezing time to block 99% of the NDHX pipe cross-sectional area is reported for different initial temperatures of the loops and value of h_{ss}. As expected, a higher initial temperature increases the freezing time and thus lower initial temperatures can be regarded as conservative. The two modes of freezing described previously in this section can be seen in Fig. 6.8. For moderate/high initial temperatures of the loop, the susceptibility of a DRACS design to freezing is independent on the initial temperature. In this case, the salt freezes due to an
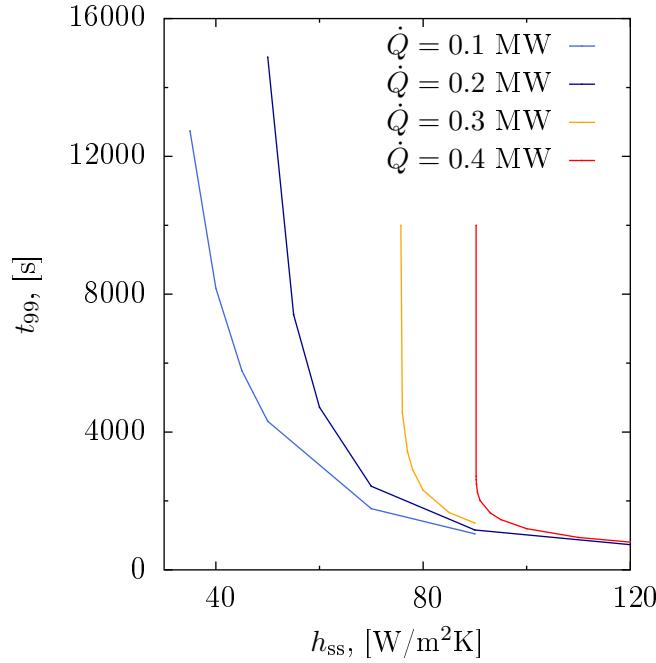
Figure 6.7: Time to freeze 99% of the NDHX pipe cross sectional area for different values of the decay heat $\dot{Q}$ and h_{ss}. Initial temperature of the loops is 650 °C.

intrinsic instability of DRACS. The only effect of a higher initial temperature is to delay the occurrence of freezing. All the profiles (for $T > 600$ °C) have the same minimum h_{ss} value, below which freezing is prevented ($h_{\mathrm{ss}} \sim 50$ W/m²K). For lower initial temperatures of the loop, freezing can occur at even lower values of h_{ss}. In this case, the salt freezes in the early stages of the transient.

It is important to discuss briefly the accuracy of the present approach, especially with respect to the axial heat conduction through the wall and the solidified layer of fluid. Axial heat conduction is indeed neglecetd in the model and could affect the results reported in this work by smoothing the temperature gradients across each pipe section. Axial conduction is likely not to have a considerable effect on the validity of the results after the NDHX pipes have become clogged by the salt. Indeed, even if conduction can be significant over short lengths due to the high temperature gradients involved, once the flow is stopped the freezing process is probably irreversible due to the long piping distance between the DHX and the NDHX. Assuming a piping system several meters long, the time-scale for temperature information to propagate via conduction between the two heat
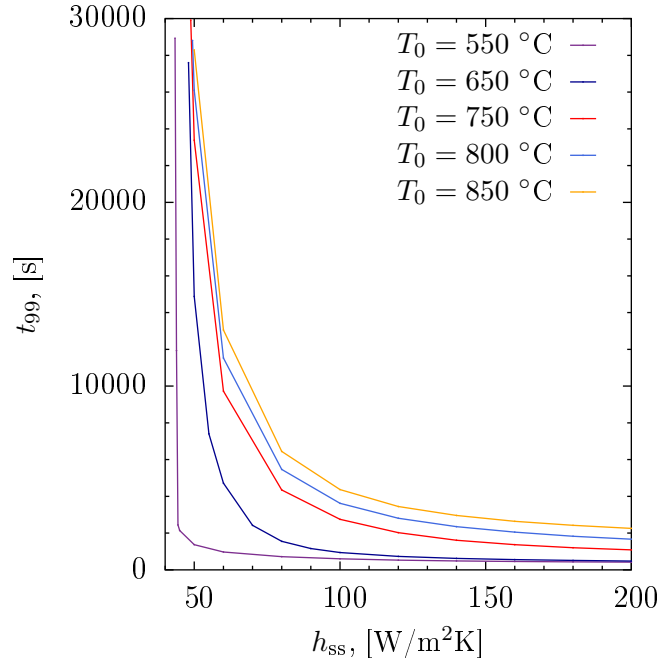
Figure 6.8: Time to freeze 99% of the NDHX pipe cross sectional area for different values of the initial temperature of the loops T_0 and h_{ss}. The decay heat is assumed to be 0.2 MW.

exchangers would be higher than 10^5 s, both in the wall and in the salt. A question arises as to what extent axial conduction can limit the freezing process when the flow is not completely clogged. A precise answer cannot be provided at this stage. Therefore, in the case where axial conduction through the NDHX wall is significant, the results of the present study should be regarded as quantitively conservative.

Lastly it is important to mention that the previous simulations were conducted by using a constant value of the reactor decay heat. In reality, the decay heat diminishes with time and freezing is therefore further promoted after the first few hours of DRACS operation.

6.4   Conclusion Chapter 6

The model described in Chapters 4 and 5 was applied to study the feasibility of the DRACS passive safety system of MSRs.

The main findings of the analysis conducted are:

- The model results suggest a possible safety concern with the DRACS passive safety system under certain circumstances that define an inadequate safety-system design. Specifically, DRACS and, by extension MSRs, are susceptible to failure following freezing in the NDHX, which acts to almost entirely block any heat-removal capability during an accident.

- Two possible modes of failure due to freezing have been identified and characterised. The first one is related to a (possible) intrinsic unstable behaviour of DRACS in which the formation of a first solid layer at the wall increases the pressure drop in the secondary loop which decreases the flow-rate and, in turn, promotes further freezing. The second one arises in the early stages of the transient when the temperatures and flow-rates are not yet stabilised and can locally promote a high freezing rate; this second behaviour is very dependent on the initial conditions.

- The wall temperature should be considered as a conservative criterion based on which it is possible to quickly evaluate the feasibility and adequacy of a design. In particular, the wall temperature of the NDHX (and other parts) should not fall below the melting point of the salt at any time during the transient response of the system. Conservative criteria for the most important/least known variables have been discussed. A low value of the decay heat is taken as conservative, since lower values promote salt freezing in the NDHX, even if higher values promote the early transient instabilities of the loops. For moderate-to-high initial loop-temperatures, an increase in the initial temperature of the loops does not affect the occurrence or not of complete freezing, and only increases the time to reach this condition. For low initial loop-temperatures, an increase in the initial temperatures of the loops will prevent sudden freezing during the early transient.

- The use of conventional, over-conservative approaches in the thermal design of the NDHX (the molten salt/air heat exchanger), which would tend to oversize the heat transfer coefficient and the heat transfer area, can have serious consequences as they may act to promote salt freezing, resulting in clogging of the pipes, and thus should be avoided.

Chapter 7

Conclusions

7.1   Summary of Thesis Achievements

The overriding aim of the work presented in this thesis was to address the issue of molten salt flow solidification (freezing) in piping systems by providing an approach to quantify the solidification of the molten salt (in terms of mass build-up, effect on the flow and heat transfer, etc.). Several aspects which mostly affect the accuracy of the predictive capabilities of relevant codes were addressed. Specifically, we considered the following aspects of this problem: 1) developing an experimental method, based on the transient hot wire method, to measure the thermal conductivity of molten salts at high temperatures; 2) providing new data for the thermal conductivity of molten salts, whose uncertainties in the value significantly affect any modelling efforts; 3) developing a transient thermo-hydraulic model to simulate the freezing process inside piping systems; 4) building an experimental apparatus to characterise transient freezing in internal flow under high heat fluxes also as a means to validate the aforementioned model; 5) applying the model to the 'Direct Reactor Auxiliary Cooling System' (DRACS), which is the passive-safety system proposed for the Generation-IV molten salt reactors.

The main findings from this work are summarised as follows:

- An experimental technique consisting of a U-shaped quartz capillary filled with molten Galinstan was developed and successfully applied to measure the thermal conductivity of molten salts up to temperature of 760 K, with an overall accuracy better than 4%.

- The thermal conductivity of $NaNO_3$–$NaNO_2$–KNO_3 eutectic (HTS) and LiCl–KCl eutectic were measured up to temperatures of 700 K and 760 K respectively. The reported expanded uncertainty (95% confidence interval) in the measurements is 3.1% for HTS and 9.1% for LiCl–KCl. The results regarding LiCl–KCl were considered unreliable due to the high scatter in the measurements, probably caused by the low purity of the sample. In addition, the results of Smirnov et al. [35] were re-evaluated by taking into account the thermal losses present in its instrument; the new results were in good agreement with other studies. We used our measurements and Smirinov's re-evaluated data to critically review and suggest the values of thermal conductivity for the most common type of salts, including FLiNaK. The uncertainty in the suggested values is 5%-20%, compared with the 10%-80% of the literature.

- A 1-dimensional thermo-hydraulic model was developed under the steady state assumption and validated to predict transient freezing in internal flow. The model can be incorporated in standard thermo-hydraulic codes and can be used to predict the solidification process in complex piping systems where CFD is computationally too expensive.

- An experimental rig equipped with laser-based diagnostic techniques was build to measure the growing thickness of an ice layer in contact with a cold surface and a water pipe-flow. The large temperature differences between the wall and the fluid resembled the conditions found in molten salt applications, such as DRACS, and showed the importance of the wall thermal mass on the growth of the solidified layer. The velocity profiles in the fluid in contact

with the ice were also measured via Particle Image Velocimetry. The freezing model developed was validated against the experimental data and the largest sources of discrepancies were analysed.

- The freezing model was applied to study the behaviour of DRACS in a LOCA scenario with blackout. DRACS was found prone to failure due to freezing in the molten salt/air heat exchanger. The main transient responses of DRACS were characterised and discussed. It was demonstrated how the use of conventional, over-conservative approaches in the thermal design of the the molten salt/air heat exchanger (NDHX), which would tend to oversize the heat transfer coefficient and the heat transfer area, can have serious consequences as they may act to promote salt freezing, resulting in clogging of the pipes, and thus should be avoided.

Other, more specific, conclusions were reached during the development of this work; these have been summarised in the conclusion section of each Chapter. We refer the reader to these sections for a detailed description of the results.

7.2   Applications

The work undertaken and explained in this thesis finds two main fields of application: 1) the model developed can be incorporated in standard thermo-hydraulic codes to simulate transient freezing in pipe flow, a condition which is not currently considered in standard codes, as mentioned in the Introduction; 2) the experimental technique utilised to measure the thermal conductivity can be further developed and optimised in a possible commercial system to be implemented for high temperature measurements of conducting fluids. Many challenges, however, need to be overcome for this second application. The main obstacle is at present the fragility of the connection between the capillary probe and the quartz tube. An innovative step is required to significantly overcome this difficulty. The

use of electrically insulative pastes (adopted in the present study) is probably not enough to guarantee reliable operation at high temperature ($>900\,\mathrm{K}$). One solution could be to manufacture the capillary by drawing it from a quartz tube; a technique which was utilised in previous studies (see Chapter 2).

7.3 Recommendation for future Works

The work presented dealt with liquids which solidified at a specific melting point. This is the case for pure fluids as well as for the more common eutectic mixtures. In real systems, and especially in nuclear applications, it is unlikely that a perfect eutectic composition is stable throughout the process lifetime. Non-eutectic melts can develop through the years or they might be chosen from the start. In liquid fuel MSR, for example, the amount of fuel dissolved is usually selected by taking into account many factors and the resulting fuel/salt mixture is seldom an eutectic. Non-eutectic mixtures do not present an unique melting point; instead, the liquid solidifies over a temperature range by changing its composition. In a scenario which involves non-eutectic melts it is therefore important to study the behaviour of systems which will incur, during melting, in phase separation. The additional contribution of mass transport increases the complexity of the problem which can not be fully analysed with the approach described in this thesis. As such we consider the study of the solidification of non-eutectic melts of primary necessity for the development of MSRs and molten-salts based energy systems in general.

The experimental work conducted in this thesis used water as a simulant for molten salts. The experiment conducted in Chapter 5 should be repeated using low melting point molten salts. The diagnostic techniques utilised for such measurements could be applied in a similar manner to molten salts flows. Such an experiment would also reveal the velocity profile in a molten salt flow, whose measurement has never been attempted before and could offer valuable insights on the

thermo-hydraulics of molten salts near the melting point.

The ability to accurately predict the solidification of molten salts opens the possibility to use such solidification as an advantage instead of a drawback. For example, a solidified layer of salt could be used as a containment barrier to avoid corrosion. A solidified layer of salt could also be used as a thermal buffer to stabilise the temperature transients by melting/solidifying part of the material. Such solutions could be of use especially in fast spectrum MSR, where corrosion and stability are particularly challenging, and should be investigated further.

Lastly the capillary probe, if further developed, could allow for accurate measurements of thermal conductivity ($<1\%$), thus providing high-temperature standards. The accuracy of the capillary probe can be increased by considering appropriate radiation corrections and by adopting a short and long capillary to take into account end effects, in a similar manner to the commonly implemented THWM. The need for high temperature standards should be however ascertained before conducting further work as the experimental difficulties are numerous.

Bibliography

[1] J. S. Wilkes. A short history of ionic liquids: from molten salts to neoteric solvents. *Green Chemistry*, 4(2):73–80, 2002.

[2] D. Kearney, U. Herrmann, P. Nava, B. Kelly, R. Mahoney, J. Pacheco, R. Cable, N. Potrovitza, D. Blake, and H. Price. Assessment of a molten salt heat transfer fluid in a parabolic trough solar field. *Journal of Solar Energy Engineering*, 125(2):170–176, 2003.

[3] P. Hank, L. Eckhard, K. David, Z. Eduardo, C. Gilbert, G. Randy, and M. Rod. Advances in parabolic trough solar power technology. *Journal of Solar Energy Engineering*, 124(2):109–125, 2002.

[4] C. Suárez, A. Iranzo, F. J. Pino, and J. Guerra. Transient analysis of the cooling process of molten salt thermal storage tanks due to standby heat loss. *Applied Energy*, 142:56–65, 2015.

[5] D. Kearney, B. Kelly, U. Herrmann, R. Cable, J. Pacheco, R. Mahoney, H. Price, D. Blake, P. Nava, and N. Potrovitza. Engineering aspects of a molten salt heat transfer fluid in a trough solar field. *Energy*, 29(5):861–870, 2004.

[6] U.S. Deparatment of Enegry. Fluoride-salt-cooled, high-temperature reactor (FHR) subsystems definition, functional requirement definition, and licensing basis event (LBE) identification white paper. Research Project Report, August 2013.

[7] J. Serp, M. Allibert, O. Beneš, S. Delpech, O. Feynberg, V. Ghetta, D. Heuer, D. Holcomb, V. Ignatiev, J. L. Kloosterman, et al. The molten salt reactor (MSR) in Generation IV: Overview and perspectives. *Progress in Nuclear Energy*, 77:308–319, 2014.

[8] C. Renault, M. Hron, R. Konings, and D.E. Holcomb. The molten salt reactor (MSR) in Generation IV: overview and perspectives. *GIF Symposium*, pages 191–200, 2009.

[9] D. F. Williams, L. M. Toch, and K. T. Clarno. Assessment of candidates molten salt coolants for the advanced high temperature reactor. *ORNL/TM-2006/12, 2006a*, 2006.

[10] L. Mathieu, D. Heuer, R. Brissot, C. Garzenne, C. Le Brun, D. Lecarpentier, E. Liatard, J. M. Loiseaux, O. Meplan, E. Merle-Lucotte, et al. The thorium molten salt reactor: moving on from the MSBR. *Progress in Nuclear Energy*, 48(7):664–679, 2006.

[11] J. Richard, D. Wang, G. Yoder, J. Carbajo, D. Williams, B. Forget, and C. Forsberg. Implementation of liquid salt working fluids into TRACE. In *International Congress on Advances in Nuclear Power Plants*. Citeseer, 2014.

[12] L. Frederic and G. Henri. *Molten salts chemistry, from lab to applications*. Elsevier, 2013.

[13] S. Fukusako and N. Seki. Fundamental aspects of analytical and numerical methods on freezing and melting heat-transfer problems. *Annual Review of Heat Transfer*, 1(1), 1987.

[14] J. S. Lee. *RELAP5 Model Benchmark for Thermal Performance of DRACS Test Facilities*. PhD thesis, Iowa State University, 1993.

[15] GOTHIC technical manual, version 7.2a. Technical report, 2006.

[16] R. Ferri, An. Cammi, and D. Mazzei. Molten salt mixture properties in RELAP5 code for thermodynamic solar applications. *International Journal of Thermal Sciences*, 47(12):1676–1687, 2008.

[17] H. C. Lin. *RELAP5 Model Benchmark for Thermal Performance of DRACS Test Facilities*. PhD thesis, The Ohio State University, 2016.

[18] P. Sabharwall, M. Ebner, M. Sohal, P. Sharpe, M. Anderson, K. Sridharan, J. Ambrosek, L. Olson, and P. Brooks. Molten salts for high temperature reactors: University of wisconsin molten salt corrosion and flow loop experiments–issues identified and path forward. *Idaho National Laboratory Report INL/EXT-10-18090*, 2010.

[19] V. M. B. Nunes, M. J. V. Lourenco, F. J. V. Santos, and C. A. Nieto de Castro. Importance of accurate data on viscosity and thermal conductivity in molten salts applications. *J. Chem. Eng. Data*, 48:446 − 450, 2003.

[20] D. F. Williams, L. M. Toth, and K. T. Clarno. *Assessment of candidate molten salt coolants for the advanced high temperature reactor (AHTR)*. United States. Department of Energy, 2006.

[21] M. Salanne, C. Simon, P. Turq, and P. A. Madden. Heat-transport properties of molten fluorides: determination from first-principles. *Journal of Fluorine Chemistry*, 130(1):38–44, 2009.

[22] M. L. V. Ramires, C. A. N. de Castro, Y. Nagasaka, A. Nagashima, M. J. Assael, and W. A. Wakeham. Standard reference data for the thermal conductivity of water. *Journal of Physical and Chemical Reference Data*, 24(3):1377–1381, 1995.

[23] K. Cornwell. The thermal conductivity of molten salts. *Journal of Physics D: Applied Physics*, 4:441 − 5, 1971.

[24] J. W. Cooke. Development of the variable-gap technique for measuring the thermal conductivity of fluoride salt mixtures. *Oak Ridge National Laboratory*, ORNL-4831, 1973.

[25] R. Tufeu, J. P. Petitet, L. Denielou, and B. Le Neindre. Experimental determination of the thermal conductivity of molten pure salts and salt mixtures. *International Journal of Thermophysics*, 6(4):315–330, 1985.

[26] H. Bloom, A. Doroszkowski, and S. B. Tricklebank. The thermal conductivity of molten nitrate systems. *Australian Journal of Chemistry*, 18:1171 – 6, 1965.

[27] A. G. Turnbull. The thermal conductivity of molten salts. Part I. A transient measurement method. *Australian Journal of Applied Science*, 12, 1961.

[28] M. J. Assael, K. D. Antoniadis, and W. A. Wakeham. Historical evolution of the transient hot-wire technique. *International Journal of Thermophysics*, 31:1051 – 1072, 2010.

[29] H. S. Carslaw and J. C. Jaeger. *Heat in solids*, volume 1. Clarendon Press, Oxford, 1959.

[30] J. J. Healy, J. J. De Groot, and J. Kestin. The theory of the transient hot-wire method for measuring thermal conductivity. *Physica B+C*, 82(2):392–408, 1976.

[31] F. J. Dietz, J. J. De Groot, and E. U. Franck. The thermal conductivity of water to 250 °C and 350 mpa. *Berichte der Bunsengesellschaft für Physikalische Chemie*, 85:1005 – 1009, 1981.

[32] Y. Nagasaka and A. Nagashima. Absolute measurement of the thermal conductivity of electrically conducting liquids by the transient hot-wire method. *J. Phys. E: Sci. Instrum.*, 14:1435 – 1440, 1981.

[33] S. I. Cohen, W. D. Powers, and N. D. Greene. "a physical property summary for anp fluoride mixture," ORNL-2050. Technical report, Oak Ridge National Lab., Tenn., 1956.

[34] W. D. Powers, S. I. Cohen, and N. D. Greene. Physical properties of molten reactor fuels and coolants. *Nuclear Science and Engineering*, 17(2):200–211, 1963.

[35] M. V. Smirnov, V. A. Khokhlov, and E. S. Filatov. Thermal conductivity of molten alkali halides and their mixture. *Electrochimica Acta*, 32:1019 – 1026, 1987.

[36] Y. Nagasaka and A. Nagashima. The thermal conductivity of molten $NaNO_3$ and KNO_3. *International Journal of Thermophysics*, 12:769 – 781, 1991.

[37] Y. Kato, K. Kobayasi, N. Araki, and K. Furukawa. A method for measuring the thermal diffusivity of molten salts by stepwise heating. *Journal of Physics*, 8:461 – 6, 1975.

[38] X. Zhang and M. Fujii. Simultaneous measurements of the thermal conductivity and thermal diffusivity of molten salts with a transient short-hot-wire method. *International Journal of Thermophysics*, 21:71 – 84, 2000.

[39] M. Hoshi, T. Omotani, and A. Nagashima. Transient method to measure the thermal conductivity of high-temperature melts using a liquid-metal probe. *Review of Scientific Instruments*, 52(5):755–758, 1981.

[40] T. Omotani and A. Nagashima. Thermal conductivity of molten salts, HTS and the Lithium Nitrate-Sodium Nitrate system, using a modified transient hot-wire method. *Journal of Chemical and Engineering Data*, 29(1):1–3, 1984.

[41] R. M. DiGuilio and A. S. Teja. The thermal conductivity of the molten $NaNO_3-KNO_3$ eutectic between 525 and 590 K. *International Journal of Thermophysics*, 13(4):575–592, 1992.

[42] Y. Nagasaka and A. Nagashima. Measurement of the thermal diffusivity of molten KCl up to 1000 °c by the forced rayleigh scattering method. *International Journal of Thermophysics*, 9(6):923–931, 1988.

[43] S. Nakamura, T. Hibiya, and F. Yamamoto. Ceramic probe for measuring the thermal conductivity of an electrically conductive liquid by the transient hot wire method. *Review of Scientific Instruments*, 59(12):2600–2603, 1988.

[44] M. Harada, A. Shioi, T. Miura, and S. Okumi. Thermal conductivities of molten alkali metal halides. *Industrial & Engineering Chemistry Research*, 31(10):2400–2407, 1992.

[45] S. E. Gustafsson, N. O. Halling, and R. A. E. Z. Kjellander. Optical determination of thermal conductivity with a plane source technique. *Z. Naturforsch*, 23a:44 − 47, 1968.

[46] R. A. Perkins, A. Laesecke, and C. A. de Castro. Polarized transient hot wire thermal conductivity measurements. *Fluid phase equilibria*, 80:275–286, 1992.

[47] A. J. Bard and L. R. Faulkner. *Electrochemical Methods, Fundamentals and Applications*. ohn Wiley & Sons, 2001.

[48] P. Baruël. On the theory of transient hot-wire measurement of the thermal conductivity of electrolytic solutions. Technical report, 1973.

[49] R. Mathie and C. N. Markides. Heat transfer augmentation in unsteady conjugate thermal systems − Part I: Semi-analytical 1-D framework. *International Journal of Heat and Mass Transfer*, 56(1–2):802–818, 2013.

[50] M. L. V. Ramires, C. A. N. de Castro, R. A. Perkins, Y. Nagasaka, A. Nagashima, M. J. Assael, and W. A. Wakeham. Reference data for the thermal conductivity of saturated liquid Toluene over a wide range of temperatures. *Journal of Physical and Chemical Reference Data*, 29(2):133–139, 2000.

[51] CINDAS. *Properties of inorganic and organic fluids. CINDAS Data series on material properties*, volume 1. Hemisphere Publishing Corporation, London, 1988.

[52] ISO 5725-2:1994. accuracy (trueness and precision) of measurement methods and results – part 2: Basic method for the determination or repeatability and reproduucibility of a standard measurement method. Technical report, 1994.

[53] O. Odawara, I. Okada, and K. Kawamura. Measurement of the thermal diffusivity of HTS (a mixture of molten $KNO_3-NaNO_3-NaNO_2$; $7-44-49$ mole %) by optical interferometry. *Journal of Chemical and Engineering Data*, 22(2):222–225, 1977.

[54] N. B. Vargaftik, B. E. Neimark, and O. N. Oleshchuck. Physical properties of high temperature liquid heat transfer medium. *Bull. All-Un. PWR Eng. Inst*, 21:1, 1952.

[55] S. Kitade, Y. Kobayashi, and A. Nagasaka, Y.and Nagashima. Measurement of the thermal conductivity of molten KNO_3 and $NaNO_3$ by the transient hot-wire method with ceramic-coated probes. *High Temperatures − High Pressures*, 21(2):219–224, 1989.

[56] Y. Nagasaka and A. Nagashima. The thermal conductivity of molten $NaNO_3$ and KNO_3. *International Journal of Thermophysics*, 12(5):769–781, 1991.

[57] J. Menashe and W. Wakeham. The thermal conductivity of n-Nonane and n-Undecane at pressures up to 500 MPa in the temperature range $35-90$ °C. *Berichte der Bunsengesellschaft für Physikalische Chemie*, 86(6):541–545, 1982.

[58] C. A. N. de Castro, R. A. Perkins, and H. M. Roder. Radiative heat transfer in transient hot-wire measurements of thermal conductivity. *International Journal of Thermophysics*, 12(6):985–997, 1991.

[59] A. E. Gheribi, S. Poncsák, R. St-Pierre, L. I. Kiss, and P. Chartrand. Thermal conductivity of halide solid solutions: Measurement and prediction. *The Journal of Chemical Physics*, 141(10):104508, 2014.

[60] A. E. Gheribi and P. Chartrand. Thermal conductivity of molten salt mixtures: Theoretical model supported by equilibrium molecular dynamics simulations. *The Journal of Chemical Physics*, 144(8):084506, 2016.

[61] A. E. Gheribi, J.A. Torres, and P. Chartrand. Recommended values for the thermal conductivity of molten salts between the melting and boiling points. *Solar Energy Materials and Solar Cells*, 126:11–25, 2014.

[62] Y. Nagasaka and A. Nagashima. Corresponding states correlation for the thermal conductivity of molten alkali halides. *International Journal of Thermophysics*, 14(4):923–936, 1993.

[63] P. V. Polyakov and E. M. Gildebrandt. Investigation of thermal conductivity of melts of system KCl-MgCl$_2$, 1974.

[64] Y. Nagasaka, N. Nakazawa, and A. Nagashima. Experimental determination of the thermal diffusivity of molten alkali halides by the forced rayleigh scattering method. I. molten LiCl, NaCl, KCl, RbCl, and CsCl. *International Journal of Thermophysics*, 13(4):555–574, 1992.

[65] J. McDonald and H. T. Davis. Determination of the thermal conductivities of several molten alkali halides by means of a sheathed hot-wire technique. *Physics and Chemistry of Liquids*, 2(3):119–134, 1971.

[66] T. Hatakeyama, U. Miyahashi, M. Okuda, Y. Nagasaka, and A. Nagashima. Measurement of the thermal diffusivity of liquids by the forced rayleigh scattering method (3rd report, measurement of molten salts). *Nippon Kikai Gakkai Ronbunshu, B Hen/Transactions of the Japan Society of Mechanical Engineers, Part B*, 54(501):1131–1137, 1988.

[67] J. Ambrosek, M. Anderson, K. Sridharan, and T. Allen. Current status of knowledge of the fluoride salt (FLiNaK) heat transfer. *Thermal Hydraulics*, pages 166 – 173, 2008.

[68] V. Khokhlov, I. Korzun, V. Dokutovich, and E. Filatov. Heat capacity and thermal conductivity of molten ternary lithium,sodium, potassium, and zirconium fluorides mixtures. *Journal of Nuclear Materials*, 410:32 – 38, 2011.

[69] G. P. Bystrai, V. N. Desyatnik, and V. A. Zlokazov. Thermal conductivity of molten uranium tetrachloride mixed with sodium chloride and potassium chloride. *Atom. Energ*, 36:517–518, 1974.

[70] V. I. Fedorov and V. I. Machuev. Thermal conductivity of fused salts. *Teplofizika Vysokikh Temperatur*, 8(4):912–914, 1970.

[71] N. Nakazawa, Y. Nagasaka, and A. Nagashima. Experimental determination of the thermal diffusivity of molten alkali halides by the forced rayleigh scattering method. II. molten NaBr, KBr, RbBr, and CsBr. *International Journal of Thermophysics*, 13(5):753–762, 1992.

[72] R. G. Ross, P. Andersson, B. Sundqvist, and G. Backstrom. Thermal conductivity of solids and liquids under pressure. *Reports on Progress in Physics*, 47(10):1347, 1984.

[73] V.D. Golyshev and M.A. Gonik. High-temperature thermophysical properties of nonscattering semitransparent materials. I: Methods and instrumentation for the determination of spectral absorptivity and thermal conductivity of melts. *High Temperatures. High Pressures*, 24(4):367–377, 1992.

[74] V. D. Golyshev, M. A. Gonik, V. A. Petrov, and Y. M. Putilin. Experimental investigation of the thermal-conductivity of transparent melts. *Teplofizika Vysokikh Temperatur*, 21(5):899–903, 1983.

[75] K. Screenisavan. Ph.d. thesis. 1967.

[76] P.V. Polyakov and V.M. Mozhaev. Thermal conductivities of NaF−AlF$_3$ melts, 1975.

[77] G.P. Bystrai and V.N. Desyatnik. Thermal conductivity of alkali metal chlorides. *Teplofiz. Issled. ZhidkAkad. Nauk SSSR, Ural. Nauchn, Tsentr Sverdlovsk, USSR*, pages 34–38, 1975.

[78] V. Khokhlov, V. Ignatiev, and V. Afonichkin. Evaluating physical properties of molten salt reactor fluoride mixtures. *Journal of Fluorine Chemistry*, 130:30 − 37, 2009.

[79] M. D. Grele and L. Gedeon. Forced convection heat transfer characteristics of molten flinak flowing in an inconel x system," naca r4 e53l18, national advisory commitee for areonautics. Technical report, 1954.

[80] H. W. Hoffman. "turbulent forced convection heat transfer in circular tubes containing molten sodium hydroxide," ORNL-1370. Technical report, Oak Ridge National Lab., Tenn., 1954.

[81] H. W. Hoffman and J. Lones. Fused salt heat transfer. part II. forced convection heat transfer in circular tubes containing NaF–KF–LiF eutectic. Technical report, Oak Ridge National Lab., Tenn., 1955.

[82] I. B. Vriesma. *"Aspects of Molten Fluorides as Heat Transfer Agents for Power Generation"*. PhD thesis, Delft University of Technology, 1979.

[83] M. D. Silverman, W. R. Huntley, and H. E. Robertson. "heat transfer measurements in a forced convection loop with two molten-fluoride salts: LiF−BeF$_2$−ThF$_4$−UF$_4$ and eutectic NaBF-NaF" ornl/tm-5335.

[84] L. Bin, W. Yu-ting, M. Chong-fang, Y. Meng, and G. Hang. Turbulent convective heat transfer with molten salt in a circular pipe. *International Communications in Heat and Mass Transfer*, 36(9):912–916, 2009.

[85] Y. T. Wu, C. Chen, B. Liu, and C. F. Ma. Investigation on forced convective heat transfer of molten salts in circular tubes. *International Communications in Heat and Mass Transfer*, 2012.

[86] J. W. Ambrosek. *Molten chloride salts for heat transfer in nuclear systems.* PhD thesis, University of Wisconsin-Madison, 2011.

[87] S. Fukusako and M. Yamada. Recent advances in research on water-freezing and ice-melting problems. *Experimental Thermal and Fluid Science*, 6(1):90–105, 1993.

[88] R. D. Zerkle and J. E. Sunderland. The effect of liquid solidification in a tube upon laminar-flow heat transfer and pressure drop. *Journal of Heat Transfer*, 90(2):183–189, 1968.

[89] R. D. Zerkle. Laminar-flow heat transfer and pressure drop in tubes with liquid solidification. 1964.

[90] D. R. Oliver. The effect of natural convection on viscous-flow heat transfer in horizontal tubes. *Chemical Engineering Science*, 17(5):335–350, 1962.

[91] C. A. Depew and R. C. Zenter. Laminar flow heat transfer and pressure drop with freezing at the wall. *International Journal of Heat and Mass Transfer*, 12(12):1710–1714, 1969.

[92] J. C. Mulligan and D. D. Jones. Experiments on heat transfer and pressure drop in a horizontal tube with internal solidification. *International Journal of Heat and Mass Transfer*, 19(2):213–219, 1976.

[93] G. J. Hwang and J. P. Sheu. Liquid solidification in combined hydrodynamic and thermal entrance region of a circular tube. *The Canadian Journal of Chemical Engineering*, 54(1-2):66–71, 1976.

[94] N. DesRuisseaux and R. D. Zerkle. Freezing of hydraulic systems. *The Canadian Journal of Chemical Engineering*, 47(3):233–237, 1969.

[95] A. P. Arora and J. R. Howell. An investigation of the freezing of supercooled liquid in forced turbulent flow inside circular tubes. *International Journal of Heat and Mass Transfer*, 16(11):2077–2085, 1973.

[96] M. N. Ozisik and J. C. Mulligan. Transient freezing of liquids in forced flow inside circular tubes. *Journal of Heat Transfer*, 91(3):385–389, 1969.

[97] E. P. Martinez and R. T. Beaubouef. Transient freezing in laminar tube-flow. *The Canadian Journal of Chemical Engineering*, 50(4):445–449, 1972.

[98] J. M. Savino and R. Siegel. Experimental and analytical study of the transient solidification of a warm liquid flowing over a chilled flat plate. 1967.

[99] R. R. Gilpin. The morphology of ice structure in a pipe at or near transition reynolds numbers. In *AIChE Symposium Series*, volume 75, pages 89–9, 1979.

[100] T. Hirata and M. Ishihara. Freeze-off conditions of a pipe containing a flow of water. *International Journal of Heat and Mass Transfer*, 28(2):331–337, 1985.

[101] B. Weigand, N. Domaschke, and S. Zehner. The morphology of ice-structure in a planar nozzle subjected to forced internal convection flow. *Heat and Mass Transfer*, 44(10):1271–1279, 2008.

[102] T. R. Goodman. The heat-balance integral and its application to problems involving a change of phase. *Trans. ASME*, 80(2):335–342, 1958.

[103] P. K. Vijayan and H. Austregesilo. Scaling laws for single-phase natural circulation loops. *Nuclear Engineering and Design*, 152(1):331–347, 1994.

[104] W. Ambrosini and J. C. Ferreri. The effect of truncation error on the numerical prediction of linear stability boundaries in a natural circulation single-phase loop. *Nuclear Engineering and Design*, 183(1):53–76, 1998.

[105] A. Mangal, V. Jain, and A. K. Nayak. Capability of the RELAP5 code to simulate natural circulation behavior in test facilities. *Progress in Nuclear Energy*, 61:1–16, 2012.

[106] A. McDonald, B. Bschaden, E. Sullivan, and R. Marsden. Mathematical simulation of the freezing time of water in small diameter pipes. *Applied Thermal Engineering*, 73(1):142–153, 2014.

[107] F. B. Cheung and Baker L. Transient freezing of liquids in tube flow. *Nuclear Science and Engineering*, 60(1):1–9, 1976.

[108] A. Charogiannis, J. S. An, and C. N. Markides. A simultaneous planar laser-induced fluorescence, particle image velocimetry and particle tracking velocimetry technique for the investigation of thin liquid-film flows. *Experimental Thermal and Fluid Science*, 68:516–536, 2015.

[109] T. Jin, J. Hong, H. Zheng, K. Tang, and Z. Gan. Measurement of boiling heat transfer coefficient in liquid nitrogen bath by inverse heat conduction method. *Journal of Zhejiang University Science A*, 10(5):691–696, 2009.

[110] D. W. Green et al. *Perry's Chemical Engineers' Handbook*, volume 796. McGraw-hill New York, 2008.

[111] P. Wibulswas. *Laminar-flow heat-transfer in non-circular ducts*. PhD thesis, University of London, 1966.

[112] G. F. Flanagan, D. E. Holcomb, and S. M. Cetiner. FHR generic design criteria. *ORNL/TM-2012/226, Oak Ridge National Laboratory*, 2012.

[113] R. C. Robertson. MSRE design and operations report. part i. description of reactor design. Technical report, Oak Ridge National Lab., Tenn., 1965.

[114] Q. Lv, H. C. Lin, I. H. Kim, X. Sun, R. N. Christensen, T. E. Blue, G. L. Yoder, D. F. Wilson, and P. Sabharwall. DRACS thermal performance evaluation for FHR. *Annals of Nuclear Energy*, 77:115–128, 2015.

[115] Q. Lv, X. Sun, R. Chtistensen, T. Blue, G. Yoder, and D. Wilson. Design, testing and modeling of the direct reactor auxiliary cooling system for ahtrs. Technical report, Battelle Energy Alliance, LLC, Idaho Falls, ID (United States), 2015.

[116] M. D. Grele and L. Gedeon. Engineering database of liquid salt thermo-physical and thermochemical properties. Technical report, Idaho National Laboratory, Idaho Falls, 2010.

[117] D. F. Williams. Additional physical property measurements and assess-ment of salt compositions proposed for the intermediate heat transfer loop. *ORNL/GEN4/LTR-06-033*, 2006.

[118] D. J. Rogers, T. Yoko, and G. J. Janz. Fusion properties and heat capaci-ties of the eutectic lithium fluoride-sodium fluoride-potassium fluoride melt. *Journal of Chemical and Engineering Data*, 27(3):366–367, 1982.

[119] G. J. Janz, C. B. Allen, N. P. Bansal, R. M. Murphy, and R. P. T. Tomkins. Physical properties data compilations relevant to energy storage. II. molten salts: data on single and multi-component salt systems. Technical report, Rensselaer Polytechnic Inst., Troy, NY (USA). Cogswell Lab., 1979.

[120] Y. Chikazawa, K. Aizawa, T. Shiraishi, and H. Sakata. Experimental demon-stration of flow diodes applicable to a passive decay heat removal system for sodium-cooled reactors. *Journal of Nuclear Science and Technology*, 46(4):321–330, 2009.

[121] P. K. Vijayan, M. Sharma, and D. Saha. Steady state and stability character-istics of single-phase natural circulation in a rectangular loop with different heater and cooler orientations. *Experimental Thermal and Fluid Science*, 31(8):925–945, 2007.

Nomenclature

Italic symbols

A Area of a fluid cross section, [m^2]

A_d Fluid diode entry area, [m^2]

C Coefficient of heat transfer, [$\mathrm{W\,K^{-1}}$]

c_p Specific heat capacity, [$\mathrm{J\,kg^{-1}\,K^{-1}}$]

D_p Effective particle diameter of the porous media, [m]

E Thermal energy, [J]

f Friction factor, [-]

g Standard gravity, [$\mathrm{m\,s^{-1}}$]

H Heigth, [m]

h Heat transfer coefficient, [$\mathrm{W\,m^{-2}\,K^{-1}}$]

I Current, [A]

K Form loss coefficient, [-]

L Length, [m]

l_e Effective length of the capillary, [m]

m_s Mass of solidified salt per unit of length, [$\mathrm{kg\,m^{-1}}$]

Nu Nusselt number, [-]

P Perimeter of a fluid cross section, [m]

p Pressure, [Pa]

Pr Prandtl number, [-]

$Q, \dot{Q}$ Thermal power, [W]

$q, \dot{q}$ Heat flux, [$\mathrm{W\,m^{-2}}$]; dotted means per unit of length, [$\mathrm{W\,m^{-1}}$]

q_{sf} Fluid-side wall heat flux in presence of a solid layer of salt, [$\mathrm{W\,m^{-2}}$]

q_{sw} Tube-side wall heat flux in presence of a solid layer of salt, [$\mathrm{W\,m^{-2}}$]

R Electrical resistance (unless otherwise stated), [Ω]

r Radius, [m]

Re Reynolds number, [-]

s Spatial coordinate, [m]

T Temperature, [K]

t Time, [s]

T_0 Reference state temperature, [K]

V Volume, [$\mathrm{m^3}$]

w Mass flow-rate, [$\mathrm{kg\,s^{-1}}$]

X Thickness, [m]

z Spatial vertical coordinate, [m]

Greek Symbols

α thermal diffusivity, [$\mathrm{m\,s^{-2}}$]

β Volumetric expansion coefficient, $[\text{K}^{-1}]$

ΔH Heat (entalphy) of fusion, $[\text{J}]$

ΔP_{draft} Draft pressure in the chimney, $[\text{Pa}]$

ΔP_{NDHX} Pressure drop through the air-side NDHX, $[\text{Pa}]$

ϵ Porosity, $[\text{-}]$

λ thermal conductivity, $[\text{W}\,\text{m}^{-1}\,\text{K}^{-1}]$

λ_{d} Diffusive length scale, $[\text{m}]$

μ Dynamic (absolute) viscosity, $[\text{kg}\,\text{m}^{-1}\,\text{s}^{-1}]$

ψ Defined by Eq. 4.4, $[\text{J}\,\text{m}^{-1}\,\text{kg}^{-1}]$

ρ Density, $[\text{kg}\,\text{m}^{-3}]$

τ Shear stress (unless otherwise stated), $[\text{Pa}]$

ξ Defined by Eq. 4.6, $[\text{J,m}^{-1}\,\text{K}^{-1}]$

Common Subscripts

air   Ambient air

chim   Chimney

ext   Outside surface of the piping system

melt   Melting (temperature)

r   Reactor

ss   Steady-state conditions

w   Wall/piping material

c   Capillary

eff   Effective (real value)

l   Liquid

loss   Related to heat losses

meas Measured

s   Salt

tot   Total

Acronyms

CCM   Concentric Cylinder Method

CFD   Computational Fluid Dynamics

DHX   Molten-salt/molten-salt DRACS heat exchanger

DRACS Direct Reactor Auxiliary Cooling System

HTS   Heat Transfer Salt $(NaNO_3-NaNO_2-KNO_3)$

LFM   Laser Flash Method

LOCA Loss of Coolant

LOFC Loss of Forced Circulation

MSR   Molten Salt Reactor

MSRE Molten Salt Reactor Experiment

NDHX Molten-salt/air DRACS heat exchanger

PPM   Planar Plate Method

RSM   Rayleigh Scattering Method

THWM Transient Hot Wire Method